Master's thesis

NTNU
Norwegian University of Science and Technology
Faculty of Engineering
Department of Marine Technology

Cecilie Vangdal

Hydrodynamic Study of Floating Wind Turbines in Extreme Conditions

Master's thesis in Marine Technology
Supervisor: Marilena Greco
June 2019

NTNU
Norwegian University of
Science and Technology

Cecilie Vangdal

Hydrodynamic Study of Floating Wind Turbines in Extreme Conditions

Master's thesis in Marine Technology
Supervisor: Marilena Greco
June 2019

Norwegian University of Science and Technology
Faculty of Engineering
Department of Marine Technology

NTNU
Kunnskap for en bedre verden

Preface

This master's thesis is written as part of the five-year master's degree programme at the Department of Marine Technology at the Norwegian University of Science and Technology (NTNU) during the spring semester of 2019.

Energy resources, and especially renewable energy resources, have been an interest of mine since the start of the studies here at NTNU. Therefore, it was considered a great opportunity and exciting challenge to be able to study and write about floating offshore wind turbines in combination with my specialisation of hydrodynamics in this master's thesis. I am very grateful for everything I have learned and experienced this past year from supervisors and lecturers.

A large amount of time was spent on learning how to use the modelling and analysis programs GeniE and HydroD. In addition, due to limited available information on the semi-submersible FWT, specifically the heave plates and the ballast system, modelling and verification of the model presented some difficulties. This limited the work process and progress during some phases. Nevertheless, I have learned much about modelling, analysing and programming/post-processing throughout the duration of this thesis. Furthermore, I have developed my knowledge and skills with regard to hydrodynamics and gained an even greater interest in the field. Finally, I have learned a great deal about the exciting field of offshore wind, which, I believe, will expand greatly and keep growing.

Cecilie Vangdal
Trondheim, June 10, 2019

NTNU Trondheim
Norwegian University of Science and Technology
Faculty of Engineering Science and Technology
Department of MarineTechnology

MASTER THESIS IN MARINE TECHNOLOGY

Spring 2019

FOR

Cecilie Vangdal

Hydrodynamic study of floating wind turbines in extreme conditions

(Hydrodynamisk studie av flytende vindturbiner i ekstreme forhold)

The increasing demand of renewable energy sources from the oceans supports investigations of floating wind turbines (FWT) in deeper water conditions. This avoids issues connected with visual impact and can offer greater available wind power. Moreover, FWTs have construction advantages and good adaptation to different water depths. However, they must ensure a continuous functioning, and survive under severe environmental conditions. During extreme storm systems, FWT must have adequate structural integrity in parked condition and with blades pitched to feather. Moreover, yaw control is needed to track possible change in wind direction. Therefore, accurate prediction of their extreme response is important.
A preliminary project work has been carried out to document the state of the art. Two FWT concepts, a spar (spar-type OC3-Hywind) and a semisubmersible (WindFloat), have been selected. They were designed to operate with the same wind turbine (5 MW NREL turbine) and in the same site (Tampen area, northern North sea). Relevant environmental conditions of the site were identified. The simulation platform SIMA was selected as research tool and preliminarily applied to the semisubmersible. Free-decay tests were performed to check the natural periods and the damping level of the system. Then, selected operational conditions were reproduced to estimate the importance the different environmental parameters (wind, current and waves) on the motions and on the FWT mean drift.

Objective
The present master thesis aims to investigate the selected FWT concepts in extreme environmental conditions, and to compare their response features and challenges, possibly speculating on design improvements.

The work should be carried out in steps as follows:

1. Summarize major findings/outcomes from the project thesis and, if necessary, complement the literature survey in order to identify state-of-the-art of the problem.
2. Describe the assumptions and features of the simulation platform selected as research tool. Complement with the modelling of second-order slow-drift load effects, neglected in the project-thesis studies.
3. Investigate the possible reasons for differences in the semisubmersible results examined in the project work and the reference solutions. Apply the simulation platform to verify proper modelling of the spar-type FWT.
4. Perform a systematic study of the two selected FWTs in extreme conditions. Analyse relevant response variables and discuss comparatively the two concepts in terms of advantages and challenges. Examples of targeted investigations are: influence of different return period, of wind-wave misalignment, of nonlinear (slow-drift) hydrodynamic loads, on relevant response variables for each floating platform and its wind turbine.

5. Draw the conclusions from the studies and discuss possible further research steps.

The work may show to be more extensive than anticipated. Some topics may therefore be left out after discussion with the supervisor without any negative influence on the grading.

The candidate should in her report give a personal contribution to the solution of the problem formulated in this text. All assumptions and conclusions must be supported by mathematical models and/or references to physical effects in a logical manner.

The candidate should apply all available sources to find relevant literature and information on the actual problem.

The thesis should be organised in a rational manner to give a clear presentation of the work in terms of exposition of results, assessments, and conclusions. It is important that the text is well written and that tables and figures are used to support the verbal presentation. The thesis should be complete, but still as short as possible. In particular, the text should be brief and to the point, with a clear language. Telegraphic language should be avoided.

The thesis must contain the following elements: the text defining the scope (i.e. this text), preface (outlining project-work steps and acknowledgements), abstract (providing the summary), table of contents, main body of thesis, conclusions with recommendations for further work, list of symbols and acronyms, references and (optional) appendices. All figures, tables and equations shall be numerated.

The supervisor may require that the candidate, in an early stage of the work, present a written plan for the completion of the work. The plan should include budget for the use of computer and laboratory resources that will be charged to the department. Overruns shall be reported to the supervisor.

From the thesis it should be possible to identify the work carried out by the candidate and what has been found in the available literature. It is important to give references to the original source for theories and experimental results.

Supervisor : Marilena Greco
Co-supervisor : Erin Bachynski
Co-supervisor : Claudio Lugni

Submitted : January 15th 2019
Deadline : June 11th 2019

Marilena Greco
Supervisor

Acknowledgements

I would like to thank my supervisor Professor Marilena Greco for invaluable help, insight and advice throughout the course of this master's thesis. I have greatly appreciated our weekly meetings, both in terms of work progress and discussions on theory, results and how to proceed when problems have occurred. I am thankful for the genuine interest Professor Greco has in helping me succeed with this thesis.

From co-supervisor Associate Professor Erin Bachynski I have received a great deal of help with problems and challenges with GeniE, HydroD and SIMA. Her knowledge about floating wind turbines has been particularly valuable. I am very grateful for all help with small and big questions. Co-supervisor Adjunct Professor Claudio Lugni has provided help and knowledge on renewable energy and hydrodynamics, for which I am very thankful. Further, Postdoctoral Fellow Yugao Shen has been very helpful with problems regarding HydroD, and PhD candidate Carlos de Souza has been helpful with challenges regarding SIMA.

Abstract

The increasing demand of renewable energy sources has supported investigations and developments of offshore floating wind turbines in deep waters. Challenges in deep waters involve stronger wind and waves, and the response in extreme combined wind-wave-current conditions must be characterised. The scope of this project was to investigate two selected floating wind turbine concepts in extreme environmental conditions, and to compare their response features and challenges.

Based on the literature study performed in this thesis, it was decided to focus on wind/wave misalignment, return period of the environmental conditions, structural loads in the tower, mooring line tensions and effects of second-order wave excitation forces during extreme environmental conditions. The two chosen FWTs, OC3-Hywind and WindFloat, were modelled in GeniE, hydrodynamically analysed in HydroD/WADAM, and in SIMA, integrated dynamic analyses were performed. The output from the first- and second-order analyses in HydroD consisted of mass, added mass, damping and hydrostatic stiffness matrices, excitation forces, RAOs, mean drift forces, QTFs and wave drift damping. These results were imported into SIMA for coupled dynamic analyses.

The numerical models were verified through the results from the hydrodynamic analyses in HydroD and by free decay tests in SIMA. The mean drift forces, RAOs, natural periods and QTFs were utilised in the verification which in general were deemed successful.

The OC3-Hywind FWT is subject to the largest motion variation, while WindFloat has the largest maximum offset. The tower of OC3-Hywind withstands the extreme conditions better in terms of axial force, while, in terms of bending moment, WindFloat withstands the extreme conditions better. The mooring lines of WindFloat is subject to lower tensions at the fairlead, than OC3-Hywind. The misalignment of the wind greatly affects the structural loads and the mooring line tensions, while the platform motion responses generally are not influenced. Of the analysed response variables, only the hydrodynamic forces and mooring line tensions are greatly influenced by the second-order wave forces.

In addition to the above results, the effect of wave drift damping and viscous forces on the heave plates of WindFloat were investigated. However, they are both subject to further work as only brief preliminary investigations were performed. Additional suggested further work, are the inconsistent results with regard to the structural loads in the tower and the mooring line tensions during aligned and misaligned extreme conditions.

Sammendrag

En økende etterspørsel etter fornybare energiressurser har støttet opp under nye studier og videre utvikling av offshore flytende vindturbiner på dypt vann. Utfordringer knyttet til denne teknologien er sterk vind og høye bølger, og responsen i ekstreme værhold må karakteriserer i kombinasjoner av vind, bølger og strøm. Objektet i denne masteroppgaven var å studere to flytende vindturbiner i ekstreme værforhold, og å sammenligne deres egenskaper og utfordringer i forhold til utvalgt responsvariabler.

Basert på litteraturstudiet, ble det bestemt å fokusere på ulike retninger på vind og bølger, returperiode for værforholdene, strukturelle laster på tårnet, samt spenninger i forankringslinene i ekstreme værforhold. De to flytende vindturbinene, OC3-Hywind og WindFloat, ble modellert i GeniE, hydrodynamisk analysert i HydroD/WADAM, og i SIMA ble det utført integrert dynamisk analyse av modellene. Resultatene fra første- og andre-ordensanalysene i HydroD besto av masse-, added mass-, dempnings- og stivhetsmatriser, eksitasjonskrefter, RAO, "mean drift"-krefter, QTF og "wave drift"-dempning. Disse resulatene ble deretter importert til SIMA for videre koblet dynamisk analyse.

De numeriske modellene ble verifisert ved hjelp av resulatene fra HydroD og fritt-fall-tester i SIMA. "Mean drift"-krefter, RAO, egenperioder og QTF ble brukt for å verifisere, som generelt ga gode resultater.

Utifra resultatene fra simuleringene har OC3-Hywind størst variasjon i bevegelsene, mens WindFloat har størst maksimal bevegelse. Tårnet på OC3-Hywind tåler de ekstreme forholdene best med tanke på aksialkrefter, mens tårnet på WindFloat tåler forholdene best med tanke på bøyemomentet. Forankringslinene på WindFloat er utsatt for mindre krefter enn de på OC3-Hywind. Ulik retning på vind og bølger påvirker de strukturelle lastene i tårnet og spenningene i forankringslinene til en viss grad, mens bevegelsene til strukturene generelt ikke er påvirket. Det er kun de hydrodynamiske kreftene og forankringslinene som blir påvirket av andre-ordens bølgekrefter.

I tillegg til de overnevnte resulatene, ble effekten av "wave drift"-dempning og viskøse krefter på hivplatene til WindFloat undersøkt. Begge aspekter er foreslått for videre arbeid. Andre forslag for videre arbeid er de utvetydige resulatene med tanke på de strukturelle lastene i tårnet, samt spenningen i forankringslinene med ulike retninger på vinden i ekstreme værforhold.

Table of Contents

List of Figures

List of Tables

Nomenclature

Abbreviations

BEM	blade element momentum
BC	boundary condition
CFD	computational fluid dynamics
DoF	degree of freedom
FEM	finite element method
FWT	floating wind turbine
FS	free surface
JONSWAP	Joint North Sea Wave Project
LC	load case
MSL	mean sea level
NREL	national renewable energy laboratory
NTM	normal turbulence model
OC3	offshore code comparison collaboration
PSD	power spectral density
PDF	probability density function
QTF	quadratic transfer function
RAO	response amplitude operator
rpm	rotations per minute
SWL	still water level
TLP	tension-leg platform
WADAM	Wave Analysis by Diffraction and Morison Theory
WT	wind turbine
WF	WindFloat
W, GW, MW	watt, giga watt, mega watt

Latin letters

A	added mass coefficient (matrix)
a	acceleration
A_{33}	heave added mass coefficient
B	damping coefficient (matrix)
B_{33}	heave damping coefficient
B_g	dissipative force coefficient
C	restoring coefficient (matrix)
C_a	Morison added mass coefficient
C_d	drag coefficient
C_m	Morison mass coefficient
D	diameter, drag force
D_c	diameter of column
D_p	diameter of plate
dz	strip length
F	force, probability distribution
f	frequency in Hz
F^{sv}	slow drift force

g	gravitational acceleration
H_s	significant wave height
KC	Keulegan-Carpenter number
L	length
M	mass coefficient (matrix)
M_g	inertial force coefficient
p	pressure, probability
p_N	force normal to the rotor plane (aerodynamic)
p_T	force tangential to the rotor plane (aerodynamic)
Q	torque
R	return period, radius
R_{ext}	external work
R_{int}	internal work
S	spectrum
S_{inf}	wetted surface
T	thrust
T_{jk}	second-order transfer function
T_n, T	natural period, period
t_p	thickness of heave plate
T_p	spectral peak period
T_z	zero up-crossing period
u	horizontal fluid velocity
U_0	1-hour mean wind speed
U_c	current velocity
U_w	wind velocity
V_i	velocity horizontal direction
V_n	normal component of fluid velocity
X, x	rigid body displacement
z	height above sea level

Greek letters

α	location parameter
β	scale parameter
γ	shape parameter
ϵ	phase angle
ζ	wave amplitude
η, $\dot{\eta}$, $\ddot{\eta}$	body motion, velocity and acceleration
κ	retardation function
μ	mean value
ρ	density
σ	standard deviation
τ	duration of event
ϕ	velocity potential
ω	angular frequency
Ω	angular rotor velocity

Chapter 1

Introduction

1.1 Background

Wind power is a reliable, affordable and clean form of energy, and the demand for continued development of wind power onshore and offshore is increasing. Onshore wind farms have a capacity factor up to 35 %, while offshore wind farms are reported with an average capacity factor of 50 % (WindEurope 2019). The water is often deep at open sea, and the winds are stronger, more reliable and more consistent than the onshore winds. In addition, suitable near-shore locations at shallow waters for fixed wind turbines are limited. Thus, the need for development within floating offshore wind turbines (FOWT's) is extensive.

Challenges connected with floating wind turbines (FWT's) arise due to deeper water and higher winds. The size and rated power of the turbines need to increase equivalently, to be able to harvest the wind and increase energy production (Kaldellis et al. 2016). One of the largest challenges is the rough environment at open sea which the wind turbines will be exposed to. In addition, global warming has increased the occurrence of extreme weather. This master's thesis will thus focus on investigating two selected floating wind turbine concepts in extreme environmental conditions.

1.1.1 Offshore Wind Energy Today

The first bottom-fixed offshore wind farm was installed outside the coast of Denmark in 1991 (Rock and Parsons 2010). In September 2009, the world's first full scale (large-capacity) floating wind turbine was installed outside the coast of Norway (Equinor 2018; WindEurope 2018): Equinor's demonstration spar floater Hywind Demo with a 2.3 MW turbine operated for eight years. In 2011, Principle Power Inc. installed the 2 MW prototype FWT WindFloat outside the coast of Portugal (Gao et al. 2018; PrinciplePower 2015). Following the two first prototypes of floating offshore wind turbines, several other FWTs have been tested and deployed. Among others; SeaTwirl deployed its first FWT off the coast of Sweden in 2011 (SeaTwirl 2011), University of Maine deployed a 1:8th scale prototype of a 6 MW FWT outside Maine in 2013 (UMaine 2019b), the Fukushima Offshore Wind Consortium deployed a full-scale 2 MW semi-submersible FWT outside of Naraha, Japan in 2015 (Consortium 2018).

Further developments of the FWT technology led to the first operational commercial floating wind farm being installed in 2017, Hywind Scotland, with a capacity of 30 MW (Equinor 2018). A joint venture including Principle Power Inc. are planning to commission a 25.2 MW wind farm off the coast of Portugal, called WindFloat Atlantic (PrinciplePower 2015). The three turbines will each be of 8.4 MW and will thus become the largest turbines installed on floating sub-structures. The project New England Aqua Ventus I consists of two 6 MW turbines on VolturnUS and will be installed during 2019 and fully operated in 2020. The wind farm will thus become the first floating wind farm in the Americas (UMaine 2019a).

According to the Global Wind Energy Council (GWEC 2018), 4.5 GW of offshore (floating and bottom-fixed) wind capacity were installed during 2018, bringing the total global offshore wind capacity to 23.1 GW (figure 1.1b, 1.1c). The total global offshore installations are then approximately 4 % of the total installed wind capacity. United Kingdom, Germany and China are the countries with most installed offshore wind capacity. In addition, Taiwan, South Korea, Japan, the US and Denmark are considered developing offshore wind markets.

The share of global offshore installations is expected to reach 25 % by 2025 (GWEC 2018). As presented in figure 1.1a, an increase in installed capacity offshore is expected. The first large-scale offshore installations in North-America are expected to be deployed by 2022/2023. Until then, the Asian and European markets will continue to install offshore wind farms.

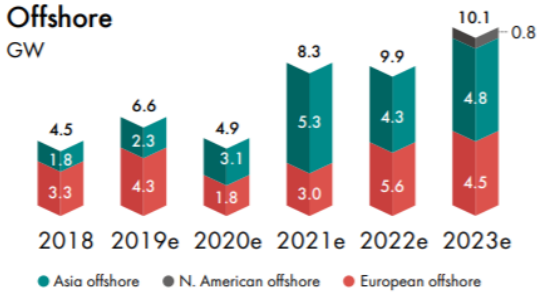

(a) Regional outlook on new installations offshore

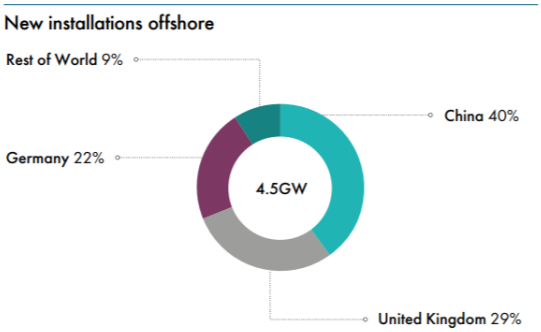

(b) New installations offshore 2018

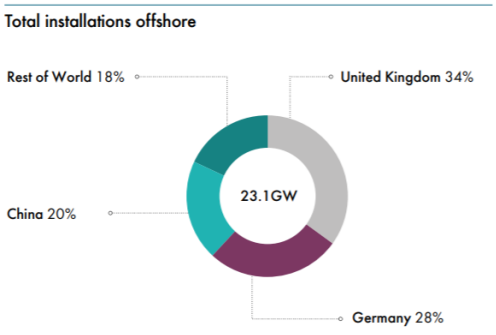

(c) Total installations offshore 2018

Figure 1.1: Offshore wind turbine installations (GWEC 2018)

1.1.2 Summary of Project Thesis

The project thesis carried during the fall semester of the academic year 2018/2019 worked as a preparation for this master's thesis. It was a preliminary study on floating offshore wind turbines in extreme conditions. The focus was split between a literature study and a preliminary dynamic analysis of a semi-submersible floating wind turbine (FWT) for validation of the analysis tool. The literature study aimed to research the state-of-the-art within theoretical, numerical and experimental studies and applications of FWT, with a focus on extreme conditions. The simulation platform and two FWT concepts were chosen based on the findings in the literature study. A suitable location in the North Sea with a water depth of 300-350 m was chosen, and environmental conditions provided by Equinor were implemented in the coupled analysis.

It was decided to study a modified version of the the semi-submersible FWT WindFloat developed by Principle Power Inc. (PrinciplePower 2015), and the spar FWT OC3-Hywind based on Equinor's concept (Equinor 2018). The turbine to be utilised in the analyses is the baseline 5 MW wind turbine developed by NREL. In view of state-of-the-art numerical tools, SIMA was chosen as the simulation platform for the coupled analysis. The numerical model of the semi-submersible FWT, provided by co-supervisor Erin Bachynski, was verified through three tests: constant wind tests (turbine performance tests), free decay tests and a coupled analysis with operational wind-wave-current conditions.

The constant wind tests presented a corresponding wind turbine behaviour with reference performance curves from Jonkman et al. (2009). The free decay tests presented deviations between the obtained natural periods T_{na} and reference values T_{nb} from Kvittem (2014), who analysed an approximately similar model with respect to dimensions, mass and mooring system. The results revealed that the obtained surge and yaw natural period is underestimated, and the sway natural period is overestimated, see table 1.1. The deviations could be explained by significant coupling effects between the platform motions, in addition to the calculation method of the natural periods, which is based upon considering a 1DoF-system, while the numerical model is analysed as a 6DoF-system. However, through the duration of the master thesis it was discovered that the static global positions of the anchor points in the provided SIMA-model are placed 58 m closer to the platform in x-direction, and 64 m farther away from the platform in y-direction, than the model by Kvittem (2014). This difference in length of the mooring line, would have greatly influenced the natural periods in sway and surge.

Table 1.1: Natural periods for WindFloat found during the project thesis

DoF	T_{na} [s]	T_{nb} [s]
Surge	99.9	107.0
Sway	147.5	124.8
Heave	19.9	19.9
Roll	36.7	35.6
Pitch	36.8	37.4
Yaw	64.38	68.5

The response study of the FWT system in a wind-wave-current environment revealed that the body motions are smaller for coupled conditions, than when the super-position principle is utilised on the load responses. The wind loading is shown to induce a large initial offset in surge and pitch, while the wave loading contributes to the continued platform motion oscillation (figure 1.2). The columns of the platform modelled as Morison slender elements contribute to a surge mean-drift and the deviations between the coupled and separate loading, due to a quadratic hydrodynamic drag coefficient.

Regarding proceeding work, it was proposed to model the two concepts in GeniE, and thus perform a hydrodynamic analysis before importing the models into SIMA where a coupled dynamic analysis was to be performed. In HydroD, a second-order analysis would be performed, to fully simulate and analyse the floating wind turbines in extreme conditions in SIMA. During the literature study, certain areas were found to be important for analysis of FWT during extreme conditions. It was thus proposed to study the influence of misaligned wind and waves, different environmental return periods and non-linear hydrodynamic loads.

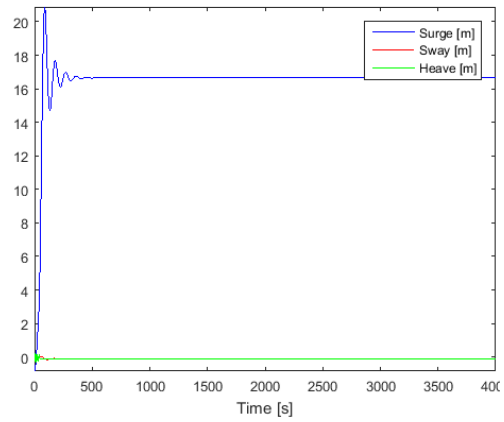

(a) Wind response - translations

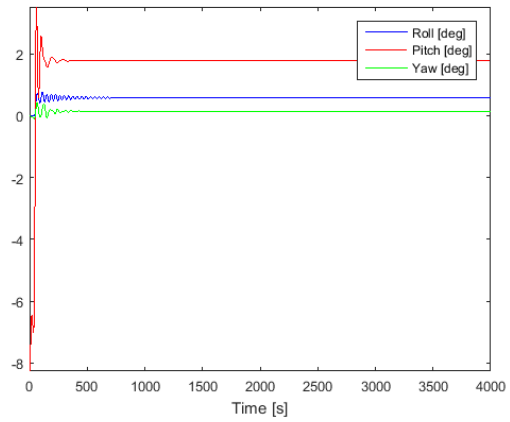

(b) Wind response - rotations

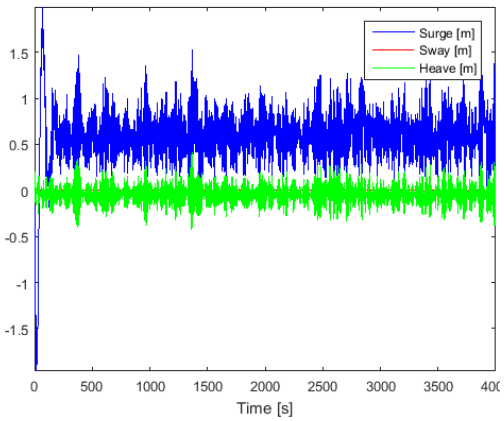

(c) Wave response - translations

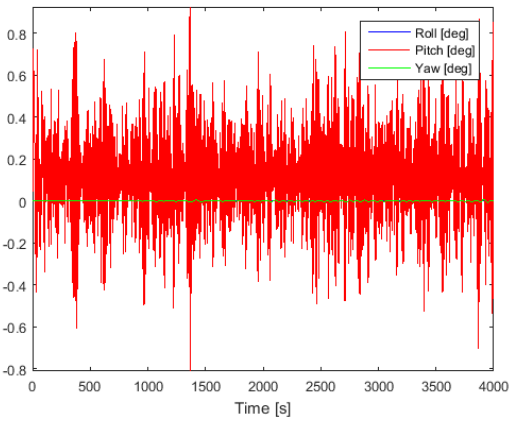

(d) Wave response - rotations

Figure 1.2: Platform motions due to separate loading

1.2 Scope

The present master's thesis is a continuation of the project thesis described above, and will aim to perform a hydrodynamic study of two floating wind turbines in extreme conditions. The scope of the master thesis will be to investigate the selected FWTs in extreme environmental conditions, and to perform a comparison of their response features and challenges. As a result of the preliminary literature study of the state-of-the-art for FWTs, possible investigative factors may be: the influence of different return periods, wind-wave misalignment and non-linear hydrodynamic loads.

1.3 Structure of the Report

A literature review on numerical modelling, studies on extreme conditions and second-order effects on FWTs is presented in chapter 2. Chapter 3 presents the utilised theory on hydrodynamics, aerodynamics and coupled time-domain analysis. The two floating wind turbine sub-structures and the publicly open wind turbine are described in chapter 4, before the location and environmental conditions are described in chapter 5. The utilised softwares and methodology of the design process are explained in chapter 6. Verification of the models and the subsequent study of FWTs in extreme environmental conditions are presented in chapter 7 and 8. The conclusion of this master's thesis and future work are given in chapter 9.

Chapter 2

Literature Study

2.1 Numerical Modelling

Numerical modelling of FWTs is heavily based on traditional frequency-domain methods used in the oil and gas industry. However, to correctly model FWTs, the coupling effects between hydrodynamics, aerodynamics, structural, mooring lines and the turbine control properties need to be accounted for. The state-of-the-art numerical modelling methodologies are thus integrated aero-hydro-servo-elastic analyses, based on coupled time-domain analyses. Borg and Bredmose (2015) present an overview of the most common numerical tools for FWT design and verification utilised by the partners in the LIFES50+-consortium. This is an international consortium with 12 partners, and is led by SINTEF Ocean. They are thus considered to represent the state-of-the-art of numerical tools for design of floating offshore wind turbines, and will be further presented. The theory which the numerical tools are based upon will be described in chapter 3.

The open-source integrated numerical tool FAST, developed by National Renewable Energy Laboratory (NREL), is the most common tool used by the partners in LIFES50+. Engineering models for hydrodynamics, aerodynamics, structural dynamics and control theory are integrated in the software, and an aero-hydro-servo-elastic time-domain simulation is performed for the whole system. FAST is implemented with the blade element momentum theory (BEM) for aerodynamics and the hydrodynamic force models include slender or large-volume structures from ANSYS AQWA or WAMIT. The two latter are commercial numerical tools developed for analysing interaction between waves and offshore structures and ships. Both tools solve the potential flow solution in the frequency-domain, with possibilities of transforming the results for time-domain simulations. In addition, second-order potential flow hydrodynamic forces may be evaluated.

SIMA (SIMO/RIFLEX) is another common numerical tool package for FWT design, developed by SINTEF Ocean. The package performs coupled time-domain analysis in this thesis. SIMA imports frequency-domain hydrodynamic properties from an external software, while aerodynamics are modelled by BEM and the structural response is modelled by a non-linear FE-approach in RIFLEX. Further description of SIMA and its features are given in section 6.1. In general, the tools utilised in the LIFES50+-consortium are based on a similar approach for design and analysis of FWTs.

2.1.1 Verification

Several international research projects have aimed to perform verification of numerical tools used in the LIFES50+-consortium, such as the Offshore Code Comparison Collaboration (OC3) (Jonkman and Musial 2010), the Offshore Code Comparison Collaboration Continuation (OC4) (Robertson et al. 2014) and the INNWIND.EU project (Azcone et al. 2013). The projects aimed to perform code-to-code comparison of numerical tools for design and analysis of FWTs.

The European INNWIND.EU project (2013-2017) worked on innovative designs of support structures for a 20 MW FWT. The most common numerical tools used for aero-hydro-servo-elastic analysis of FWTs were verified. The OC3 and OC4 projects aimed to verify the accuracy and correctness of numerical codes for FWT analysis. Several types of both bottom-fixed and floating support structures were analysed by several codes: monopile, tripod, spar-buoy, jacket structure and a semi-submersible. The reports conclude that most of the numerical tools are verified through code-to-code comparison through the three mentioned research projects.

2.1.2 Validation

Validation of numerical codes through comparison with experimental model tests have not been sufficiently performed in the same way as is the case with verification of the codes. However, through the Offshore Code Comparison Collaboration Continuation, with Correlation (OC5) (Robertson et al. 2017) and the INNWIND.EU-project (Azcona et al. 2014), validation has been performed with varied success.

The state-of-the-art within experimental methods for floating wind turbines to be used for validating integrated numerical simulation tools, were investigated. Three methods are presented, with different ways of solving the challenges regarding scaling effects and wind generation.

- Pure Froude and geometrical scaling: based on the methods traditionally used on large-scale floating offshore vessels and structures from the oil, gas and marine industry. Utilise Froude scaling and geometric similitude. The aerodynamic loading is shown not to be sufficiently accounted for during pure Froude-scaling experiments (Robertson et al. 2013).

- Froude-scaling with modified geometry: a simplification of the aerodynamic simulation was performed by Cermelli et al. (2009), where the rotor was replaced by a drag disk which attracted wind loads corresponding to the wind design force (figure 2.1a). Limitations to the method were found regarding the weight scaling, aerodynamic torque and the turbine controller.

- Hybrid testing: solves the Froude-Reynolds-scaling problems by physically model one part of the system, while the other part of the system is numerically simulated on a computer (figure 2.1b). They interact in real-time through sensors and actuators (Sauder et al. 2016).

The OC5-project compared a model test of a semi-submersible in a wave basin, under combined Froude-scaled wind and wave loading, with numerical analysis. The scaling

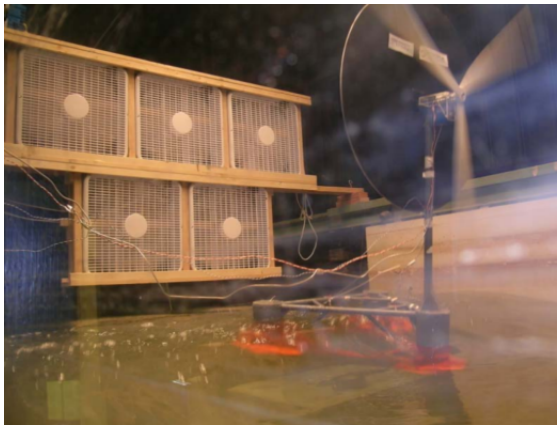

(a) Froude-scaling with modified geometry (Cermelli et al. 2009)

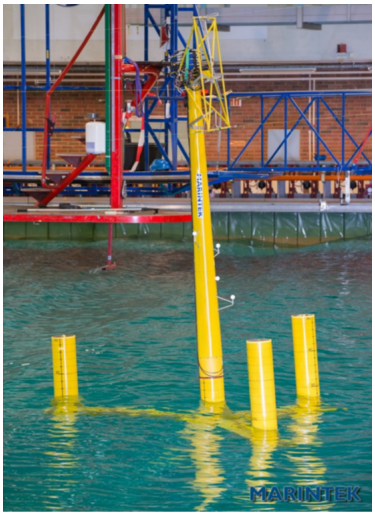

(b) Real-time hybrid-testing (Karimirad et al. 2017)

Figure 2.1: Experimental testing of FWTs

gave initial problems with the wind environment, which led to a rebuilding of the turbine. The results presented an underestimation of non-linear wave excitation forces, and the report concluded with the importance of including hydrodynamic attributes that induce non-linear wave forces in the numerical codes (Robertson et al. 2017).

Azcona et al. (2014) performed a hybrid model test of a semi-submersible, emphasising the scaling problems between the Reynolds-dependent wind environment and the Froude-dependent wave environment. A ducted fan was installed and governed by a real time computation of the full rotor, and coupled with the motions of the semi-submersible platform during the test. The experimental results correspond in general well with the numerical computations.

Karimirad et al. (2017) compared real-time hybrid experimental model tests with numerical analysis of a semi-submersible in SIMA. Vittori et al. (2018) also performed a hybrid experimental model test, similar to the one performed by Azcona et al. (2014), to validate the numerical tool FAST. The importance of second-order hydrodynamics in cases with irregular waves and constant wind were emphasised, while those effects were less important than the aerodynamic effects in cases with irregular waves and turbulent wind. Nevertheless, both reports concluded with good agreement between the integrated numerical simulations and the experimental hybrid results.

In general, verification of the most used integrated numerical tools have been verified. Validation of the codes have in many cases proved successful through hybrid experimental tests. However, further improvement of the experimental methods and implementation of second-order effects in the numerical codes will be essential in further development of innovative and cost-effective solutions for FWTs.

2.2 Studies on FWTs Under Extreme Conditions

Floating wind turbines placed in areas with deep water are exposed to stronger environmental conditions, and thus more complex loads, than offshore bottom-fixed WTs in shallow waters and onshore WTs. The structural integrity of FWTs and the coupling effects between the platform motions and the aerodynamic loads on the tower and turbine are essential to accurately predict. The loads due to the extreme wave and wind conditions are thus important to predict, simulate and analyse accurately. Several recent studies have emphasised this issue, and will be presented in the following paragraphs.

Utsunomiya et al. (2014) developed a dynamic analysis tool for floating offshore wind turbines, with similar assumptions to SIMA, and compared simulation results with experiments. The spar-FWT exposed to an extreme environmental condition, which corresponds to a 50-year storm, is in parked condition and analysed for three aligned/misaligned wind/wave conditions. The misalignment of wind and waves significantly influence the mean values of the platform responses, while the simulations and experiments in general corresponded well. However, vortex-induced motions are not implemented in the developed tool, unlike in SIMA, where this can be implemented by including the drag-amplification factor. This leads to an underestimation of the numerical results of the current loads and cross-flow responses compared to the experiments.

The coupled dynamic behaviour of the Hywind spar platform under maximum and survival conditions, was investigated by Bae and M. H. Kim (2014) in the numerical tool FAST. Maximum conditions are defined at cut-out wind speed and with a power-generating turbine. The survival condition is defined as the 100-year storm in the Gulf of Mexico, with parked turbine and fully feathered blades. First-order wave frequency wave loading, second-order difference-frequency wave loading (by Newman's approximation), tower and blade wind loading and platform responses were investigated.

The loading connected to the waves is largest in the survival conditions, while the wind loading on the blades is largest in the maximum operational condition, see figure 2.2. Resonance peaks are present in the survival condition due to large excitation near the natural frequencies for all six degrees of freedom. Due to aerodynamic damping for fully operating blades, the resonance is greatly reduced during operational condition. The maximum mooring line top-tensions are approximately 45 % larger in survival condition, due to large surge and heave slow-drift motions. Fatigue failure in the blade roots may occur due to large shear force during operation. The report thus concludes that the main design of FWTs should be based on survival conditions, while blade design should be based on maximum operational condition.

Karmakar et al. (2016) simulated combined wind and wave conditions and predicted the out-of-plane (OoP) bending moment, and blade root and tower-base moment loads on a spar and a semi-submersible FWT in FAST. The environmental contour (EC) method is used to estimate the long-term joint probability distribution, to be able to predict the extreme loads. The EC-method is based on an inverse first-order reliability method and considers combinations of random variables related to the platform performance. The response amplitude operator (RAO) is presented for surge, heave and pitch motions of the two platforms. The RAO's are higher for the semi-submersible

than for the spar platform, where the latter increases with the wave period and the former is unstable with regard to the wave period. Two cases with extreme conditions are considered with 50- and 100-year return period. The OoP bending moment for the two load cases and the two platforms increase with increasing return period, i.e. when the wave height and wind speed increase. In general, the results predicted with the EC-method show that the semi-submersible have smaller predicted OoP and tower-base bending moments than the spar platform in the two extreme conditions.

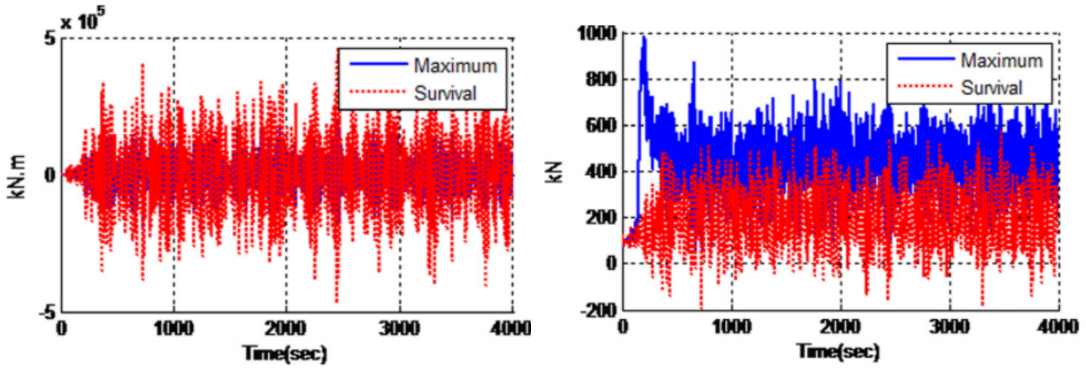

(a) Pitch wave loading

(b) Blade wind loading

Figure 2.2: Time histories of the wave and blade wind loading (Bae and M. H. Kim 2014)

Critical environmental conditions and design load cases were identified during the LIFES50+-project (Müller et al. 2018). Two 10 MW semi-submersible FWTs were investigated during numerical simulations in FAST. The aerodynamic effects were calculated with BEM and the hydrodynamics with potential flow theory in combination with Morison drag forces or Newman's approximation (second-order forces). Two load cases (LC) were defined with extreme wind and/or wave conditions: LC1 has a normal turbulence wind model (operational turbine) but a severe sea state model, while LC2 has a turbulent extreme wind speed model (parked turbine) and an extreme sea state.

An ultimate limit state (ULS) sensitivity analysis was performed for the two load cases for seven and eight environmental conditions, respectively. The global sensitivity analysis illustrates that wind speed, wave period and wind/wave-misalignment are of major importance on the loading for both load cases. For LC1, a significant decrease in the overall loading on the structures was discovered when "neglecting the range between physical breaking wave limit and the minimum period required for severe sea states by standards" (Müller et al. 2018). For LC2, the blade root bending moment was dominated by the wind speed, while the tower base bending moment and the fairlead tensions were mainly dominated by the wave period and direction.

2.3 Second-Order Effects on FWTs

Research of the effects of second-order wave-excitation forces on FWTs have not yet been thoroughly investigated, as most state-of-the-art numerical tools neglect these effects and only consider first-order effects. However, some studies have been performed and the key factors will be presented in the following paragraphs.

Duarte et al. (2014) performed a spectral analysis of the influence of the second-order wave loads on the FWT OC3-Hywind, by implementing the second-order hydrodynamic loads in FAST with the quadratic transfer functions (QTF). Four load cases for the spectral analysis were chosen; three under normal power production operation (one is defined as extreme) and one when the turbine is in parked condition with normal wind and sea state. The analyses were performed with only first-order loads, Newman's approximation, difference-frequency full QTF, sum-frequency full QTF and complete second-order solution.

When there is no wind, the sum-frequency and Newman's approximation underestimates the surge motion, pitch motion and fairlead tension around their respective natural frequencies (figure 2.3a). The surge motion is dominated by the wind loads as there is no significant influence of the second-order excitation forces during normal conditions. However, the pitch motion is influenced by the difference-frequency, and Newman's approximation underestimates the loads around its natural frequency. For extreme wave load, the influence of the second-order loads is clearly visible for both surge motion, pitch motion and the fairlead tension, as Newman's approximation again underestimates the effects around the natural frequencies (figure 2.3b).

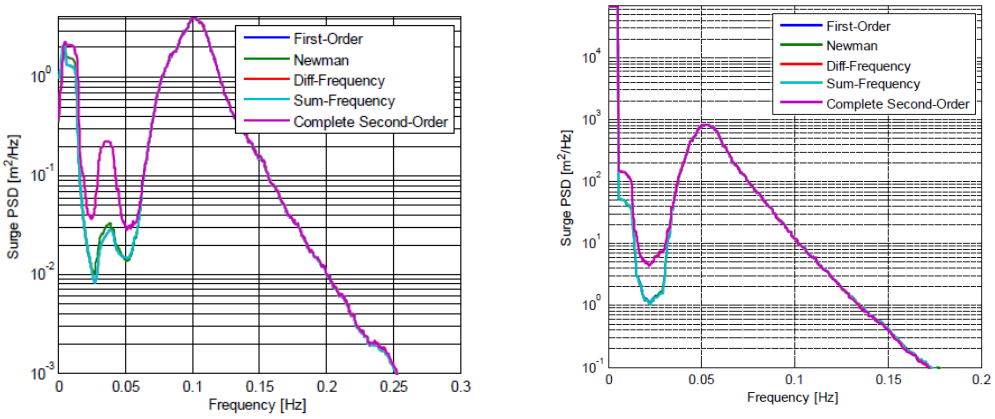

(a) Without wind loads

(b) With wind loads and severe sea state

Figure 2.3: Power spectral densities of the surge motion (Duarte et al. 2014)

The second-order hydrodynamics of a semi-submersible FWT were investigated by analysing different options for estimation of the slow-drift motions by Simos et al. (2017). The case study consisted of experimental model tests and numerical model tests performed in WAMIT as no wind loading were considered; experimental decay tests, experimental and numerical first-order and second-order analysis in regular, irregular and bichromatic waves. Response amplitude operators (RAO's), mean drift forces, QTF's and response spectra were obtained. The slow-drift motions were com-

puted with full second-order QTF from WAMIT, with Newman's approximation and with the white noise approach. A general underestimation of the slow-drift forces are observed by the Newman's approximation and white noise approach compared to the full QTF method. This can be explained by the low natural periods of the horizontal motions, as Newman's approximation in general are valid for deep-water moored structures with large resonant periods in the horizontal plane ($>$ 100s). The white noise approach only requires that the second-order spectrum is narrow-banded, which is the case here, and the QTF is computed for frequency-pairs with $\Delta\omega = \omega_n$ of the drift motion, which greatly reduces the computational time and effort. The white noise approach therefore corresponds better with the full QTF, than Newman's approximation does.

The effects of second-order wave-body interaction on the global performance of the OC4 semi-submersible FWT were investigated by H. C. Kim and M. H. Kim (2015) in a numerical tool combination of WAMIT, FAST and CHARM3D. The numerical results were compared with the DeepCWind experimental results. Time series and motion spectra were obtained by first-order analysis, full-QTF second-order analysis and Newman's approximation. Irregular waves in two white-noise wave spectra were applied, with no wind or current loading.

In general, the second-order numerical results agree well with the experimental results. The surge and pitch slowly varying motions are underestimated when only first-order analysis is executed, while the heave motion shows approximately no difference between the three applied methods, see figure 2.4. This effect is also visible for the mooring line tension. Where Newman's approximation is applied, the surge slowly varying motion agrees well with the experiments, however, the results are less accurate for the pitch motion. Regenerated plots of the second-order difference-frequency wave spectra are also presented which verifies the above results. It is emphasised that Newman's approximation is sufficient for the surge motion due to the similarity of Newman's and QTF close to the surge natural frequency. The opposite behaviour verifies that Newman's approximation is not appropriate for the pitch motion.

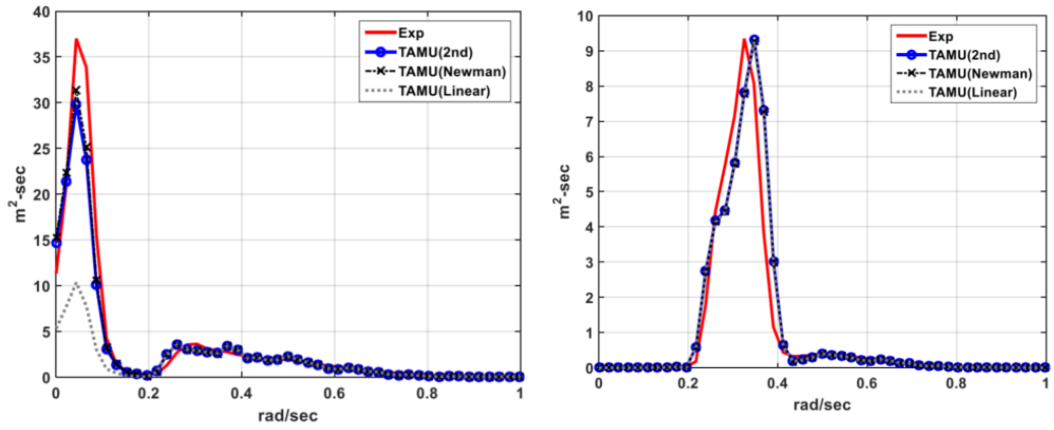

(a) Surge motion spectrum

(b) Heave motion spectrum

Figure 2.4: FWT motions in low white noise spectrum (H. C. Kim and M. H. Kim 2015)

Roald et al. (2013) investigated the effects of second-order hydrodynamics on two FWTs in WAMIT and FAST; the OC3-Hywind spar and UMaine TLP platform. A comparison of first- and second-order response in a specific sea state for both platforms and of the second-order hydrodynamic and aerodynamic effects (only OC3-Hywind) were presented. The second-order forces are small compared to the first-order forces for the spar platform, however, a difference-frequency surge response peak is visible at the surge and pitch eigen-frequencies, due to coupled response. The magnitude of the second-order forces for the TLP are higher, as the heave sum-frequency force is close to the first-order force, which means that the former dominates. The surge and pitch difference-frequency at the eigen-frequencies dominate the overall response, which is explained due to the neglected viscous drag force. The power-spectral densities (PSD) of the spar motion response in surge, heave and pitch due to second-order and aerodynamic forces were computed for 12 environmental conditions. The turbine is configured as rigid, i.e. no structural dynamics are included. It was found that the first-order wave excitation dominates the motion response in the incident wave frequency range. The aerodynamic excitation response dominates for low and high frequencies, however, the high-frequency response is of much smaller importance.

2.4 Effect of Heave Plates

A common approach in design of spar and semi-submersible FWTs in order to minimise the heave motion and acceleration, is to attach heave plates to the bottom of the vertical columns. The heave plates will shift the heave resonance period out of the first-order wave period by increasing it. The heave motion response can also be reduced by increasing the heave damping, which can indeed be achieved by adding heave plates to the base of the cylindrical structures. Further, the added mass is increased by adding heave plates.

During the development of spar and semi-submersible FWT concepts, experimental and numerical studies have been carried out to determine the effects of heave plates in reference to added mass, viscous damping and the Keulegan-Carpenter (KC) number.

Tao and Cai (2003) conducted a numerical study focusing on the effect of the diameter ratio between a spar buoy and attached plate, on the heave damping and added mass. The results demonstrate that the added mass coefficient is strongly dependent on the diameter ratio D_p/D_c, where p = plate and c = column. Thus, the heave natural period increases with increasing added mass, and is higher for large diameter-ratios.

The viscous damping ratio is also investigated, and it was found that the damping is less influenced by the diameter-ratio than the added mass, especially for large diameter ratios. The effect of the plate thickness on the viscous damping ratio is large for small aspect ratios t_p/D_p, where t_p is the plate thickness. The effect is smaller for higher aspect ratios. This is also supported by Tao et al. (2007), who state that, due to viscous effects, an increasing added mass coefficient results from a thinner disk, observed in figure 2.5. Based on this article, a thin heave plate with a large diameter will provide favourable results in regard to high viscous damping and added mass, required that structural integrity and fatigue strength are satisfied.

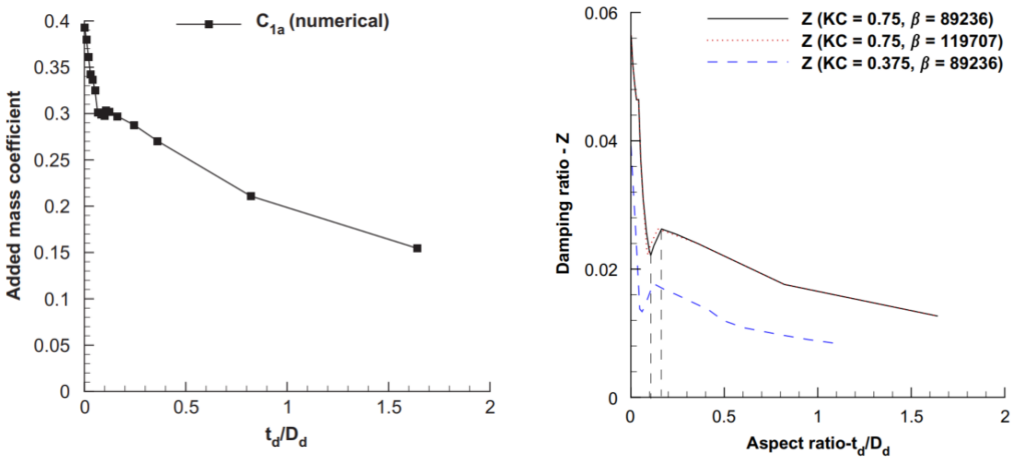

(a) Added mass, KC = 1

(b) Viscous damping ratio

Figure 2.5: Effect of aspect ratio t_p/D_p on added mass and viscous damping ratio (Tao et al. 2007)

Lopez-Pavon and Souto-Iglesias (2015) conducted a study on a design of three vertical columns connected by braces, with a heave plate at the bottom of each column. However, the studies focused on an isolated vertical column with an attached heave plate, thus neglecting any coupling with the braced structure. The authors compared results from an experimental study, a first-order WADAM analysis and a CFD analysis for a range of frequencies and KC-numbers (figure 2.6). The hydrodynamic coefficients are presented as the change in added mass and damping in reference to the theoretical added mass for the combined cylinder-plate-structure. The results indicate that the coefficients are strongly dependent on the KC-numbers, while there is only a weak dependence on the frequency. The observation of KC-dependent hydrodynamic coefficients is also supported by other studies, such as Tao et al. (2007) and Tao and Cai (2003).

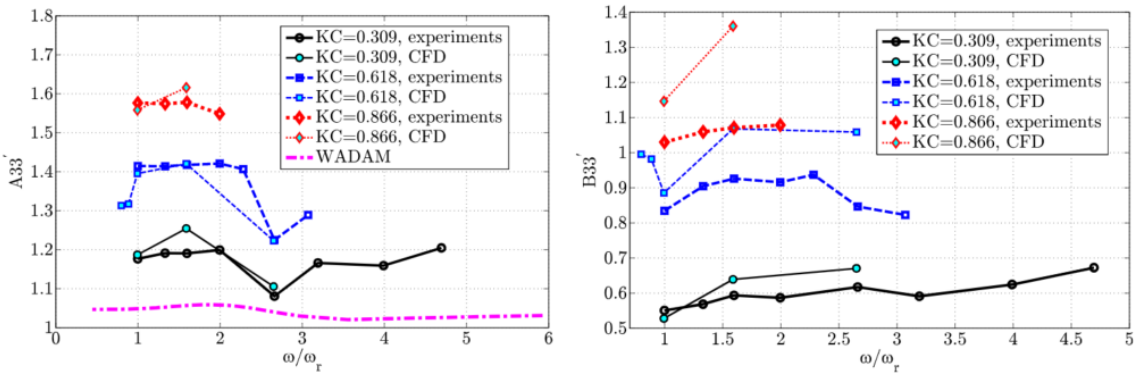

Figure 2.6: Added mass and damping coefficients (Lopez-Pavon and Souto-Iglesias 2015)

Lopez-Pavon and Souto-Iglesias (2015) studied the effect of a reinforced heave plate, compared to a plain plate which is discussed above. A plain plate would not be economically feasible at full scale due to a large required steel thickness, thus, they have to be radially and circularly reinforced. In figure 2.7, the added mass is increased for the reinforced plate compared to the plain plate, however, only for low KC-numbers and the WADAM potential flow computations. The damping is significantly reduced for the reinforced plate, compared to the plain plate.

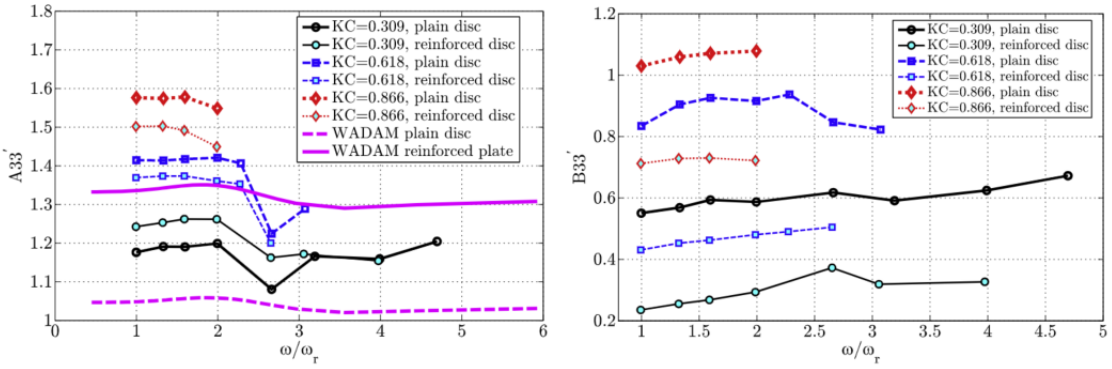

Figure 2.7: Added mass and damping coefficients for plain and reinforced plate (Lopez-Pavon and Souto-Iglesias 2015)

2.4.1 Selection of Heave Plate Added Mass

The viscous terms for the submerged structure are important to determine for time-domain analysis. This contribution is added by the use of slender elements in SIMA. Quadratic drag for the slender elements is calculated based on drag coefficients from Jonkman (2010) and Kvittem (2014) for the spar and semi-submersible platforms, respectively. Added mass was not included for the main part of the simulations. Nevertheless, it was decided to investigate additional added mass of the heave plates of the WindFloat for one simulation case.

In order to account for the viscous-flow effects of the plates on the added mass and damping coefficients, it was decided to lean on previous experimental and numerical studies. The heave plates of the semi-submersible WindFloat are hexagonal. Moreno et al. (2016) conducted a comparative experimental study of hydrodynamic coefficients of hexagonal and circular heave plates attached to a vertical circular cylinder. The structure with the hexagonal heave plate is based on WindFloat, thus, those results were chosen as most relevant for selection of viscous coefficients. The procedure for calculating the additional added mass and the KC-number for the heave plates is based on studies by Lopez-Pavon and Souto-Iglesias (2015) and Moreno et al. (2016), and described in section 6.4.2.

Figure 2.8 presents the added mass and damping coefficients for circular and hexagonal plates for different KC-numbers and oscillation frequencies from the conducted experiments by Moreno et al. (2016). The results support the above discussion that the added mass increases with increasing KC. It is observed that the added mass for the hexagonal plate is somewhat larger than for the circular plate at low KC, however,

this difference is narrowed out for higher KC. Concerning the damping coefficient, the frequency presents a larger variability for both types of plates. In general, the damping is similar for the plates at low KC, but for higher KC, the hexagonal plate seems to have higher damping.

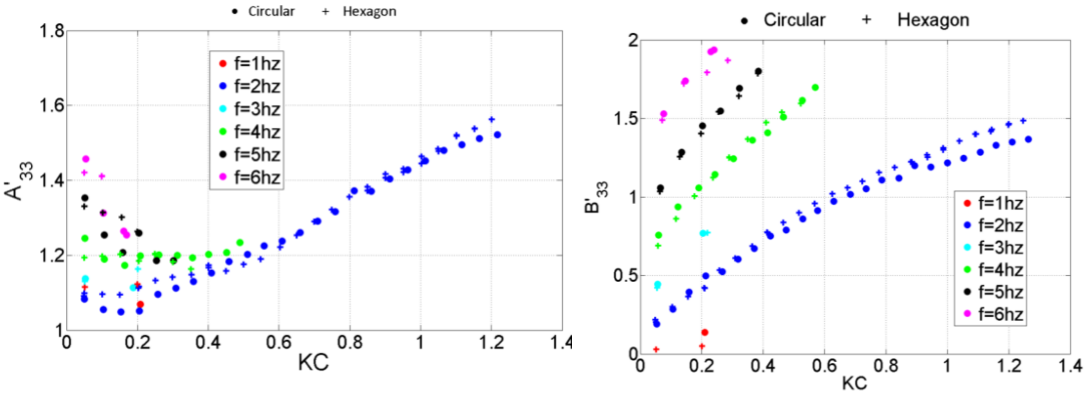

(a) Added mass coefficient

(b) Damping coefficient

Figure 2.8: Hydrodynamic coefficients for circular and hexagonal heave plate (Moreno et al. 2016)

Chapter 3

Theory

3.1 Hydrodynamic

The following subsections describes a broad overview of the hydrodynamic theory used in the numerical model and analysis, and are in general based on theory from the textbook *Sea Loads on Ships and Offshore Structures* by Faltinsen (1993).

3.1.1 Linear Wave Theory

First-order potential theory is used in HydroD to calculate hydrodynamic coefficients. The deep water velocity potential ϕ is applied in line with the scope of the thesis (equation (3.1)). The wave elevation ζ is given in equation (3.2). Here, ζ_a, k and ω are defined as wave amplitude, wave number and angular wave frequency, respectively. The wave number is related to the frequency through the dispersion relation for deep water waves in equation (3.3).

$$\phi = \frac{g\zeta_a}{\omega} e^{kz} \cos(\omega t - kx) \tag{3.1}$$

$$\zeta = \zeta_a \sin(\omega t - kx) \tag{3.2}$$

$$\omega^2 = kg \tag{3.3}$$

The velocity potential is obtained by four boundary conditions (BC): sea-bottom kinematic BC, body kinematic BC, free-surface kinematic BC and free-surface dynamic BC. The two first define impermeability on the sea-bottom and the body. The kinematic BC requires a fluid particle on the free-surface to remain on the free-surface at all times. The dynamic boundary condition requires that the surface water pressure equals the ambient atmospheric pressure.

3.1.2 Statistical Description of Waves

The wave elevation of a long-crested irregular sea wave propagating in the positive x-direction can be represented by superimposing linear regular waves, equation (3.4). Here, ζ_j, ω_j, k_j and ϵ_j define the wave amplitude, circular frequency, wave number and random phase angle, respectively, for wave component j. The wave amplitude is represented in equation (3.5) by the spectrum $S(\omega)$ and the difference-frequency $\Delta\omega$. A

wave spectrum can be estimated from wave measurements, and the two recommended ones are modified Pierson-Moskowitz (PM) and JONSWAP (Joint North Sea Wave Project) spectrum.

$$\zeta = \sum_{j=1}^{N} \zeta_j \sin\left(\omega_j t - k_j x + \epsilon_j\right) \tag{3.4}$$

$$\frac{1}{2}\zeta_j^2 = S(\omega_j)\Delta\omega \tag{3.5}$$

3.1.3 Response in Regular Waves

The hydrodynamic problem in regular waves can then be divided into two sub-problems, defined by Faltinsen (1993):

a) "The forces and moments on the body when the structure is restrained from oscillating and there are incident regular waves. The hydrodynamic loads are called **wave excitation loads** and composed of so-called Froude-Kriloff and diffraction forces and moments."

b) "The forces and moments on the body when the structure is forced to oscillate with the wave excitation frequency in any rigid-body motion mode. There are no incident waves. The hydrodynamic loads are identified as **added mass, damping** and **restoring** terms."

Problem a) is defined as the diffraction problem, and the two force components are obtained by integrating the incident-wave and diffraction dynamic pressure along the mean wetted hull surface. Problem b) is defined as the radiation problem, and the added mass (A) and damping (B) terms are connected with the dynamic pressure while the restoring (C) terms are connected with the hydrostatic pressure.

When the above hydrodynamic properties have been obtained, the equation of motion for a rigid body in water can be written as in equation (3.6), where $\eta_k, \dot{\eta}_k$ and $\ddot{\eta}_k$ are the body motion, velocity and acceleration, respectively:

$$F_j e^{-i\omega t} = \sum_{k=1}^{6} [(M_{jk} + A_{jk})\ddot{\eta}_k + B_{jk}\dot{\eta}_k + C_{jk}\eta_k] \tag{3.6}$$

The two sub-problems can be linearly superimposed to obtain the total velocity potential. The equation of motion can thus be solved in frequency-domain, through equation (3.7). A complex 6x1 translation vector is defined by $\mathbf{X}(\omega, \theta)$, and the matrices **M, C, A** and **B** represent the coefficients of mass, hydrostatic restoring, added mass and damping, respectively.

$$\boldsymbol{F}(\omega, \theta) = \boldsymbol{X}(\omega, \theta)[\omega^2(\boldsymbol{M} + \boldsymbol{A}(\omega)) - i\omega\boldsymbol{B}(\omega) + \boldsymbol{C}] \tag{3.7}$$

3.1.4 Second-Order Non-Linear Effects

In second-order potential theory, all terms in the velocity potential, fluid pressure and wave loads which are proportional to ζ_a or ζ_a^2, where ζ_a is wave amplitude, are kept. The solution is more accurate and consists of the linear solution, mean forces and forces oscillating with difference- and sum-frequencies. For slacked moored FWTs, the difference-frequency forces are important due to the high natural periods, in addition to the mean forces, as explained in chapter 2.

Mean Wave Drift Forces
Mean wave drift forces in a potential flow model are due to "a structure's ability to cause waves" (Faltinsen 1993). For surface-piercing structures in regular waves, the relative vertical motion between the body and the waves causes a non-zero mean pressure, which results in a mean wave force. WADAM can calculate the mean wave forces by conservation of momentum (three horizontal DoFs) or pressure integration (all six DoFs). Equation (3.8) presents the method of conservation of momentum.

$$\bar{F}_i = -\overline{\int\int_{S_\infty} [pn_i + \rho V_i V_n] ds} \tag{3.8}$$

The horizontal force component averaged over one oscillation period is defined as $\bar{F}_i$, where i = 1,2,6. Further, V_i is velocity in the given horizontal direction and V_n the normal component of the fluid velocity at the body surface. S_∞ indicates the time-dependent wetted-surface of a non-moving cylindrical control surface away from the body, while ρ and p denotes the water density and pressure normal to S_∞, respectively. When utilising equation (3.8), only the first-order velocity potential is necessary, as the second-order velocity potential does not contribute to the mean wave force.

Difference-Frequency Forces
Difference-frequency loads excite slow-drift motions in moored structures, which are "resonance oscillations excited by non-linear interaction effects between the waves and the body motions" (Faltinsen 1993). They are important for large-volume structures, and occur in surge, sway and yaw for moored structures. A contribution from the second-order velocity potential is necessary for slow-drift excitation loads, equation (3.9), where F_i^{SV} is the slow-drift force or moment.

$$F_i^{SV} = \sum_{j=1}^{N}\sum_{k=1}^{N} \zeta_j \zeta_k [T_{jk}^{ic} \cos\left((\omega_k - \omega_j)t + (\epsilon_k - \epsilon_j)\right) + T_{jk}^{is} \sin\left((\omega_k - \omega_j)t + (\epsilon_k - \epsilon_j)\right)] \tag{3.9}$$

Here, ζ_j and ζ_k are the wave amplitudes, ω_j and ω_k are the wave frequencies, and ϵ_j and ϵ_k are the random phase angles for the waves. The coefficients T_{jk}^{ic} and T_{jk}^{is} are defined as the second-order transfer functions, dependent on the wave frequencies.

To reduce computational time and effort, Newman (1974) proposed an approximation of the transfer functions to avoid calculating the second-order velocity potential. Newman's approximation, equation (3.10), corresponds to finding the transfer-functions when $(\omega_k - \omega_j)$ is small.

$$T_{jk}^{ic} = T_{kj}^{ic} = \frac{1}{2}(T_{jj}^{ic} + T_{kk}^{ic}) \qquad T_{jk}^{is} = -T_{kj}^{is} = 0 \tag{3.10}$$

Wave Drift Damping
Wave drift damping occurs due to the slow-drift motion in surge, sway and yaw, and can be defined as "the first-order correction in terms of slow-drift velocity of the mean wave drift force" (Finne et al. 2000). It is proportional to the body speed and acts as a damping force in the equation of motion. Due to the coupling between the slow-drift motions in the horizontal plane, the wave drift damping can be presented in a 3x3 matrix $\boldsymbol{B}$. The coefficients in the matrix can be derived from the equations of conservation of momentum.

Viscous Effects
Viscous effects may be important for structures and sea states where the relation between the wave length and the diameter of the structure is large (Faltinsen 1993). The wave loads on slender, fixed structures when viscous forces matter, can be calculated by Morison's equation, however, it is also applied to floating circular cylinders (section 2.1). The force on a horizontal strip of length dz by body position η_1, is calculated for a vertical floating cylinder by equation (3.11).

$$dF = \frac{1}{2}\rho C_D D dz(u - \dot{\eta}_i)|u - \dot{\eta}_i| + \rho C_M \frac{\pi D^2}{4} dz a_i - \rho(C_M - 1)\frac{\pi D^2}{4} dz \ddot{\eta}_i \tag{3.11}$$

The first term is the drag force term with C_D = drag coefficient, the second term is the mass force term with C_M = mass coefficient, and the third term represents the correction of the added mass coefficient $C_A = C_M - 1$. ρ, D, u and a_i represent the water density, cylinder diameter, horizontal undisturbed fluid velocity and acceleration at strip midpoint, respectively.

3.1.5 Mooring Line Analysis

Both the spar FWT and semi-submersible FWT have a catenary mooring system (chapter 4). A spread catenary mooring system is a system where the lines are freely hanging under the influence of gravity, and the bottom part of the line towards the anchor lies on the seabed (figure 3.1). The anchor point is thus only subject to horizontal forces. Through the suspended weight of pre-tensioned mooring lines, the system provides restoring forces and horizontal stiffness on the floating structure.

SIMA calculates mooring line forces by a quasi-static procedure. Quasi-static loads are loads due to the swell, wind, current and the low frequency of the system (Vryhof 2010). The quasi-static procedure can be performed in a time- or frequency-domain simulation. The main difference from static design procedure, is that the latter is non-linear, such that the catenary stiffness at each horizontal offset is applied in the equations of motions.

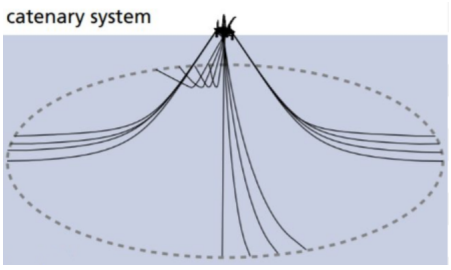

Figure 3.1: A catenary system (Vryhof 2010)

3.2 Aerodynamic

3.2.1 Blade Element Momentum Theory

Blade element momentum theory (BEM) is the most common aerodynamic theory in numerical tools. It is based on the combination of an ideal turbine (the one-dimensional actuator disc model) with wake rotation and lift and drag generation on the air foils (Bachynski 2018). The thrust T and torque Q based on momentum theory are defined in equation (3.12) and (3.13). The induction factors a and a' (rotational) are defined as velocity reduction on the disc, relative to the incoming velocity v_0. The forces normal p_N and tangential p_T to the rotor plane can be identified based on the lift force L, drag force D and the angle ϕ (figure 3.2). Further, Ω and B define the angular rotor velocity and number of blades, respectively.

$$dT = 4a(1-a)\frac{1}{2}\rho v_0^2 2\pi r dr = Bp_N dr = B(L\cos\phi + D\sin\phi)dr \tag{3.12}$$

$$dQ = 4a'(1-a)\frac{1}{2}\rho v_0 \Omega r^2 2\pi r dr = Brp_T dr = Br(L\sin\phi - D\cos\phi)dr \tag{3.13}$$

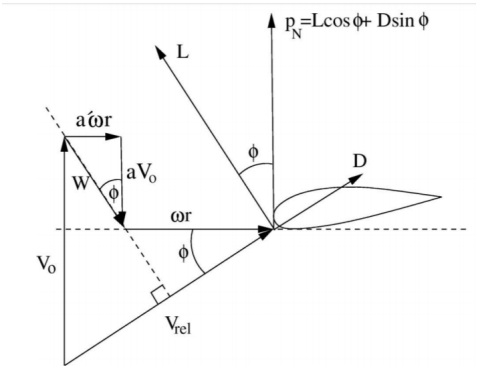

Figure 3.2: Air foil section in the rotor plane (Bachynski 2018)

3.2.2 Corrections to BEM

The BEM theory requires some corrections to provide a good physical representation of the aerodynamics of a wind turbine. These corrections will be described briefly in the following and are based on lecture notes from Bachynski (2018).

The BEM theory assumes an infinite number of blades, which is incorrect. The Prandlt correction factor, or the tip loss factor, corrects for a finite number of blades on the rotor. It describes the loss of aerodynamic force on the blade tip due to the flow moving from the lower to the upper side of the blade, by adding a correction for the relative velocity to the force equations.

For induction factors $a > 0.5$, the BEM-theory is not valid. The Glauert correction adjusts for such cases because the wind velocity in the far-field wake would be negative.

If there is a change in the incoming wind velocity, blade pitch angle or rotor speed, the induction factors will be updated with a time lag. The dynamic wake effect acts as a filter for the induced velocities due to shedding and downstream convection of vorticity. The result is a more physical wake change.

Dynamic stall accounts for the sudden attachment and re-attachment of the flow due to dynamic incoming wind. The lift and drag coefficients are governed by the angle of attack, and will thus change when the angle of attack changes.

In addition, SIMA also implements the tower shadow effects, hub loss and skewed inflow correction. The tower shadow effect models the effect of the tower on the local incoming wind flow, since, as each blade pass by the tower, the thrust will vary. This may lead to fatigue damage. Hub losses correct for the presence of the hub of the turbine, while skewed inflow corrections account for the possible rotor tilt or the yaw angle between the rotor and incoming wind (Ormberg and Bachynski 2012).

3.3 Coupled Time-Domain Analysis

In the following section, the integrated coupled time-domain analysis performed in SIMA will be described. The procedure in SIMA (SIMO/RIFLEX) is explained in section 6.1.

A FWT is subject to several load and response contributions from wind, wave and current. In addition, response from the structural dynamics of the mooring lines and the rotor, and the hydrodynamic characteristics of the floating structure. The interaction of these loads and responses for a floating structure, lead to important coupling effects (Kvittem 2014), which may include the following:

- Aerodynamic damping from the rotor on the motions of the floater.
- The FWT motions may influence the wind force.
- The wind and mooring forces may be influenced by the mean platform position.
- The mooring line dynamics may affect the FWT platform motion.

In coupled time-domain analysis, the rigid body dynamics of the submerged part and the flexible, slender FE-elements for the mooring system need to communicate at every time step. The rigid body and the flexible slender elements are connected at nodes, and the motion equilibrium of the two systems are solved separately, but simultaneously, in time-domain. Thus, external forces and displacements are exchanged between them at every time step (Kvittem 2014).

For a coupled analysis, the results from the hydrodynamic frequency-domain analysis (equation (3.7)) are applied to the time-domain by Cummins equation, equation (3.14). The equation introduces an impulse-response function, called the retardation function $\boldsymbol{\kappa}$. Further, the matrices **M, C, A** and **B** represent the coefficient matrices of mass, hydrostatic restoring, added mass and damping, respectively, and **x** is the rigid body displacement.

$$\boldsymbol{F}_{exc}(t) = (\boldsymbol{M} + \boldsymbol{A}_{\infty})\ddot{\boldsymbol{x}}(t) + \int_0^t \boldsymbol{\kappa}(t-\tau)\dot{\boldsymbol{x}}(\tau)d\tau + \boldsymbol{C}\boldsymbol{x}(t) \tag{3.14}$$

The force vector $\mathbf{F}(t)$ in equation (3.14) for a rigid body with catenary mooring lines and a turbine in a coupled time-domain analysis, consists of non-linear restoring, inertia and damping from the mooring lines, wave forces and inertia and damping forces from the turbine, equation. (3.15).

$$\boldsymbol{F}(t) = \boldsymbol{F}^{\boldsymbol{moor}}(t) + \boldsymbol{F}^{\boldsymbol{wave}}(t) + \boldsymbol{F}^{\boldsymbol{wind}}(t) + \boldsymbol{F}^{\boldsymbol{turb}}(t) + \boldsymbol{F}^{\boldsymbol{visc}}(t) \tag{3.15}$$

3.3.1 Non-Linear FEM

As mentioned above, the FWT response is solved at each time step in time-domain. The structural and dynamic loads of slender, flexible elements are computed in RIFLEX by non-linear finite element methods (Ormberg and Bachynski 2012). These methods take into account the effects of large displacements and cases where the boundary conditions change. Large displacements and quadratic thrust and drag force behaviour may induce geometric structural non-linearities in FWT modelling (Kvittem 2014).

The dynamic equilibrium of a system of finite elements can be described by global matrices containing mass, damping and stiffness properties of the finite elements. The tower and turbine is assumed a stiff structure, while the global mass, damping and stiffness matrices include the properties of the floating body, the rotor blades, hub and mooring lines (computed in HydroD). The governing equation is presented in equation (3.16), where the work by external loads $\boldsymbol{R}_{ext}$ equals the work by inertial, dissipative and internal forces, respectively $\boldsymbol{M}_g\ddot{D}$, $\boldsymbol{B}_g\dot{D}$ and $\boldsymbol{R}_{int}$. D represents the nodal displacements. Equation (3.16) is solved by step-by-step numerical integration in RIFLEX, by using the implicit Newmark-β-method (SINTEFOcean 2018a).

$$\boldsymbol{M}_g\ddot{D} + \boldsymbol{B}_g\dot{D} + \boldsymbol{R}_{int} = \boldsymbol{R}_{ext} \tag{3.16}$$

Chapter 4

The FWT Concepts

4.1 FWT Platforms

There are mainly three concepts of floating wind turbine application in deep water. Technology from onshore wind turbines is combined with known technology on floating structures in the oil and gas industry. All three concepts present different stability criteria, and are illustrated in figure 4.1.

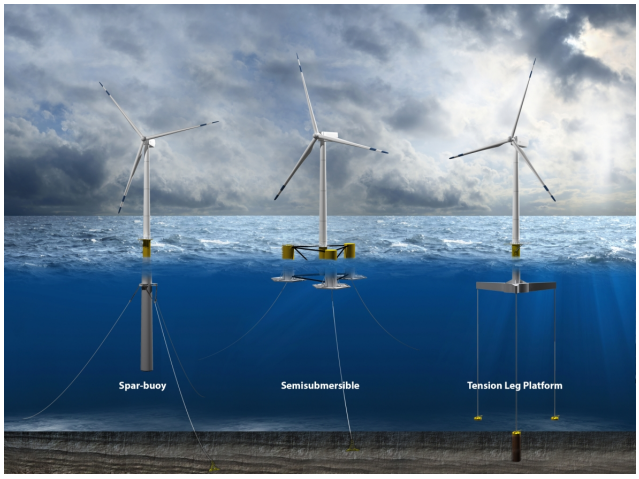

Figure 4.1: A spar, a semi-submersible and a TLP FWT (WindEnergyTechnologiesOffice 2017)

- Spar-buoys: ballast stabilised, intended for deep waters. Designed for small and slow motions, especially in heave due to deep draft and reduced vertical wave excitation forces (Bachynski 2018). Spar FWTs are vulnerable to low-frequency vortex-induced motions due to current-induced dominant loads (DNVGL 2018).
- Semi-submersibles: buoyancy stabilised provided by submerged pontoons, characterised by a small draft and large motions. Due to small water plane area, the vertical natural periods are quite high, and may experience significant wave and low-frequency motions (Roddier et al. 2009).
- Tension-leg platforms (TLP): mooring line stabilised by vertical tensioned tethers which works as a soft spring in surge, sway and yaw and stiff spring in heave,

roll and pitch. The corresponding natural periods are therefore quite high for the former, and low for the latter motions. It is characterised by small motions and may experience horisontal wave-frequency motions (DNVGL 2018).

Two FWTs are to be studied in this master's thesis, and a semi-submersible and a spar are chosen: the modified WindFloat (inspired by Principle Power's semi-submersible concept) and the OC3-Hywind (inspired by Equinor's spar concept). The given semi-submersible platform is chosen as it is close to commercialisation, and a better choice than other similar concepts regarding geometry, weight and access to information. The given spar platform is chosen due to the simple design, and because it is already commercialised, which makes it a natural choice to study.

4.2 OC3-Hywind

Equnior's spar FWT, Hywind from the world's first commercialised floating wind farm, has been used as a basis in several projects for verification and validation of numerical codes. The platform utilised in this thesis is defined by Jonkman (2010) for the OC3-project. The OC3-Hywind platform is somewhat modified for the public project, and scaled to support a 5 MW turbine. Figure 4.2 illustrates Equinor's original Hywind (4.2a) and the modified OC3-Hywind (4.2b).

The tower and turbine is placed 10 m above the still water level (SWL) on top of the spar, and the draft of the spar is 120 m. It consists of two cylindrical regions connected by a linearly tapered conical region. The cylinder region above this transition is smaller than the region below, which reduces the hydrodynamic loads near the surface. The mass of the whole OC3-Hywind system, including platform, tower, turbine and mooring system, balances the buoyancy of the undisplaced platform in still water.

(a) Equnior's Hywind (Equinor 2018) (b) The OC3-Hywind (Jonkman 2010)

Figure 4.2: The spar FWT Hywind

A simplified mooring system is modelled by Jonkman (2010), consisting of three catenary equivalent homogeneous lines, placed with 120° between each line, where one is placed along the positive x-axis. A yaw spring is attached on each line to achieve correct yaw stiffness. Further, all mooring system damping is neglected, which includes the hydrodynamics drag and line-to-seabed drag.

Table 4.1, 4.2 and 4.3 present the platform geometry, mooring line particulars and the reference values for the natural periods, respectively.

Table 4.1: OC3-Hywind platform geometry (Jonkman 2010)

Parameter	Value
Total draft	120 m
Elevation to platform top (above SWL)	10 m
Taper top to SWL	4 m
Taper bottom to SWL	12 m
Upper platform diameter	6.5 m
Lower platform diameter	9.4 m
Platform mass (incl. ballast)	7.466e+06 kg
Center of mass below SWL	(0, 0, -89.92) m

Table 4.2: OC3-Hywind mooring system (Jonkman 2010)

Parameter	Value
Depth to fairleads below SWL	70 m
Radius to anchors from platform centerline	853.87 m
Unstretched mooring line length	902.2 m
Equivalent mass density	77.71 kg/m

Table 4.3: Reference values for the natural period of OC3-Hywind (Jonkman and Musial 2010)

DoF	T_n [s]
Surge	124.3
Sway	124.3
Heave	30.8
Roll	29.2
Pitch	29.2
Yaw	8.3

4.3 Modified WindFloat

A generic model of Principle Power's WindFloat (2 MW turbine) (figure 4.3a) was modified for a 5 MW turbine and presented at the International Conference on Ocean, Offshore and Arctic Engineering in 2011 (figure 4.3b) (Roddier et al. 2011). The numerical model used in this thesis is based on a model by Kvittem (2014), which is slightly modified compared to the model by Roddier et al. (2011), however, the main dimensions are the same.

The modified WindFloat is a semi-submersible FWT with three columns with equal distance between each and heave plates at the bases. The columns are connected by beams and braces. The tower and the turbine are placed on one of the three columns.

The heave plates at the bases of the columns provide additional hydrodynamic inertia to the structure due to the large amount of displaced water when the structure is moving (Roddier et al. 2011). This results in a shift away from the wave energy for the natural periods, and increased viscous damping forces induced by vortices at the plate edges. The latter reduces platform motion in roll, pitch and heave.

(a) The original WindFloat (PrinciplePower 2015)

(b) Modified WindFloat (Roddier et al. 2011)

Figure 4.3: The semi-submersible FWT WindFloat

The WindFloat concept has an active ballast system in order to keep the structure in an upright position, and thus maximise the power output of the system. Water is pumped between the columns with a reaction time of 20 minutes to significant changes in wind speed and direction. The ballast system will have no influence on, or minimise, the roll and pitch motions. The centre of gravity and mass moments of inertia as functions of wind speed are presented in appendix A.2.

The mooring system modelled for the modified WindFloat is based on the system by Kvittem (2014), which is slightly different from the system defined by Roddier et al. (2011). Four catenary mooring lines keep the platform in position, where two lines are connected to the heave plate of the column with the tower and one line on each of the other two columns. Each mooring line consists of three sections, where the top and bottom section is a chain line, while the middle section is polyester rope. A clump weight is connecting the upper chain and the polyester rope.

In table 4.4, 4.5 and 4.6 the main particulars for the modified WindFloat, the particulars of the mooring system and reference values for the natural periods are presented, respectively.

Table 4.4: WindFloat platform particulars (Kvittem 2014)

Parameter	Value
Column diameter	10.0 m
Column center to center	46.0 m
Main beam and pontoon diameter	2.0 m
Brace diameter	1.5 m
Operating draught	17.0 m
Heave plate edge length	15.0 m
Turbine tower foundation above SWL	10.0 m
Pontoon vertical position	-15.0 m
Ballast tank bottom lower level	-13.0 m
Mass (without tower and turbine)	4.019e+06 kg
Center of gravity (whole WT system)	(-0.331, 0, 1.489) m

Table 4.5: WindFloat mooring system (Kvittem 2014)

Parameter	Value
Length upper chain	60 m
Length polyester rope	769.8 m
Length bottom chain	232.58 m
Unstretched mooring line length	1062.4 m
Radius to anchors from centerline	769.99 m

Table 4.6: Reference values for the natural period of the modified WindFloat (Kvittem 2014)

DoF	T_n [s]
Surge	107.0
Sway	124.8
Heave	19.9
Roll	35.6
Pitch	37.4
Yaw	68.5

4.4 5 MW Reference Wind Turbine by NREL

NREL (National Renewable Energy Laboratory) developed specifications for a representative utility-scale multi-megawatt turbine, named "NREL offshore 5-MW baseline wind turbine". The definition is presented by Jonkman et al. (2009), and the technical report defines the basis of the following description of the turbine. The turbine is a "conventional three-bladed upwind variable-speed variable blade-pitch-to-feather-controlled turbine" (Jonkman et al. 2009). The authors collected information and specifications from several available wind turbine designs, and created a composite model from the best collected information. Table 4.7 presents the properties of the representative 5 MW wind turbine. The origin of the coordinate system is based along the centerline of the tower at the mean sea level.

Table 4.7: Properties for the 5 MW NREL wind turbine (Jonkman et al. 2009)

Parameter	Value
Rating	5 MW
Rotor diameter	126 m
Hub height	90 m
Cut-in, rated and cut-out wind speed	3 m/s, 11.4 m/s, 25 m/s
Cut-in and rated rotor speed	6.9 rpm, 12.1 rpm
Rotor mass	1.1e+05 kg
Nacelle mass	2.4e+05 kg
OC3-Hywind tower mass	2.497e+05 kg
Center of mass (overall)	(-0.2, 0, 64) m

Chapter 5

Environmental Conditions

5.1 Location

In line with the scope of the master's thesis, a suitable location for FWT operation was necessary to be defined in order to carry out the numerical investigations. Due to the aim of investigating FWTs during extreme environmental conditions, the water depth is an important factor as the environmental loads are generally larger at deeper water. In the project thesis, the chosen location was the Tampen area in the northern North Sea (figure 5.1a). The area has a water depth of 300-350 m, as seen by the marked cross in figure 5.1b. This depth suits the scope of the thesis with respect to deep water. The met-ocean data for this location was provided by Equinor (Kvingedal and Mathiesen 2010).

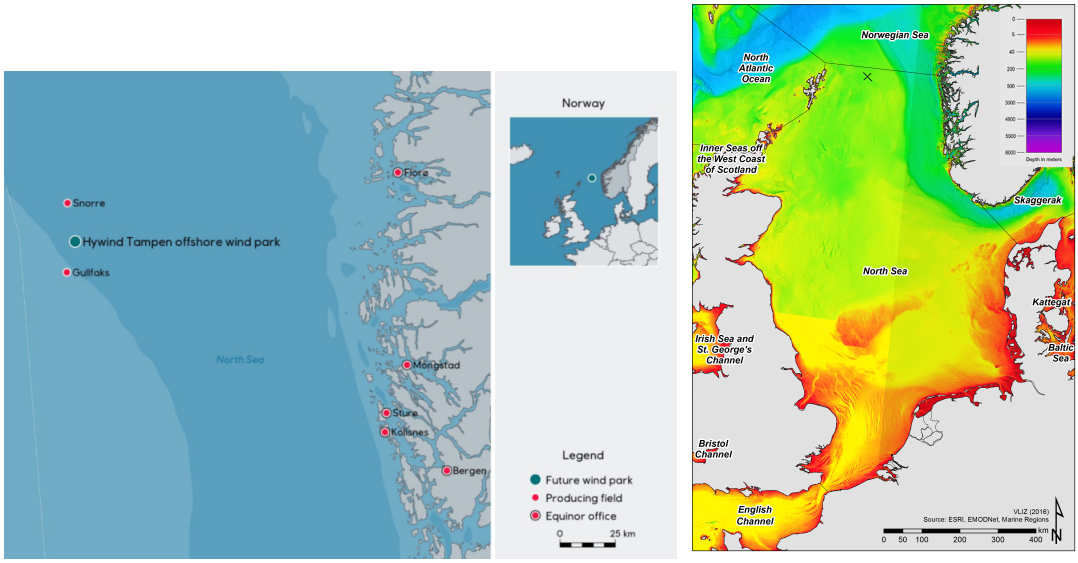

(a) The Tampen area (Kvingedal and Mathiesen 2010)

(b) Bathymetry of the North Sea (VLIZ 2016)

Figure 5.1: The chosen location for definition of environmental conditions

5.2 Theory Environmental Conditions

According to Kvingedal and Mathiesen (2010), all the seasonal/directional extremes are lower than the marginal extremes (all seasonal and omni-directional). When predicting extreme structural response for design purposes, it shall be verified that the obtained extreme response is in agreement with overall requirements regarding annual exceedance probabilities. Thus, to calculate the marginal exceedance probability of a given response level as a weighted sum of the exceedance probabilities for the various direction sectors, would be the correct approach.

In the following section, the theory of the long-term and short-term statistics will be defined. The theory yields for both wind, wave and current, and the parameter values are calculated from the met-ocean report from Equinor (Kvingedal and Mathiesen 2010).

5.2.1 Long-Term Statistics

The long-term distribution $F(x)$ of the wind speed, the significant wave height and the current speed (here represented by the generic x) is modelled with a 3-parameter Weibull-distribution, equation (5.1). The corresponding extreme value for a given return period R, equation (5.2), is obtained by inverting the long-term distribution for a cumulative probability.

$$F(x) = 1 - \exp\left[-\left(\frac{x-\alpha}{\beta}\right)^{\gamma}\right] \tag{5.1}$$

$$x_R = \alpha + \beta\left(-\ln\left(\frac{\tau}{pR}\right)\right)^{1/\gamma} \tag{5.2}$$

The expected value of x for the 3-parameter Weibull-distribution, is given in equation (5.3). The Weibull-parameters are defined as listed below.

$$E[x] = \alpha + \beta\Gamma\left(\frac{1}{\gamma} + 1\right) \tag{5.3}$$

α = location parameter
β = scale parameter
γ = shape parameter
τ = duration of event
p = sector or monthly probability

Joint Distribution for a Sea State
The long term sea state can be described by the joint probability density function of the significant wave height H_s and the spectral peak period T_p, given by equation (5.4). The mean value μ and variance σ^2 are defined in equation (5.5). The parameters a_i and b_i, and the mean spectral peak period given significant wave height, are tabulated.

$$f_{H_s,T_p}(h_s, t_p) = f_{H_s}(h_s) \cdot f_{T_p|H_s}(t_p|h_s) \tag{5.4}$$

$$\mu = a_1 + a_2 h_s^{a_3} \qquad \sigma^2 = b_1 + b_2 \exp\left[-b_3 h_s\right] \tag{5.5}$$

Joint Distribution of Wind and Waves
Li et al. (2015) describe the joint distribution of wind speed U_w, the significant wave height H_s and the spectral peak period T_p, presented in equation (5.6). It consists of the marginal distribution of U_w, a conditional distribution of H_s given U_w, and a conditional distribution of T_p given H_s and U_w. The method is tested at a site in the North Sea which corresponds well with the chosen location, i.e the parameter values and subsequent computed values for the wind and waves are given for that location.

$$f_{U_w,H_s,T_p}(u,h,t) = f_{U_w}(u) \cdot f_{H_s|U_w}(h|u) \cdot f_{T_p|U_w,H_s}(t|u,h) \tag{5.6}$$

The marginal probability distribution function (PDF) of the wind speed is given by the Weibull distribution, while the conditional PDF of the significant wave height is given as a two-parameter Weibull distribution, i.e. the location parameter is zero. The shape and scale parameters are given as power functions of the mean wind speed with estimated parameters for the given location, equation (5.7).

$$\gamma = c_1 + c_2 u^{c_3} \qquad \beta = d_1 + d_2 u^{d_3} \tag{5.7}$$

The conditional PDF of the spectral peak period is lognormal distributed, and the parametrization of T_p is based on the method suggested by Johannessen et al. (2001). The mean value of T_p can then be calculated by equation (5.8).

$$\mu_{T_p} = \bar{t}(h)\left(1 + \theta\left(\frac{u - \bar{u}(h)}{\bar{u}(h)}\right)^{\gamma}\right) \tag{5.8}$$

5.2.2 Short-Term Statistics

A short term distribution is often defined as the probability distribution of wave heights/wind speed within a short time period, such as a wave/wind recording or sea state.

Wave Spectrum
According to Kvingedal and Mathiesen (2010), a sea state at the given location may be modelled by the directional spectrum $S(f,\theta)$, as in equation (5.9), where $S(f)$ is the frequency spectrum and $D(\theta)$ is the direction distribution.

$$S(f,\theta) = S(f)D(\theta) \qquad \int_0^{2\pi} D(\theta)d\theta = 1 \tag{5.9}$$

The frequency spectrum can be defined by the Torsethaugen frequency spectrum, as a sum of the frequency spectrum for the swell and the wind seas contribution. It is a modified JONSWAP spectrum, where the Torsethaugen spectrum decays according to

f^{-4} instead of f^{-5} as the JONSWAP spectrum does. For pure wind seas, the JONSWAP spectrum can be used.

Wind Spectrum
The spectrum of the wind speed at the chosen location is given as a 1-point wind spectrum, which defines the spectral density of the longitudinal wind speed fluctuations. $S(f)$ is defined as the spectral density at frequency f [Hz].

5.2.3 Wind Profile

The 1-hour mean wind speed at height z above the sea level ($z = 0$), $U(z)$, can be presented as a wind profile, as in equation (5.10). The wind profile is implemented as mean wind speeds from $z = 0$ to $z = 200m$ to reach above the highest point on the blades of the wind turbines.

$$U(z) = U_0 \left(1 + C \ln \frac{z}{10}\right) \qquad C = 5.73 \cdot 10^{-2} \sqrt{1 + 0.15 U_0} \tag{5.10}$$

5.3 Environmental Load Cases

The standard 61400-3-2 by International Electrotechnical Commission (IEC 2019b) defines design requirements for floating offshore wind turbines. Certain design situations and load cases are characterised, in addition to the ones defined for fixed offshore wind turbines in part 3-1 (IEC 2019a), which should be considered in design of FWTs. The following environmental load cases are inspired by the load cases by IEC (2019b). The design situations in this thesis will be considered as power production (LC1, LC2) and extreme conditions with parked turbine (LC3-LC6), i.e. no fault conditions will be applied. See table 5.1 for the values of wind, waves and current.

Consequently, it was thus decided to define six environmental load cases for the investigation of the two FWTs:

- LC1: Expected operational condition for the given location
- LC2: Maximum operational condition, i.e. at cut-out wind speed $U_w = 25m/s$
- LC3: Extreme condition with 50-year return period, wind speed direction = 0°
- LC4: Extreme condition with 50-year return period, wind speed direction = 90°
- LC5: Extreme condition with 100-year return period, wind speed direction = 0°
- LC6: Extreme condition with 100-year return period, wind speed direction = 90°

All of the load cases are presented with a wind turbulence model, a wind speed U_w at hub height $z = 90m$ above MSL, significant wave height H_s, spectral peak period T_p and current speed U_c at $z = -5m$ below MSL. The waves are defined as head waves, i.e. the direction is 0°. The wind is either defined as aligned or misaligned at 90° with the waves.

LC1 is based on met-ocean data from Kvingedal and Mathiesen (2010). The Weibull-parameters are tabulated so that the expected wind speed can be calculated by equation (5.3). This process is also applied to the computation of H_s, while T_p is found through the joint distribution of a sea state described in section 5.2.1. The expected current speed follows the same method as for the wind speed and wave height.

The starting point for LC2 is the cut-out wind speed at hub height, i.e. $U_w = 25m/s$ at $z = 90m$. The wind speed at a height 10 m above MSL is calculated from the given wind profile (Kvingedal and Mathiesen 2010). The significant wave height and spectral peak period are calculated by the method of joint distribution of wind and waves by Li et al. (2015), described in section 5.2.1. The current speed is defined by the Weibull-parameters and the expected value.

The extreme values of LC3-LC6 for the wind speed, significant wave height and current speed are calculated by equation (5.2) with Weibull-parameters from Kvingedal and Mathiesen (2010), for direction 0° and 90°. The spectral peak period is found by the joint distribution of H_s and T_p. The turbulence model for the four extreme load cases are all defined as normal turbulence model (NTM), but with the calculated extreme wind speed for either 50- or 100-year return period. This is due to the definition of the extreme wind speed model (EWM) by IEC (2019a), and proposed by co-supervisor Erin Bachynski.

Table 5.1: Environmental Load Cases

	Wind			Waves			Current	
Case	Model	$U_{w,z=90}$ [m/s]	Dir. [°]	H_s [m]	T_p [s]	Dir. [°]	$U_{c,z=-5}$ [cm/s]	Dir. [°]
LC1	NTM	10.46	0	2.30	9.51	0	18.34	0
LC2	NTM	25.00	0	6.27	11.43	0	18.34	0
LC3	NTM	38.93	0	13.80	16.50	0	95.07	0
LC4	NTM	27.37	90	13.80	16.50	0	95.07	0
LC5	NTM	41.14	0	14.51	16.91	0	99.40	0
LC6	NTM	29.41	90	14.51	16.91	0	99.40	0

Chapter 6

Methodology

6.1 Software

In order to perform a coupled aero-hydro-servo-elastic analysis of a FWT, a numerical model must be set up by utilising available state-of-the-art software. The numerical analysis was conducted in the steps outlined below, and in figure 6.1.

- Modelling of the geometry and generation of finite element panel models in GeniE.
- The panel models were imported into HydroD, and hydrodynamic analyses were performed by the WADAM-wizard.
- Coupled time-domain aero-hydro-servo-elastic analyses were performed in the SIMA-workbench using a SIMO/RIFLEX-coupling.

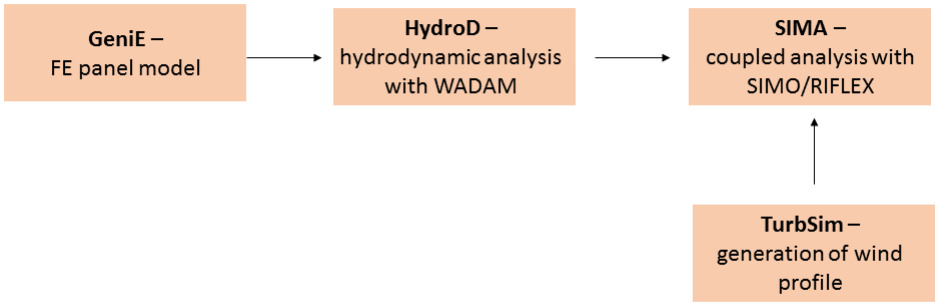

Figure 6.1: Flow diagram for building the numerical model

6.1.1 GeniE

GeniE is a part of the DNV GL software package SESAM, and is a tool built for design and analysis of offshore and maritime structures (DNVGL 2015b). It offers a fast modelling process integrated with advanced strength assessment. The software supports work phases from initial concept studies, such as finite element mesh generation, to complex design, analysis and load calculation. For FWT design, and in this master's thesis, GeniE is used to design and model the geometry of the two FWT platforms. For the semi-submersible WindFloat, the inclined braces are excluded from the model in GeniE due to computational efficiency. Due to the small diameter, their contribution to the future analyses could be neglected. GeniE was further used to generate finite element panel models of the sub-structures and the free surfaces, described in section 6.2.

6.1.2 HydroD

HydroD is an analysis tool developed by DNV GL and is part of the SESAM package. It is an application for computations of hydrostatics, stability, wave loads and motion response for ships and offshore structures (DNVGL 2016). Both frequency and time-domain analyses are available. Frequency-domain hydrodynamic analyses can be performed by WADAM (Wave Analysis by Diffraction and Morison Theory), which uses Morison's equation for slender structures, and first- and second-order 3D potential theory for large volume structures.

6.1.3 SIMA

The SIMA-workbench is a numerical tool developed by SINTEF Ocean, for modelling, simulation and analysis of marine operations and floating structures (SINTEFOcean 2018b). The software allows for coupled aero-hydro-servo-elastic analysis of FWT systems in time-domain. SIMA consists of two engines where the different parts of the coupled analysis are carried out. In SIMO, the simulation and analysis of motions and station-keeping behaviour of large-volume floating structures are performed. The hydrodynamic calculations are based on a combination of potential flow theory in frequency domain and distributed Morison elements, including second-order wave loading (see section 3.1). The mooring line calculations are performed by a quasi-static analysis, and a simplified dynamic analysis accounting for the effect of drag loading on the lines (SINTEFOcean 2018b). In RIFLEX, the structural and dynamic response of slender, flexible marine structures are computed and analysed by non-linear finite element methods for time-domain analysis (Ormberg and Bachynski 2012). The aerodynamic input is computed in a stand-alone software called TurbSim, developed by NREL, and then implemented in a separate module in RIFLEX. The aerodynamic output is calculated by the BEM-theory through the RIFLEX-engine (Ormberg and Bachynski 2012). The workflow in the SIMA-workbench is presented in figure 6.2 (Bachynski 2018).

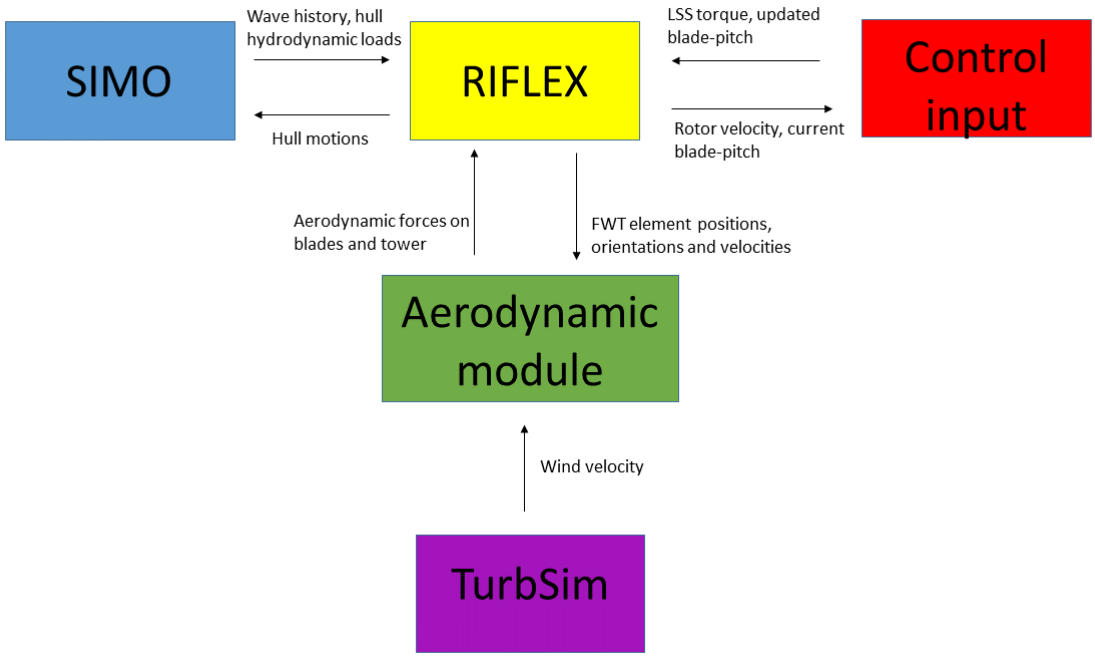

Figure 6.2: Flow chart for the coupled analysis in SIMA

6.2 Panel Models in GeniE

The hydrodynamic models of the two FWT concepts have been generated in the design and analysis tool GeniE. The geometry of the semi-submersible WindFloat is based on the model by Kvittem (2014), presented in section 4.3. The model was simplified by excluding the inclined braces between the main columns in the model, as their contribution to the hydrodynamic analyses performed in HydroD were deemed negligible. The geometry of the spar concept is based on the description by Jonkman (2010), presented in section 4.2. To increase the computational efficiency during the analyses in HydroD, the structures were modelled symmetrically. The spar was modelled symmetrically in both the xz- and yz-plane ($\frac{1}{4}$ of the body), while the semi-submersible was modelled symmetrically in the xz-plane ($\frac{1}{2}$ of the body). In figure 6.3, the top view and the coordinate system of the two concepts are presented.

After defining the geometries, the bodies were discretized into a finite element panel model using a wet surface loading condition. Figure 6.4 illustrates the discretised FE panels models. The upper limit of number of elements a FE panel model may consist of is 15 000, and both 3- and 4-noded elements are accepted. In addition, the wet surface of the models need to have a hydro pressure, pointing from the fluid onto the model.

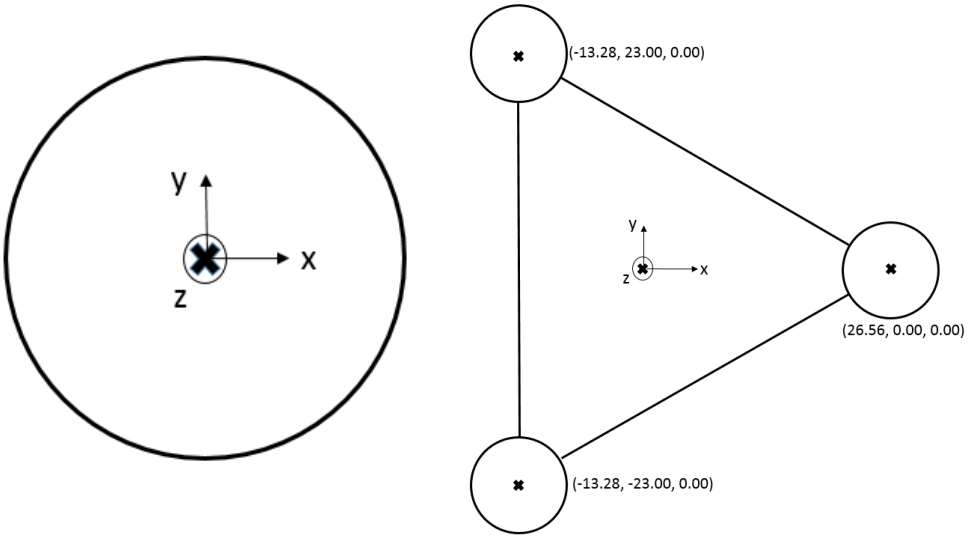

(a) OC3-Hywind (b) WindFloat

Figure 6.3: Top view of the concepts. The waterline is at z=0.

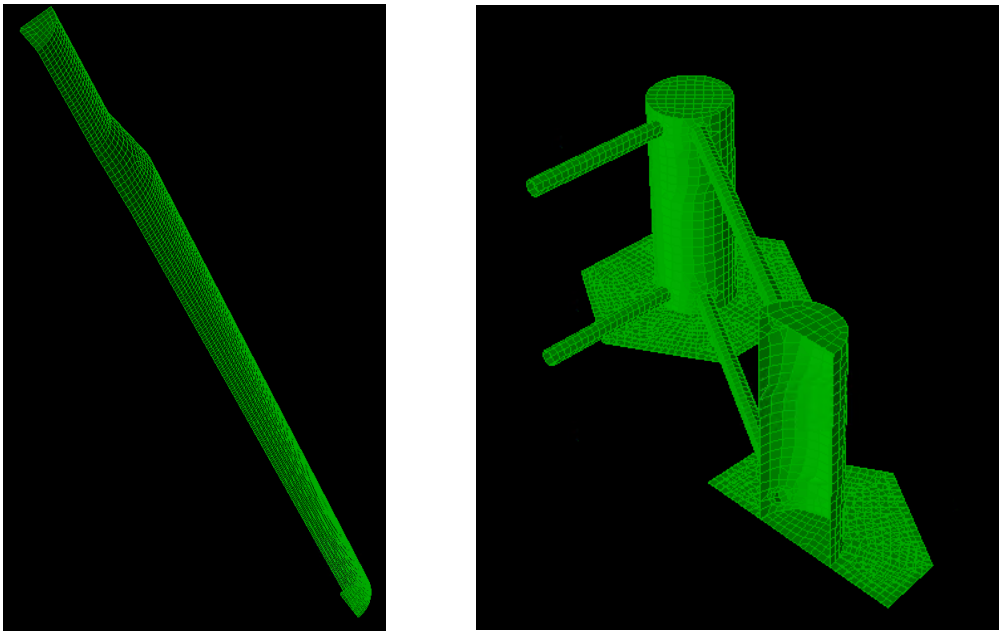

(a) OC3-Hywind (b) WindFloat

Figure 6.4: Discretised FE panel models

6.2.1 Finite Element Free Surface Models

In order to perform a second-order difference-frequency analysis in HydroD, a finite element model of the free surface (FS) had to be generated. The free surface was designed and discretised in GeniE with a hydro pressure load case in the negative z-direction. The FS-model was modelled with the same symmetry as the structures with cut-outs for the surface-piercing components. Both free surface models are presented in figure 6.5. To investigate the quality of the FS-mesh, three parameters were considered:

- A limit of 10 000 panels for the free surface model.
- The current version of HydroD does not accept triangular elements in the free surface mesh, thus, only 4-noded elements are valid.
- The radii R_1 and R_2 of the outer boundaries of the free surface should be determined according to the decaying rate of local waves (DNVGL 2015c). An appropriate approximation in deep water is $R \sim O(\lambda)$, where λ is the longest wave length involved. The radii of the two free surfaces were set to 250 m, which corresponds to a wave with $T = 12.65s$ and $\omega = 0.496rad/s$. Thus, the lower limit of the frequency set for second-order analyses was set to $0.5rad/s$.

6.2.2 Mesh Quality

As mentioned above, the panel model and the free surface mesh can consist of 15 000 and 10 000 elements, respectively. However, due to computational efficiency, it was decided to apply less elements in both cases. The mesh of the structures were verified by computing the mean drift forces on the body surfaces by two methods; pressure integration and conservation of fluid momentum. The verification of the mesh quality of the structures is presented in section 7.1.

The modelling of the free surface mesh focused on obtaining a fine grid close to the columns of the structures. It proved difficult to obtain a free surface with only 4-noded elements, especially regarding the semi-submersible platform. The second-order analyses performed in HydroD were used to verify the free surface mesh. A mesh refinement study was performed for the free surface models to obtain corresponding results from full-QTF computation and Newman's approximation (see section 6.3). The final number of elements for the structures and the free surfaces are presented in table 6.1. The respective numbers are valid for $\frac{1}{2}$ and $\frac{1}{4}$ of the structure and FS.

Table 6.1: Number of elements in the respective mesh models

	Structure	Free surface
OC3-Hywind	3582	2881
WindFloat	5024	6075

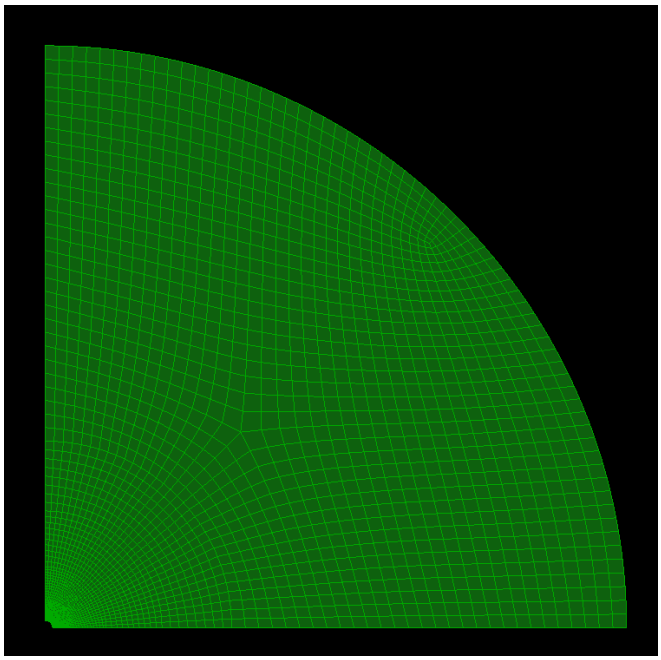

(a) OC3-Hywind FS

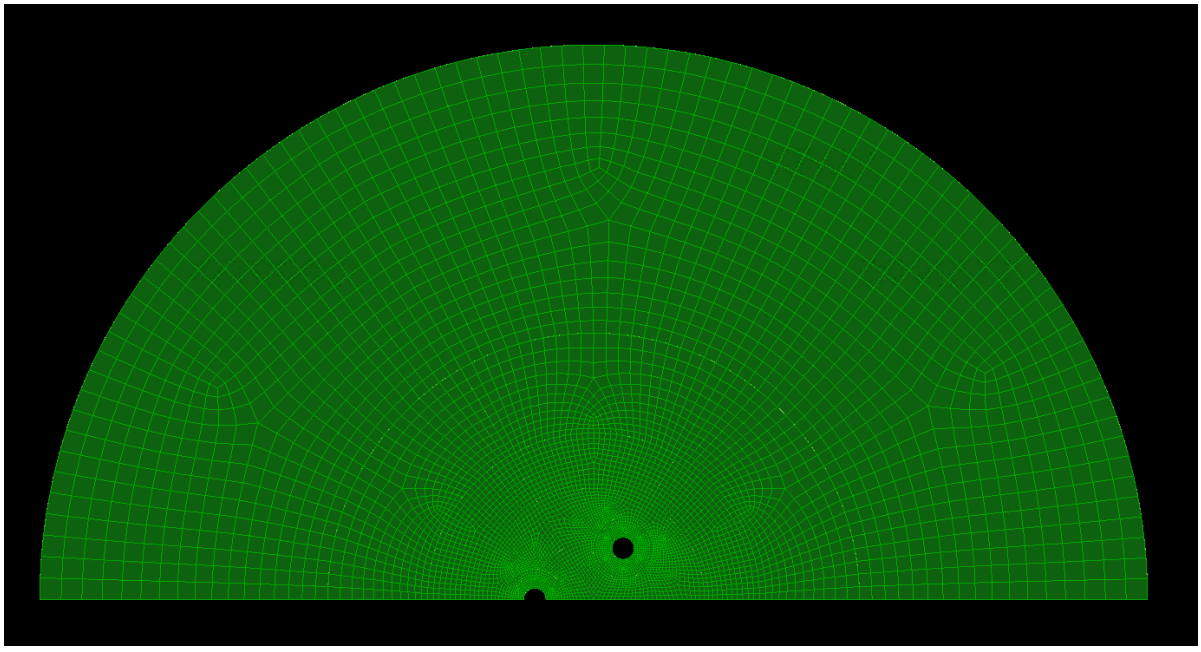

(b) WindFloat FS

Figure 6.5: Discretised FE free surface models in GeniE

6.3 Frequency-Domain Analysis in HydroD

The finite element panel models and free surface models generated in GeniE were imported into HydroD, where frequency-domain hydrodynamic analyses were performed in the WADAM-engine as explained in section 6.1.2. To calculate first-order radiation and diffraction effects on large volume structures, first-order potential theory is applied. Second-order potential theory is utilised to compute the difference-frequency second-order forces and moments and rigid body motions in the presence of bi-chromatic and bi-directional waves (DNVGL 2015c). The output of the analyses consist of the following:

- Mass matrix and hydrostatic stiffness for the floating structures
- Frequency-dependant added mass and damping
- Total excitation forces and moments
- First-order response amplitude operator
- Horizontal mean drift forces and moments in surge, sway and yaw
- Quadratic transfer functions for difference-frequency forces and moment in surge, heave and pitch
- Wave drift damping in surge, sway and yaw

The frequency-domain hydrodynamic data is calculated for the submerged parts of the hull of the FWTs. The hull displacement thus correspond to the total weight of the FWT system. This includes the rotor, hub, nacelle, tower and mooring lines. The mass, centre of gravity and moment of inertia were therefore computed for the total system. In addition, an additional restoring matrix was included to compensate for the mooring line stiffness. The mooring stiffness matrix for the OC3-Hywind is taken from Jonkman (2010). For the WindFloat, additional mooring stiffness is only applied in surge, based on a study by Kvittem and Moan (2015).

6.3.1 First-Order Frequency Domain

The output of the first-order analysis in HydroD consisted of matrices of the added mass coefficients, damping coefficients, excitation forces and moments, the mean drift forces/moments calculated by conservation of momentum, and the response amplitude operators (RAO). The analyses were performed for one wave heading, namely 0°, and 60 frequencies from 0.05-3 rad/s with $\delta\omega = 0.05$. To verify the models, the obtained added mass coefficients, damping coefficients and excitation forces and moments for the OC3-Hywind were compared with results from the definition report on OC3-Hywind (Jonkman 2010). The correspondence between the results was satisfying. The obtained excitation forces for the modified WindFloat were compared to the excitation forces for the model by Kvittem (2014). The correspondence was once again satisfying. In addition, the eigenperiods for the two structures were compared against the values presented in table 4.6 and 4.3. The comparison is given in section 7.1.

6.3.2 Second-Order Frequency Domain

Second-order hydrodynamic analyses were performed in HydroD to obtain the difference-frequency excitation forces and moment in surge, heave and pitch. The forces and moment were calculated by both the quadratic transfer function (QTF) and Newman's approximation. The difference-frequency effect occurs due to the difference between two frequencies, meaning that all valid combinations of the frequency input were subject for analysis. Consequently, implementing the same frequency range as for first-order analysis would be costly in regards to time and computational efficiency. It was therefore decided to define a shorter range of frequencies with less frequencies, i.e. from 0.5-1.5 rad/s with $\delta\omega = 0.04$.

The analysis was performed to do a preliminary investigation if a full QTF time-domain analysis in SIMA would be required, or if the Newman's approximation was sufficient when computing the difference-frequency excitation forces. The validity of the approximation is based on the assumption that the frequency-difference is small due to the involved error which is in the order $O(\delta\omega^2)$ (Duarte et al. 2014). Therefore, Newman's approximation is normally valid in calculation of difference-frequency forces for large offshore systems in deep waters with large natural periods (above 100 s). However, for lower natural periods, the errors involved may lead to unacceptable results for design purposes.

In addition to the difference-frequency forces, the mean wave drift forces and the wave drift damping are computed during the second-order hydrodynamic analysis. The mean drift forces are computed by both pressure integration and conservation of fluid momentum, while the wave drift damping is computed by conservation of fluid momentum. The results are presented in section 7.1.

6.4 Coupled Dynamic Analysis in SIMA

The models for the aero-hydro-servo-elastic analysis was completed in the SIMA-workbench. The results of the frequency-domain hydrodynamic analyses were imported into SIMA as a SIMO-body, so that the output of the WADAM-analysis was imported as a nodal component in a dynamic analysis. Further, the floating body was connected to the tower, the turbine and a catenary mooring system.

The models of the tower, turbine and mooring system were provided by co-supervisor Erin Bachynski. The implemented turbine is the NREL 5 MW turbine, described in section 4.4 (Jonkman et al. 2009). The catenary mooring systems for WindFloat and OC3-Hywind are defined by Kvittem (2014) and Jonkman (2010), respectively. The mooring lines are applied as Morison elements. The master-slave-technique is utilised, by defining the fairleads as slaves with the floating structure as their master. This technique is also applied to the connection between the tower and the floating structure with the tower base as slave.

Some corrections had to be made to the hull hydrostatic data. The frequency-domain hydrodynamic results from the analyses in HydroD correspond to the total weight of the FWT systems, and the values in SIMA have to correspond to only the floating

sub-structure weight. The modified data in SIMA coincides with the values presented in table 4.4 and 4.1.

The active ballast system of the WindFloat FWT is included in the numerical model in SIMA by making the structural mass model a function of the mean wind speed at hub height, i.e. by modifying the platform inertia and centre of gravity. The values for the ballast system are presented in appendix A.2, for the floating hull alone.

In addition to the modifications to the platform hulls, turbine control files, turbulent wind files and viscous drag contributions had to be implemented in the numerical models. This will be described in the following sections.

6.4.1 Wind and Control Input

The turbulent wind input to the time-domain analysis in SIMA is generated by the stochastic, full-field, turbulent-wind simulator TurbSim, developed by NREL (Jonkman 2009). The generated input is based on the environmental load cases presented in section 5.3. A separate file containing wind velocities for each load case is written, and accordingly imported into SIMA.

In TurbSim, the wind input files are generated as a box containing 2D-grids of instantaneous wind velocity of the incoming wind. Each grid contains the whole area which the rotor covers, and the hub and rotor are assumed to be centred horizontally on the grid. The size of the grid is defined to be a 160 m x 160 m square, as the rotor radius is 63 m. Each grid contains a matrix of 32 grid points vertically and horizontally, containing a 3D velocity vector.

In addition, a file containing input for the wind turbine control system is imported. This file is provided by co-supervisor Erin Bachynski. For the given turbine, the power-production control approach relies on a generator torque controller in the below-rated wind-speed range and a full-span rotor-collective blade-pitch controller in the above-rated range. The goal below the rated wind speed is to maximise the power capture, while the goal above rated wind speed is to regulate the generator speed.

6.4.2 Non-Linear Viscous Drag Contribution

The contribution to the quadratic drag term in Morison's equation ((3.11)) was taken into account by discretising the submerged bodies into slender elements in SIMA. The spar platform was divided into three elements; the lower part of the hull, the truncated cone and the upper submerged and above-water part of the cylindrical hull. The semi-submersible platform is divided into 12 slender elements: three vertical circular cylinders for the surface-piercing columns, three vertical circular cylinders corresponding to the heave plates and six horizontal circular cylinders corresponding to the horizontal pontoons. The contribution from each element is added together by strip theory.

Table 6.2 presents the slender elements in SIMA for both structures. L [m] is the length of the element in vertical direction (the length of the horizontal pontoons is therefore not given here), D [m] is the diameter of the components, z_1 and z_2 are the vertical coordinates of the components and C_D is the hydrodynamic quadratic drag

coefficient. The latter is taken from Jonkman (2010) and Kvittem (2014) for the spar OC3-Hywind and semi-submersible WindFloat, respectively.

For one selected environmental load case, the viscous forces for the WindFloat are defined through the procedure presented in section 6.5.2.

Table 6.2: Slender elements in SIMA

OC3-Hywind					
	L [m]	D [m]	z_1 [m]	z_2 [m]	C_D [-]
Lower part of hull	108	9.4	-120.0	-12.0	0.6
Tapered part of hull	8	9.4 $\rightarrow$ 6.5	-12.0	-4.0	0.6
Upper part of hull	14	6.5	-4.0	10.0	0.6

WindFloat					
	L [m]	D [m]	z_1 [m]	z_2 [m]	C_D [-]
Heave plates	0.4	30.0	-17.0	-16.6	7.5
Columns	26.5	10.0	-16.5	10.0	1.0
Submerged pontoons	-	2.0	-15.0	-15.0	1.0
Above-water pontoons	-	2.0	8.0	8.0	1.0

6.5 Heave Plate Modelling for WindFloat

6.5.1 Selection of Heave Plate Thickness

There was limited available information on the design of the heave plates in the published literature, due to the patented design by PrinciplePower (2015). In reality, the heave plates are more complex than just a plain plate as is modelled in this thesis. They are reinforced radially and circularly, as seen in figure 6.6a. Kvittem (2014), who's PhD-thesis is utilised in this master's thesis as a basis for designing the semi-submersible WindFloat, reported an effective heave plate thickness of 0.05 m and modelled the plates without reinforcements. Roddier et al. (2011) did not mention any details about the heave plates, except the length of the plate edges. Roddier et al. (2009) do not present any structural geometry for the floating sub-structure. Aubault and Cermelli (2009) base the structural design of the heave plates on previous heave plate studies within the oil and gas industry, and define the size of stiffeners and stringers based on similar results. Structural optimisation of the heave plates are mentioned as a way of enhancing the economy of the project, however, it is emphasised that "the penalty for over-design of the heave plates is relatively minimal, as additional steel located at the vessel keel contributes to the platform stability, and can be compensated by ballast water, the largest weight contribution to the platform once installed" (Aubault and Cermelli 2009).

A heave plate thickness of 0.05 m provided challenges with regard to numerical results, local mesh refinement and the computational effort. Thus, based on the literature research presented in section 2.4 and the above-mentioned information, it was decided to

model the heave plates as plain plates, but with a larger thickness. With an equivalent diameter of the hexagonal heave plate to a circular plate, the plate-diameter/column-diameter ratio corresponded well with Moreno et al. (2016). Because of the similarity, and the fact that they provided results for a hexagonal heave plate, it was decided to choose a heave plate thickness which would give a similar aspect ratio to what Moreno et al. (2016) presented. In addition, it was desired to use the results from that particular study for an investigation on the corrected added mass and KC-number of the heave plates for one simulation case, described in section 6.5.2.

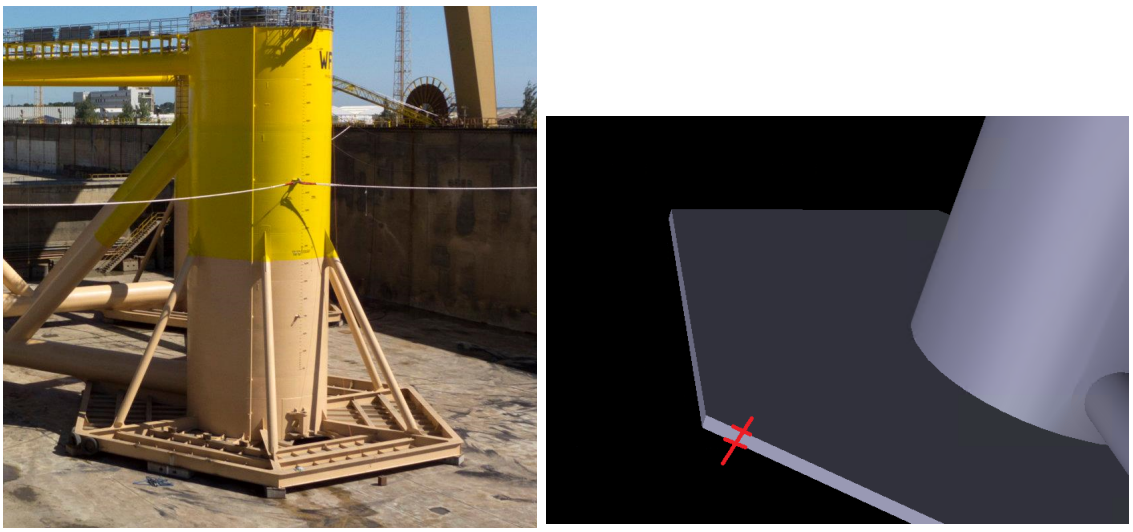

(a) Heave plates by PrinciplePower (2015)

(b) Heave plate thickness defined by the author

Figure 6.6: Illustrations of the heave plates on the WindFloat semi-submersible FWT

It was finally decided to use a heave plate thickness of 0.4 m, as defined in figure 6.6b. The relevant specifications of the modelled heave plates are given in table 6.3. Based on the calculated aspect ratio t_p/D_p, the added mass coefficient can be expected to have a value of 0.35-0.4, while the damping ratio may be expected to have a value of 0.5-0.6. The values given the aspect ratio is defined through figure 2.5.

Table 6.3: Specifications of the modelled heave plates

t_p [m]	D_p [m] (equivalent)	D_c [m]	t_p/D_p [-]	D_p/D_c [-]
0.4	27.3	10	0.0146	2.73

Simulations in HydroD were conducted with a plate thickness of both 0.05 m and 0.4 m for comparison. Figure 6.7 presents the pitch RAO for the semi-submersible with thickness of 0.05 m (black line), 0.4 m (blue line) and the model of Kvittem (2014) (red line). A difference between the thin plate and the model of Kvittem (2014), versus the model with the thicker heave plate is visible. It is thus assumed that Kvittem (2014) utilised a thin heave plate of 0.05 m. Numerical issues were discovered when calculating the second-order forces on the semi-submersible FWT, such as mean wave drift loads and quadratic transfer functions. In figure 6.8, the mean drift force in surge, computed with both conservation of fluid momentum and pressure integration for the two different thicknesses, are presented. A discrepancy between the two computation

methods is visible for the thin plate, while the mean drift forces correspond well for the thicker plate. Due to this fact, it was preferable to continue with the thick plate of 0.4 m. In addition, it is reasonable to assume that a thinner plain plate would give structural load issues, as the real full-scale plates are reinforced with stiffeners. Due to time efforts, analysis of the structural local loads on the conjunction between the heave plate and the column, was not performed, however it is strongly suggested as future work.

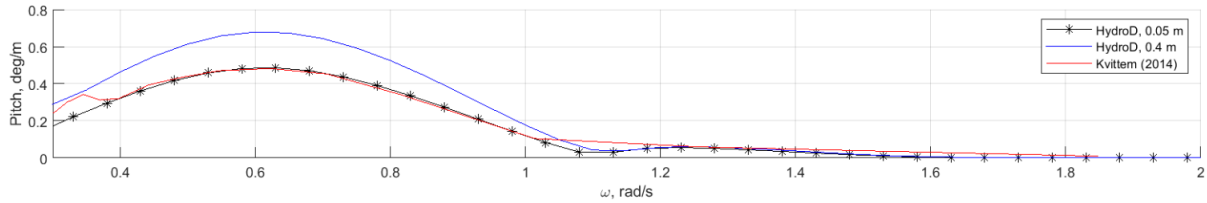

Figure 6.7: Pitch RAO for two heave plate thicknesses and the model of Kvittem (2014)

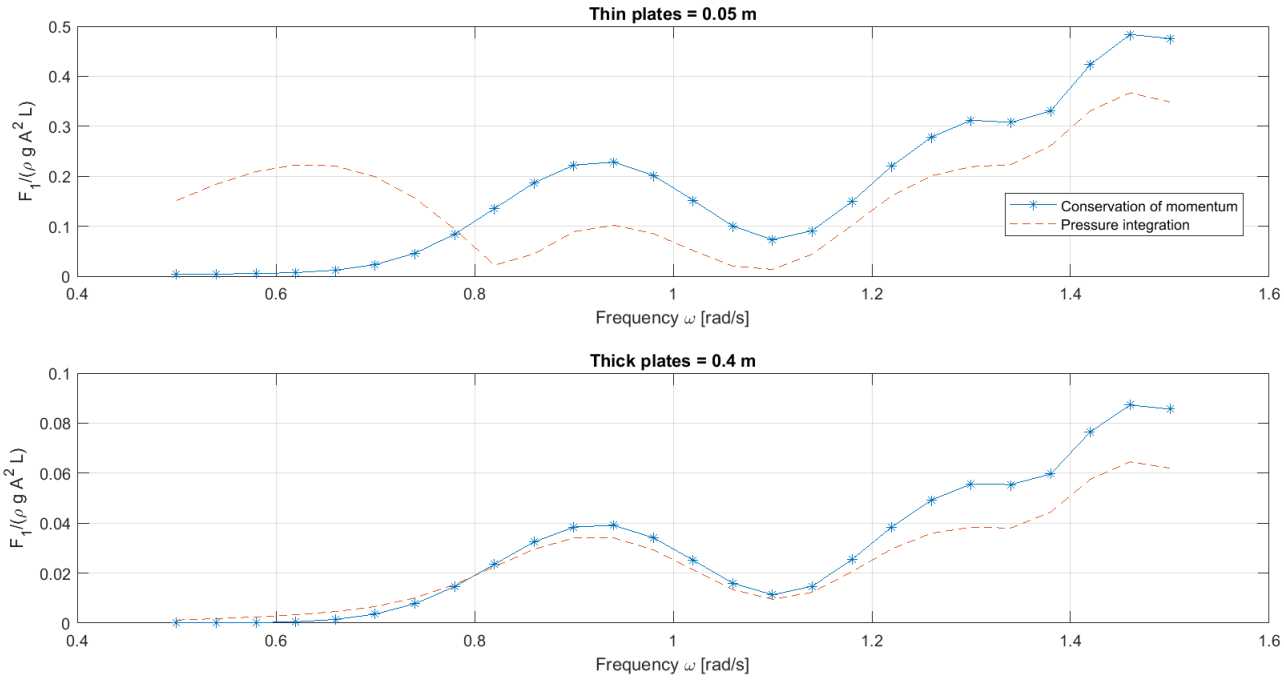

Figure 6.8: Mean drift force in surge for the WindFloat for two heave plate thicknesses

6.5.2 Selection of Viscous Coefficients for Heave Plates

As previously explained, the viscous-flow effects on the plates should be accounted for. The quadratic drag is already accounted for in SIMA, but the viscous added mass is not. The added mass and damping is strongly dependent on the KC-number, equation (6.1), where A is the plate oscillation amplitude and D_p is the plate diameter. The KC-number is thus a function of the flow velocity at the structure component and will differ with each wave in an irregular sea state.

$$KC = \frac{2\pi A}{D_p} \tag{6.1}$$

The variability in the KC-number provide a challenge for time-domain analysis, since it is not possible to define those coefficients as changeable variables in SIMA. The quadratic term in the Morison equation will therefore become underestimated in small waves, and overestimated in large waves. Concerning added mass, the case is opposite. It was therefore decided to use a statistical approach to obtain a good approximation for the KC-numbers. DNV GL's recommended practice for modelling and analysis of marine operations defines the KC-number for irregular sea states as in equation (6.2) (DNVGL 2017). Here, σ_v is the standard deviation of the relative velocity at the plate, T_z is the zero up-crossing period and D_p the plate diameter. σ_v is found by taking the standard deviation of the difference between the vertical velocity of the FWT and the vertical wave particle velocity at z = -16.8 m. This depth corresponds to the mid-point of the heave plate with a thickness of 0.4 m.

$$KC = \frac{\sqrt{2}\sigma_v T_z}{D_p} \tag{6.2}$$

In order to establish the viscous added mass and damping contribution, previous research has been utilised, and a summary was presented in section 2.4. The previous studies present the added mass A'_{33} and damping B'_{33} in their non-dimensionalized forms, equation (6.3) and (6.4), respectively. A^{th}_{33} is the theoretical added mass and ω is the oscillation frequency.

$$A'_{33} = \frac{A_{33}}{A^{th}_{33}} \tag{6.3}$$

$$B'_{33} = \frac{B_{33}}{\omega A^{th}_{33}} \tag{6.4}$$

The corrected heave added mass for the heave plates, which was implemented into SIMA for one environmental load case, was established according to the steps below.

- A model with and without heave plates was modelled in GeniE, and subsequently analysed with potential frequency-domain theory in HydroD.
- The difference in heave added mass for the two numerical models was established through post-processing in Matlab: A^{plate}_{33} and $A^{noplate}_{33}$. The values at the approximate heave natural period of 19.9 s were used in order to reflect the resonance conditions.
- The estimate of the added mass for an individual plate was thus found by dividing the difference by three. The result is defined as the potential heave added mass: $A^{pot}_{33} = (A^{plate}_{33} - A^{noplate}_{33})/3$
- According to the results of Lopez-Pavon and Souto-Iglesias (2015) (figure 2.6), the potential theory values for heave added mass overestimates the theoretical values. In order to account for this, the theoretical added mass is thus scaled down: $A^{th}_{33} = A^{pot}_{33}/1.04$

- The change of rate in heave added mass A'_{33} is taken from figure 2.8a, as a function of the KC-number.
- Because the potential-flow added mass A_{33}^{pot} is already included in the frequency-domain hydrodynamic analysis, the added mass can be considered a correction as in equation (6.5), which is implemented into SIMA.

$$A_{33}^{corr} = A_{33}^{th} \cdot A'_{33} - A_{33}^{pot} \tag{6.5}$$

Once the theoretical heave added mass A_{33}^{th} is established and B'_{33} is found by use of figure 2.8b, the linearized damping B_{33} can be found through equation (6.4). The drag coefficient due to the heave plate can then be found through equation (6.6), which in turn can be implemented as a quadratic drag coefficient in SIMA.

$$B_{33} = \frac{1}{3}\rho f D_p^3 \cdot KC \cdot C_D \tag{6.6}$$

Iterative Strategy
To define the viscous forces for the selected environmental load case, an iterative strategy was established. The KC-number, corrected added mass and drag coefficient for each slender element were found through the following steps.

1. Assumed values for added mass and drag were implemented into SIMA.
2. A time-domain analysis with environmental conditions according to table 5.1 was carried out for a one-hour simulation of the semi-submersible FWT WindFloat.
3. The standard deviation of the relative particle velocity at the plate σ_v and the zero up-crossing period T_z were found through post-processing in Matlab. The KC-number was calculated according to equation (6.2).
4. New corrected added mass and drag coefficient dependent on the KC-number were calculated in Matlab through the procedure explained above (equation (6.5) and (6.6)). The new values of added mass and quadratic drag were implemented in SIMA, and a new time-domain analysis were performed.
5. The first four steps were repeated until the iteration produced a converged KC-number with a sensitivity of 0.001. The process was then aborted, and the finalised values for KC, added mass and drag coefficient were imported into SIMA for a final simulation.

Chapter 7

Verification of Models

7.1 Hydrodynamic Analysis in HydroD

7.1.1 Mean Drift Forces

The mean drift forces were used to verify the mesh of the structures, by computation with both pressure integration and conservation of fluid momentum. As seen in figure 7.1, the two methods produce approximately the same mean drift force in surge for the mesh of both the spar and semi-submersible platform. For heave and pitch, the mean drift force is approximately zero for both structures, and the plots are therefore not presented here.

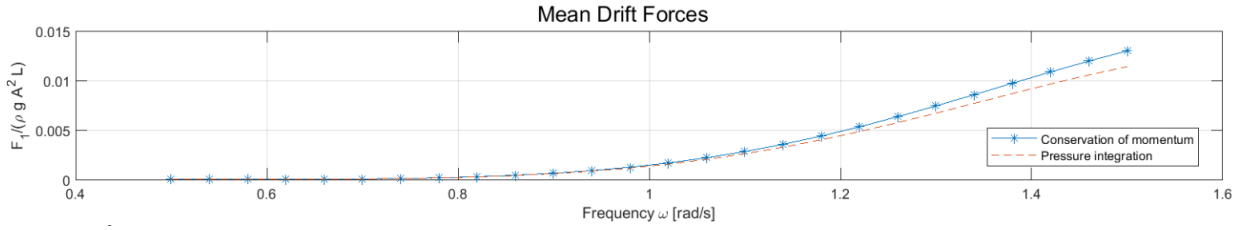

(a) OC3-Hywind

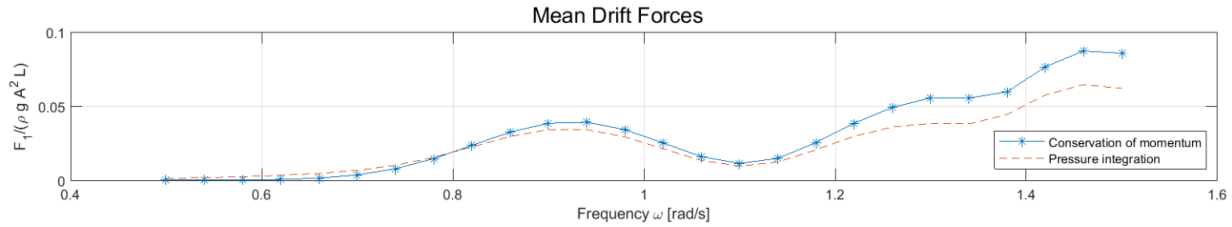

(b) WindFloat

Figure 7.1: Mean drift forces in surge

7.1.2 Response Amplitude Operator

The response amplitude operators (RAOs) of the models analysed in HydroD were compared to the RAOs of models provided by co-supervisor Erin Bachynski, analysed in SIMA by a regular wave analysis. The RAO is the transfer function of the body motion amplitude (Faltinsen 1993), and presents body response amplitude per incident wave-amplitude. By comparing the response from a simple model in HydroD to the predicted responses by a more complicated non-linear time-domain tool, the response of the platforms can be verified. The RAOs for the spar and semi-submersible platform are presented in figure 7.2 and 7.3, respectively. The spar platform shows good agreement between the analyses from HydroD and SIMA. The semi-submersible, however, has a discrepancy in pitch, but shows quite good agreement for surge and heave. The inconsistency between 0.4 rad/s and 0.9 rad/s for the pitch RAO, is assumed to appear due to a thicker heave plate in the HydroD-model than in the provided SIMA-model. See section 6.5 for discussion regarding the heave plate thickness.

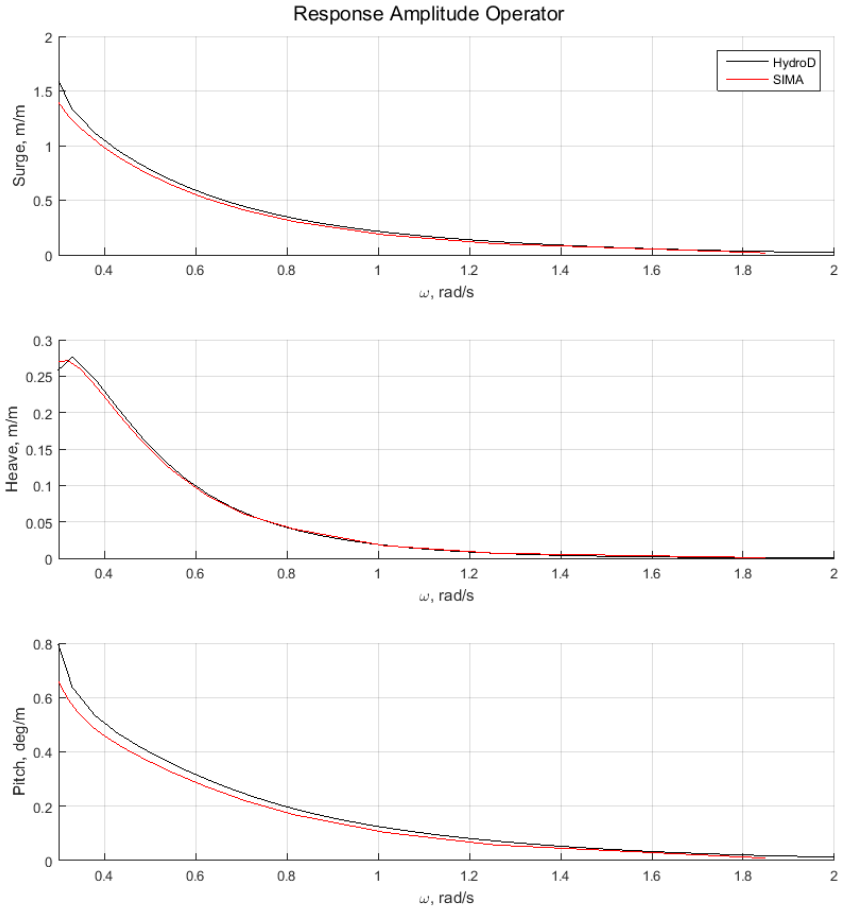

Figure 7.2: Response amplitude operator OC3-Hywind

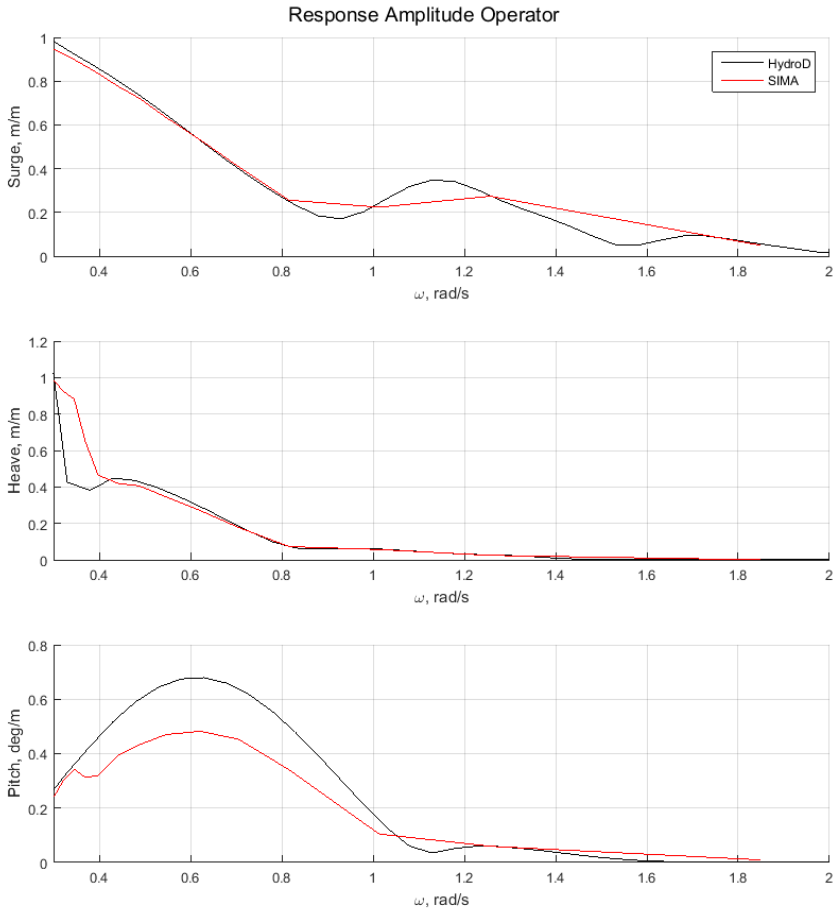

Figure 7.3: Response amplitude operator WindFloat

7.1.3 Eigenperiods

HydroD calculates the natural periods for the FWT structures without the influence of the mooring system. However, additional mooring line stiffness is applied for all six DoFs for OC3-Hywind and for surge for WindFloat. The obtained natural periods and the difference (%) in regard to the values presented in table 4.3 and 4.6, are presented in table 7.1. Regarding the semi-submersible platform, the hydrostatic restoring coefficients for sway and yaw are zero. Thus, only the natural periods for surge, heave, roll and pitch are presented for WindFloat.

The natural periods for the models of OC3-Hywind and WindFloat, show quite good agreement with the reference values in table 4.3 and 4.6, respectively.

Table 7.1: Natural periods from HydroD

DoF	$T_{n,OC3}$ [s]	Difference [%]	$T_{n,WF}$ [s]	Difference [%]
Surge	124.3	0	105.7	- 1.2
Sway	124.3	0	-	-
Heave	30.9	+0.3	20.2	+1.5
Roll	29.1	- 0.3	35.8	+0.6
Pitch	29.1	- 0.3	37.0	- 1.1
Yaw	8.4	+1.2	-	-

7.1.4 Quadratic Transfer Functions

In figure 7.4, the difference-frequency excitation forces in surge and heave and moment in pitch, calculated with full QTF and Newman's approximation, are presented for both OC3-Hywind and WindFloat. It is observed that Newman's approximation and the full-QTF analyses give similar results for the surge difference-frequency forces. However, for the heave force and pitch moment, Newman's approximation underestimates with respect to the full QTF force. This corresponds to the assumption that Newman's approximation generally underestimates the force when the natural periods are less than 100 s, which is the case in heave and pitch for both FWTs.

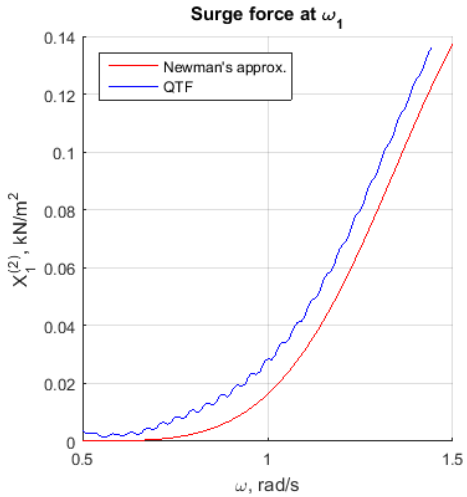

(a) OC3-Hywind - Surge diff.-frequency

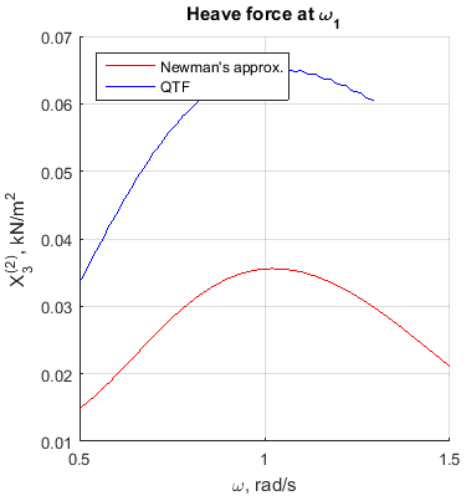

(b) OC3-Hywind - Heave diff.-frequency

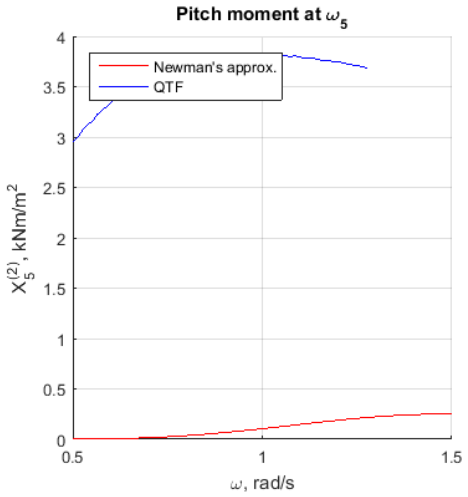

(c) OC3-Hywind - Pitch diff.-frequency

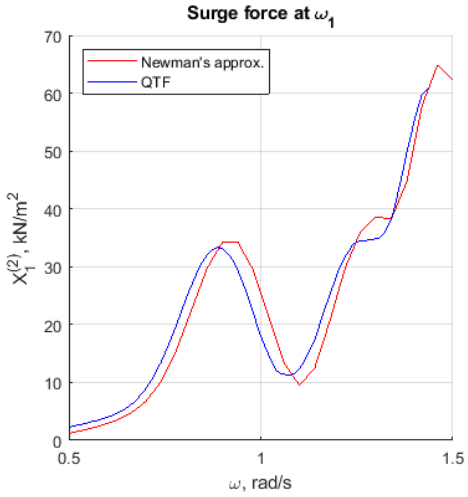

(d) WindFloat - Surge diff.-frequency

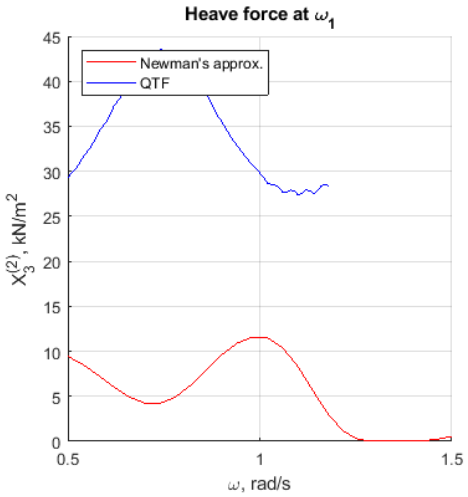

(e) WindFloat - Heave diff.-frequency

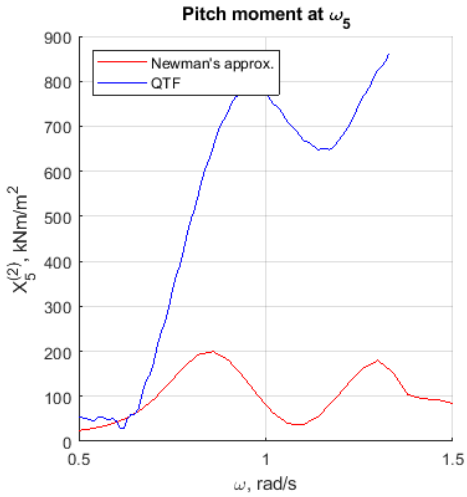

(f) WindFloat - Pitch diff.-frequency

Figure 7.4: Difference-frequency excitation force for both platforms

7.2 Free Decay Tests

In order to document the behaviour of the FWTs, the natural periods of the two systems were determined through free decay tests of all six degrees of freedom. The tests thus serve as a verification of the models and hydrodynamic data from GeniE and HydroD. The tests were carried out in SIMA by applying a ramp force or moment after 50 s, followed by a constant force or moment which is released after a specified time. The turbine is in parked condition, i.e. the rotor blades are feathered and stand-still, to reduce the degrees of freedom for the system. The wind speed is $U_w = 0.01$ m/s, and the wave condition is represented by $H_s = 0.001$ m and $T_p = 20$ s. The obtained natural periods and the difference (%) in regard to the values in table 4.3 and 4.6, are presented in table 7.2. The free decay motions are given in appendix B for both structures and all degrees of freedom.

Table 7.2: Natural periods from free decay tests

DoF	$T_{n,OC3}$ [s]	Difference [%]	$T_{n,WF}$ [s]	Difference [%]
Surge	125.2	+0.7	105.2	- 1.7
Sway	125.3	+0.7	125.0	+0.2
Heave	29.8	- 3.2	20.0	+0.5
Roll	27.6	- 5.5	36.4	+2.2
Pitch	27.6	- 5.5	37.1	- 0.8
Yaw	8.5	+2.4	63.0	- 7.4

The modelled spar platform analysed in SIMA give satisfying corresponding natural periods to the reference values from Jonkman (2010). The eigenperiods in roll and pitch give the largest discrepancy with 5.5 % difference to the reference value of 29.2 s. For the modelled semi-submersible platform, the eigenperiods for all DoFs except yaw motion, produce corresponding results to the reference values from Kvittem (2014). In figure B.4c in the appendix, it is also seen that the first wave top for the yaw free decay test, is smaller than the second one. This will cause errors and discrepancies for the yaw eigenperiod, which is defined at 68.5 s by Kvittem (2014). A possible explanation for this discrepancy is the coupling between the yaw and sway motion, which is quite extensive. In appendix B.3, the coupling effect between the sway and yaw motion during the yaw free decay test is quite distinct. In addition, the coupling of all motions during the sway free decay test is presented, and the coupling with the yaw motion is quite distinguishable.

7.3 Wind Turbine Performance

To validate the performance of the 5 MW wind turbine and the controller, constant uniform wind tests were performed in SIMA. The tests were carried out by performing a time-domain analysis of the FWT system exposed to constant uniform wind speeds from 4 m/s to 24 m/s, including the rated wind speed. The wave condition is calm with zero current speed and $H_s = 0.001m$ and $T_p = 20s$. The parameters to be validated against the NREL performance curves are the mean of the properties listed below. The statistical values are plotted for the time period after the system has reached a steady-state condition in figure 7.5 with satisfying results.

- Rotor speed [rpm]
- Blade pitch angle [deg]
- Generator torque [kNm]
- Generator power [kW]
- Rotor thrust [kN]
- Rotor torque [kNm]

The performance of the NREL 5 MW wind turbine was checked against the performance curves by Jonkman et al. (2009), given in appendix A.4. From a graphical assessment, the obtained results correspond well with the reference curves and the tabulated values

in table 4.7. Above rated wind speed, the blade-pitch controller reduces the rotor thrust, while the generator power and torque are kept constant by regulating to a fixed rotor speed and variable blade-pitch angle. This is to maintain the optimal conversion efficiency of the wind energy power.

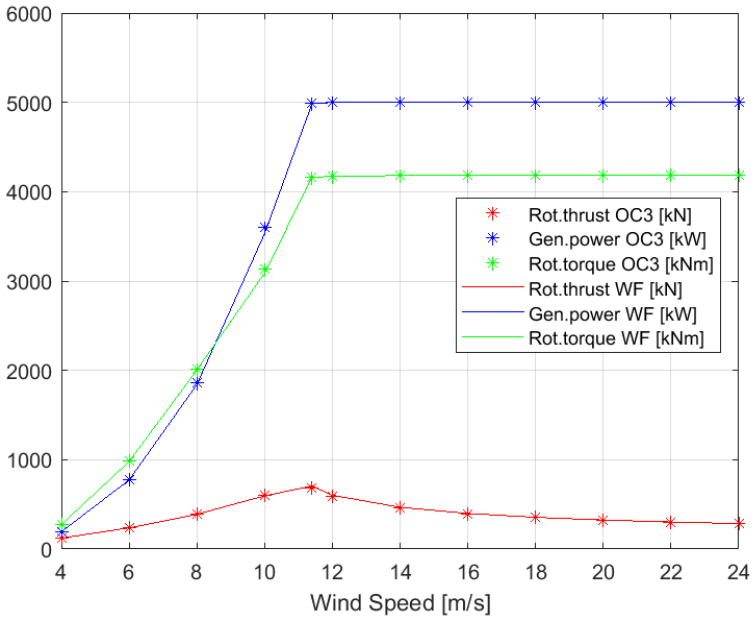

(a) Rotor thrust, generator power and rotor torque

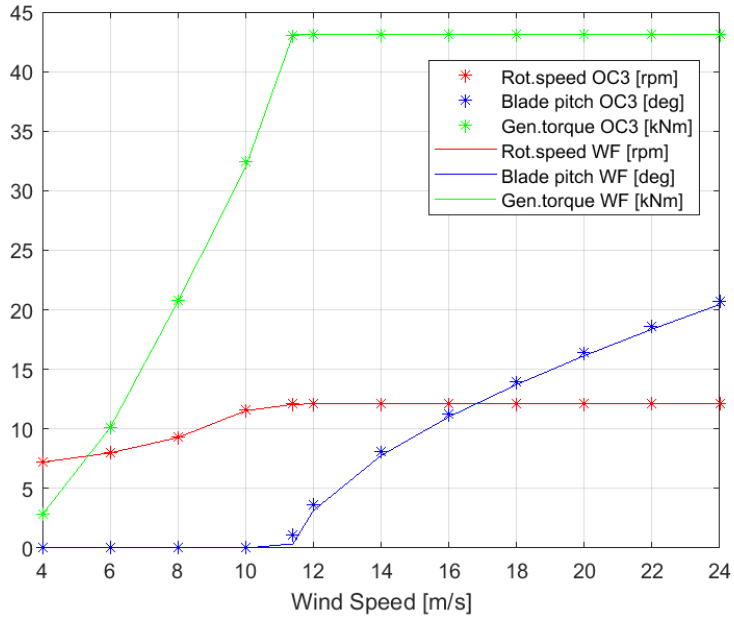

(b) Rotor speed, blade pitch angle and generator torque

Figure 7.5: NREL 5 MW turbine performance curves

Chapter 8

Study of FWTs in Extreme Conditions

The investigation of the two floating wind turbines in extreme conditions will next be presented. Each FWT is analysed in SIMA under the environmental load cases presented in tab. 5.1. Each analysis is performed in three ways:

- First-order wave force analysis
- Second-order wave drift force analysis with Newman's approximation
- Second-order difference-frequency wave force analysis with full QTF

All simulations are run for 3600 second, i.e. one-hour simulations. The first 1000 seconds of the simulation time are excluded from the time-series, in order to allow for the start-up time of the turbine. In addition to the analyses listed above, selected cases have been chosen to be investigated in a second-order analysis with wave drift damping included, by utilising Newman's approximation (section 8.5). Further, one selected case for the semi-submersible WindFloat has been chosen, in order to investigate the correction of viscous forces due to the heave plates, presented in section 8.6.

8.1 Platform Motion Response

In order to analyse the effect of the different environmental load cases on the two FWTs, it was decided to present statistical values of the platform responses. Therefore, the standard deviation, maximum and minimum of the platform response in surge, heave and pitch are presented for the two FWTs in table 8.1. In addition, time-series of the surge motion for each load case are presented for both platforms in figure 8.1. The values are extracted from the simulation in SIMA which includes the second-order difference-frequency wave force transfer function. However, the difference to the first-order and second-order Newman analysis is in the order of 0.01.

Some trends are apparent in the response of the FWTs in table 8.1. Focusing on the differences between the two platforms, the spar OC3-Hywind has in general larger standard deviation in surge motion, than the semi-submersible WindFloat. This is true for the expected operational condition and the four extreme conditions. This is also true for the pitch motion in the extreme conditions (LC3-LC6). With regard to the

two cases with 50-year conditions, the surge response is approximately 3.8 % larger for OC3-Hywind, while the pitch response is approximately 25 % larger. For the 100-year conditions, the corresponding differences are 8 % and 29 %, respectively. In heave motion, the opposite relation is observed, as WindFloat has larger response variation for the maximum operational and extreme conditions. For load case 3 and 4, the heave response is 54.2% higher for WindFloat, than for OC3-Hywind. The difference in heave response is greatest for the misaligned 100-year wind and waves (LC6), with 56.9 % larger heave response for WindFloat.

WindFloat is subject to greater maximum offset in surge and heave, than OC3-Hywind. This is also observed in figure 8.1 for surge. The maximum surge response of the semi-submersible platform is approximately 40 % higher than for the spar. Regarding the pitch response in the extreme conditions, the results are inconsistent. With a 50-year return period, the maximum pitch response is greatest for WindFloat, while maximum pitch response is largest for OC3-Hywind with a 100-year return period.

The trend that the semi-submersible WindFloat has larger motions, is supported by the fact that spar platforms are designed for small and slow motions, especially in heave due to the large draft. Semi-submersible platforms have a smaller draft and are thus characterised by larger motions. This is true in these cases, as observed, even though WindFloat has heave plates attached to the bottom of the columns which should reduce heave and pitch platform motion. It is assumed that the heave motions for WindFloat would be more extensive without the heave plates, however, this effect is not investigated in this thesis. Karmakar et al. (2016) found that the RAOs in surge, heave and pitch were higher for a semi-submersible FWT than for a spar platform, which indeed supports the results presented here.

As expected, the platform motion responses increase with increasing environmental conditions. A 100-year return period of wind and waves, produce larger responses than a 50-year return period. This is seen for both OC3-Hywind and WindFloat for all DoFs. It is observed that the surge and pitch response are lower in the maximum operational case, than in the expected operational case, where the latter is characterised by lower wind speed and waves.

In LC4 and LC6, the wind is misaligned with the waves with 90°. The response deviation of the FWTs is somewhat influenced by the misalignment of wind and waves. However, the differences to the aligned cases are minimal and in the order of 0.01 regarding the standard deviation. The aligned conditions produce larger responses, which is illustrated in figure 8.1. The differences between the misaligned and aligned cases are more considerable for the maximum values, where the aligned conditions produce the largest maximum response. This is consistent with the fact that the wind speed is significantly less for the misaligned conditions (table 5.1).

Table 8.1: Standard deviation, maximum and minimum of platform motion

Standard Deviation of Platform Motion

	Surge [m]		Heave [m]		Pitch [deg]	
	OC3	WF	OC3	WF	OC3	WF
LC1 - exp. op.	3.60	2.58	0.18	0.12	0.81	1.86
LC2 - max. op.	1.27	1.67	0.31	0.49	0.70	1.10
LC3 - 50-year, aligned	3.81	3.67	0.87	1.90	1.94	1.47
LC4 - 50-year, misal.	3.85	3.70	0.87	1.90	1.98	1.46
LC5 - 100-year, aligned	4.12	3.79	1.01	2.11	2.11	1.52
LC6 - 100-year, misal.	4.15	3.84	0.91	2.11	2.17	1.50

Maximum of Platform Motion

	Surge [m]		Heave [m]		Pitch [deg]	
	OC3	WF	OC3	WF	OC3	WF
LC1 - exp. op.	28.02	23.85	0.32	0.42	6.13	5.21
LC2 - max. op.	13.90	18.04	1.21	2.16	5.19	5.99
LC3 - 50-year, aligned	22.32	37.81	4.57	6.26	6.59	6.71
LC4 - 50-year, misal.	21.43	35.82	4.13	6.22	6.50	6.68
LC5 - 100-year, aligned	24.96	40.28	5.59	6.86	7.31	6.76
LC6 - 100-year, misal.	23.03	38.05	4.30	6.82	7.09	6.93

Minimum of Platform Motion

	Surge [m]		Heave [m]		Pitch [deg]	
	OC3	WF	OC3	WF	OC3	WF
LC1 - exp. op.	5.68	7.55	-0.89	-0.54	1.16	-6.42
LC2 - max. op.	5.44	7.81	-0.81	-1.67	-0.65	-3.08
LC3 - 50-year aligned	-0.92	14.79	-2.03	-5.84	-5.28	-4.49
LC4 - 50-year misaligned	-2.78	12.27	-2.52	-5.90	-5.70	-4.50
LC5 - 100-year aligned	-0.58	16.53	-2.67	-6.40	-5.67	-4.85
LC6 - 100-year misaligned	-4.09	14.44	-2.52	-6.45	-6.30	-4.55

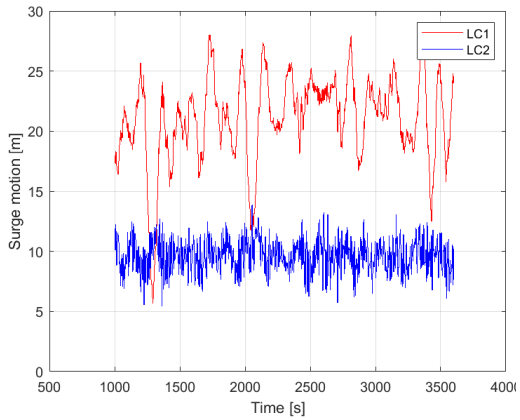

(a) OC3-Hywind - LC1, LC2

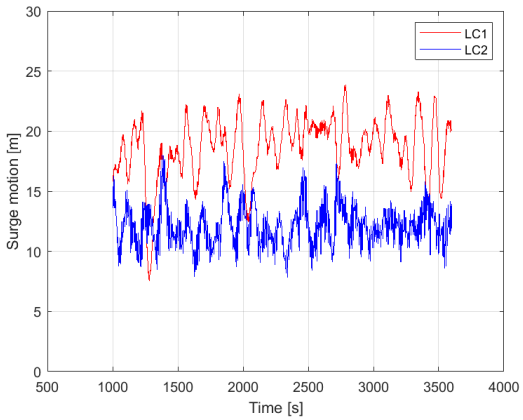

(b) WindFloat - LC1, LC2

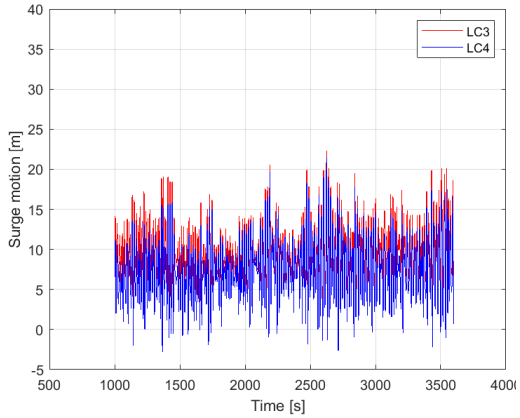

(c) OC3-Hywind - LC3, LC4

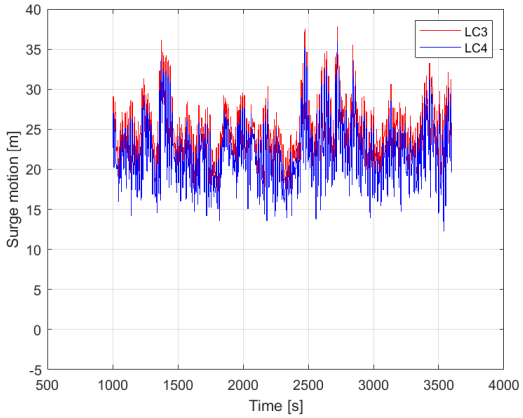

(d) WindFloat - LC3, LC4

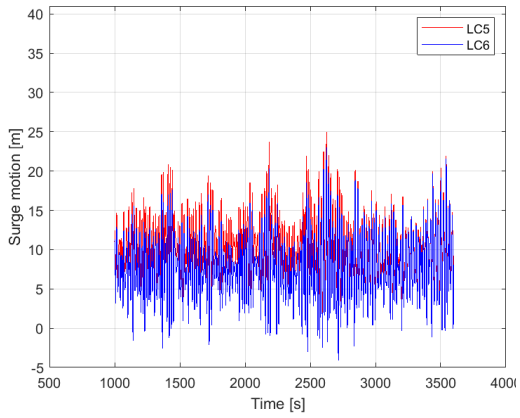

(e) OC3-Hywind - LC5, LC6

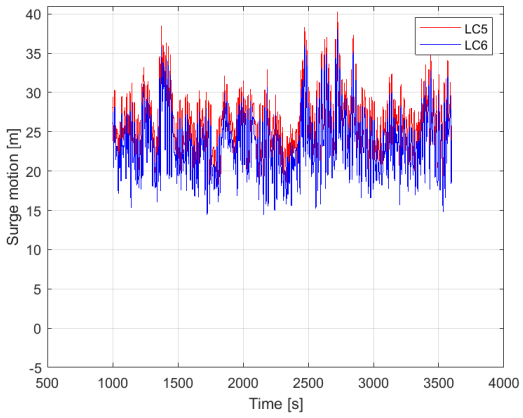

(f) WindFloat - LC5, LC6

Figure 8.1: Time series of the platform surge motion of both platforms

8.2 Loads on the FWTs

In order to identify the effect of the extreme conditions on the two structures, structural loads in the tower and the aerodynamic thrust force on the wind turbine are presented next. The axial force and bending moment in y-direction are taken at the tower base and tower top. In addition, the aerodynamic thrust force in x-direction at the shaft is given. The loads are given as standard deviation, for each load case and type of analysis, in table 8.2-8.4. In figure 8.2, the time-series of the axial force, bending moment and thrust are given for both structures during the two extreme cases with aligned conditions. A short time period of the full simulation time is selected due to simplicity of the illustration and observation. Figure 8.3 presents the surge, heave and pitch force by first-order analysis, second-order QTF and second-order wave drift analysis with Newman's approximation in LC3. Lastly, figure 8.4 presents the second-order QTF surge forces of OC3-Hywind and WindFloat for load cases 1,3 and 5.

8.2.1 Axial Force on Tower Base and Top

Focusing on the axial force in the tower base and tower top in table 8.2, one can observe that the axial force is significantly higher in the tower for the semi-submersible WindFloat than for OC3-Hywind. This is true for both the base and top of the towers, each load case and each type of analysis. The axial force in the tower base of the WindFloat is approximately 50 % larger in the two operational cases and the two cases with aligned conditions. When the wind and waves are misaligned, the difference is about 62%. This is valid for first-order, second-order wave drift and second-order full-QTF forces. However, at the tower top the axial force of the OC3-Hywind is only 30-36 % of the force of the WindFloat, regarding the two operational and two aligned extreme load cases.

One of the most noticeable aspects regarding the axial force in the tower, is that the force is approximately equal for first-order, second-order wave drift and second-order QTF analysis for each structure. The wave drift and difference-frequency wave force transfer functions only apply to the waves, which in most cases do not interact with the tower significantly. Due to this, the similarity between the three cases is plausible. It is also observed that the axial force is stronger at the tower base than the tower top, which implies that the forces from the waves affect the structural loads at the base in a more extensive degree.

The misalignment of the wind to the waves during extreme conditions poses an effect to the axial forces in the towers. On the spar platform OC3-Hywind, the axial force due to misaligned wind is much smaller than in the case of aligned wind. With a 100-year return period and aligned conditions, the axial force at the tower base is approximately 27% larger than during misaligned conditions. At the tower top, the difference is 45 %. With 50-year conditions, the corresponding values are 17 % and 37 %, respectively. The misaligned wind speed is closer to the maximum operational wind speed of 25 m/s, and thus, the those results correspond well. Regarding WindFloat, the situation is opposite for the extreme cases, as the axial force due to misaligned wind is larger than in the case of aligned wind, however, only by 1-2 %.

As expected the axial force in the tower increases with increasing wind speed, i.e. increasing return period of the environmental conditions. Regarding OC3-Hywind, the axial force under 100-year conditions are 13-14% larger, while it is 5-7 % on the WindFloat-tower. This leads to the implication that the tower of WindFloat is subject to a larger variation of and stronger axial force, but is not as affected by the increasing wind speed as the OC3-Hywind-tower. This is illustrated in figure 8.2a and 8.2b, where the time series of the axial force at the tower base of both structures are presented for LC3 and LC5.

Table 8.2: Standard deviation of FWT axial force at tower base and top

Axial force tower base [kN]

	First-order wave		Second-order wave drift		Second-order QTF	
	OC3	WF	OC3	WF	OC3	WF
LC1 - exp. op.	20.62	42.11	20.60	42.07	20.62	42.10
LC2 - max. op.	60.39	114.83	60.39	114.88	60.45	114.89
LC3 - 50-year, aligned	91.17	190.17	91.31	191.01	90.76	190.62
LC4 - 50-year, misal.	75.56	194.93	75.82	195.69	75.86	195.49
LC5 - 100-year, alinged	104.87	200.28	105.54	201.51	105.50	203.57
LC6 - 100-year, misal.	76.45	203.66	76.58	204.88	77.06	207.29

Axial force tower top [kN]

	First-order wave		Second-order wave drift		Second-order QTF	
	OC3	WF	OC3	WF	OC3	WF
LC1 - exp. op.	18.14	28.74	18.13	28.70	18.14	28.72
LC2 - max. op.	54.47	81.02	54.46	81.00	54.47	81.05
LC3 - 50-year, aligned	77.17	117.80	77.19	118.45	76.65	118.34
LC4 - 50-year, misal.	48.32	120.48	48.49	120.94	48.48	120.94
LC5 - 100-year, aligned	89.06	125.44	89.34	126.43	89.36	127.89
LC6 - 100-year, misal.	48.81	125.91	48.83	126.71	49.03	128.33

8.2.2 Bending Moment in Y-Direction at Tower Base and Top

In table 8.3, the standard deviation of the bending moments in y-direction of the tower base and tower top are presented. The bending moment in y-direction is chosen because it is larger than the bending moment in z-direction, i.e. it affects the structural integrity of the tower to a larger extent. The mean and standard deviation of the bending moment in z-direction is in the order of 10^3, while in y-direction the bending moment of the tower is in the order of 10^4.

During the expected operational load case (LC1), where the wind speed is below rated wind speed, the bending moment in y is higher for the WindFloat tower base than for OC3-Hywind. However, during the other load cases, where the wind speed is higher than rated wind speed (LC2) and higher than the cut-out wind speed (LC3-LC6), the

bending moment is higher in the OC3-Hywind-tower. This is illustrated in figure 8.2c and 8.2d, where the time series of the bending moment in y-direction in the tower base are presented for both structures and load cases 3 and 5. The moment of OC3-Hywind is visibly higher and with larger variation than WindFloat. this corresponds with the results presented from Karmakar et al. (2016). The bending moment during the extreme conditions, with both aligned and misaligned wind, is approximately 67 % higher in the OC3-Hywind-tower.

The misalignment of the wind has an inconsistent effect on the two structures. At the tower base of the OC3-Hywind-tower, the misaligned wind produces a higher bending moment, while at the WindFloat tower base, the misaligned wind produces a smaller moment. This is only seen at the tower base, since at the tower top of both structures, the misaligned wind produces a smaller bending moment. As with the axial force, an increase of magnitude of conditions, increases the bending moment in y-direction in the tower. In addition, the effects of the different hydrodynamic analyses are small, although the bending moment increases with increasing environmental condition.

Table 8.3: Standard deviation of FWT bending moment in Y at tower base and top

Bending moment tower base [kNm]

	First-order wave		Second-order wave drift		Second-order QTF	
	OC3	WF	OC3	WF	OC3	WF
LC1 - exp. op.	19586	23235	19590	23271	19587	23300
LC2 - max. op.	32666	20268	32672	20229	32670	20191
LC3 - 50-year, aligned	54880	18668	54888	18774	54924	18957
LC4 - 50-year, misal.	55241	18384	55245	18524	55272	18663
LC5 - 100-year, aligned	57070	19010	57084	19163	57192	19458
LC6 - 100-year, misal.	57487	18603	57465	18770	57573	19068

Bending moment tower top [kNm]

	First-order wave		Second-order wave drift		Second-order QTF	
	OC3	WF	OC3	WF	OC3	WF
LC1 - exp. op.	1454.1	1553.8	1454.1	1553.7	1454.0	1553.0
LC2 - max. op.	2864.5	2781.1	2865.9	2772.5	2864.4	2781.7
LC3 - 50-year, aligned	1734.6	792.2	1737.2	796.6	1736.9	802.6
LC4 - 50-year, misal.	1311.5	569.0	1311.5	571.1	1311.8	574.1
LC5 - 100-year, aligned	1850.2	870.7	1845.6	880.2	1851.6	890.9
LC6 - 100-year, misal.	1360.7	574.1	1360.8	576.3	1362.7	583.6

8.2.3 Aerodynamic Thrust on the Turbine Shaft

The aerodynamic force in x-direction at the shaft of the turbine, i.e. the thrust force on the turbine, is presented for all load cases in table 8.4. The thrust force is a reaction force from the turbine on the wind, due to the load from the wind flow. The thrust on the turbine of the spar platform is in general slightly larger than on the turbine of the semi-submersible. Further, the thrust is significantly lower for the extreme cases than during the operational cases. This is explained by the parked turbine and fully feathered blades during the extreme load cases (LC3-LC6), i.e. the turbine is not producing power. The reason for pitching the rotor blades of the turbine is to reduce the thrust to protect the turbine during extreme weather conditions. When the blades are pitched, the angle of attack decreases, and consequently, the lift force on the air foils decreases. The thrust force is mainly produced from the lift force, which is explained in section 3.2. Thus, when the lift force decreases, the thrust force decreases.

It is also observed that the misalignment of the wind greatly influences the thrust force. The thrust force is comparably smaller during misaligned wind cases. This corresponds to the connection between the wind flow and the thrust force during those two cases. The wind flow is then directed in the positive y-direction, while the thrust force is taken in the positive x-direction. However, the aerodynamic force increases with increasing wind speed and wave height and period. Nevertheless, the differences between the two extreme cases with aligned conditions are quite small, as can be seen in figure 8.2e and 8.2f. The times series of the thrust force in x-direction at the turbine shaft are illustrated for both structures and load cases 3 and 5.

Table 8.4: Standard deviation of FWT aerodynamic thrust at shaft (x-direction)

Aerodynamic thrust at shaft [kN]

	First-order wave		Second-order wave drift		Second-order QTF	
	OC3	WF	OC3	WF	OC3	WF
LC1 - exp. op.	98.83	93.84	98.83	93.86	98.82	93.83
LC2 - max. op.	86.24	68.90	86.24	68.82	86.20	68.83
LC3 - 50-year, aligned	14.71	11.02	14.74	11.02	14.79	11.02
LC4 - 50-year, misal.	3.22	2.95	3.45	2.96	4.36	2.96
LC5 - 100-year, aligned	17.46	12.62	17.39	12.58	17.45	12.67
LC6 - 100-year, misal.	4.10	3.40	4.13	3.39	4.15	3.38

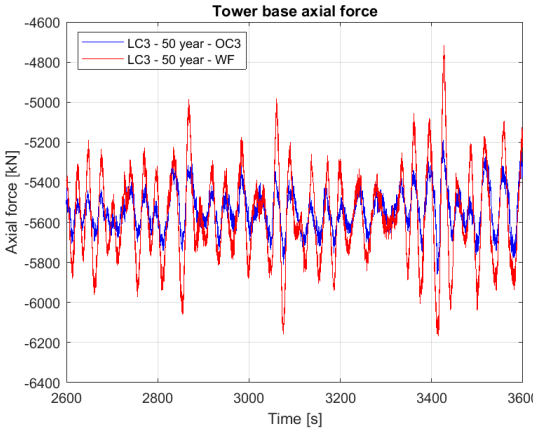

(a) Axial force tower base, LC3

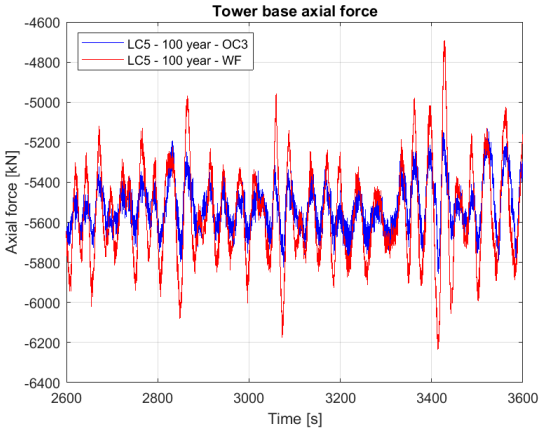

(b) Axial force tower base, LC5

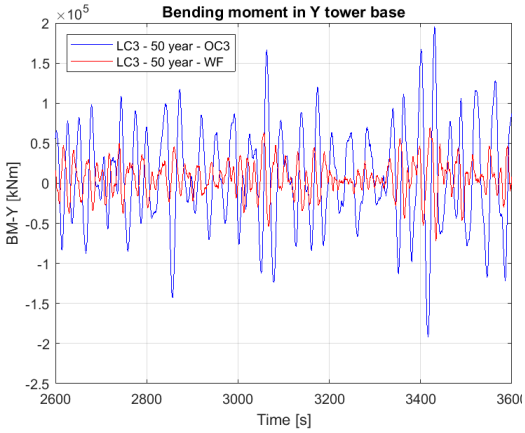

(c) Bending moment (y) tower base, LC3

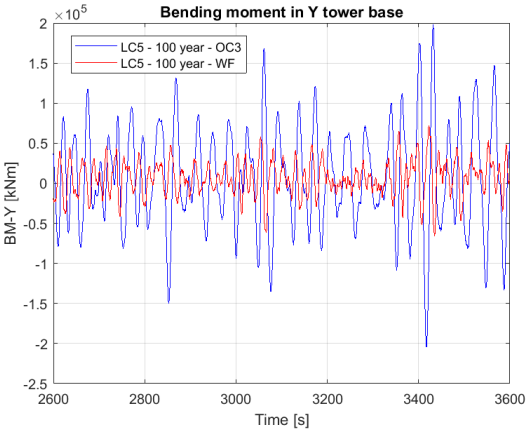

(d) Bending moment (y) tower base, LC5

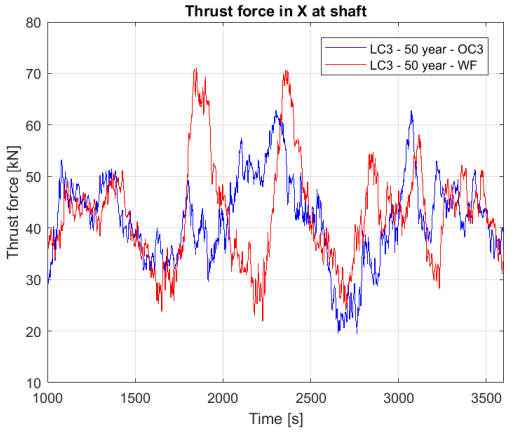

(e) Thrust force shaft, LC3

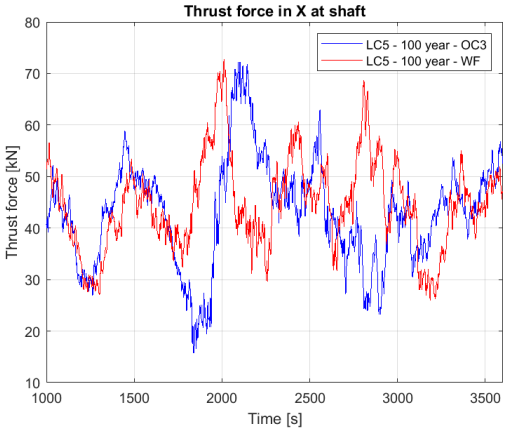

(f) Thrust force shaft, LC5

Figure 8.2: Axial force, bending moment in y-direction and thrust force for LC3 and LC5 - OC3 and WF

8.2.4 Hydrodynamic Loads on the FWTs

In addition to the structural and aerodynamic loads described above, the hydrodynamic loads on the floating platforms have been analysed and illustrated in figure 8.3 and 8.4.

In figure 8.3, the surge and heave forces on the OC3-Hywind and WindFloat are presented for load case 3 with 50-year return period conditions. The pitch forces are not presented here as they are fairly similar for both FWTs. The forces are computed by first-order wave force (red line), second-order wave drift force with Newman's approximation (green line) and second-order QTF force (blue line). The first-order wave forces are significantly larger than the two forces calculated with second-order theory. This corresponds to the literature studied in section 2.3, and the theory from Faltinsen (1993). Further, the second-order QTF wave force is in general larger than the second-order Newman's wave drift force to a small extent. WindFloat is subjected to a larger surge and heave force than OC3-Hywind. This is particularly noticeable for the heave force.

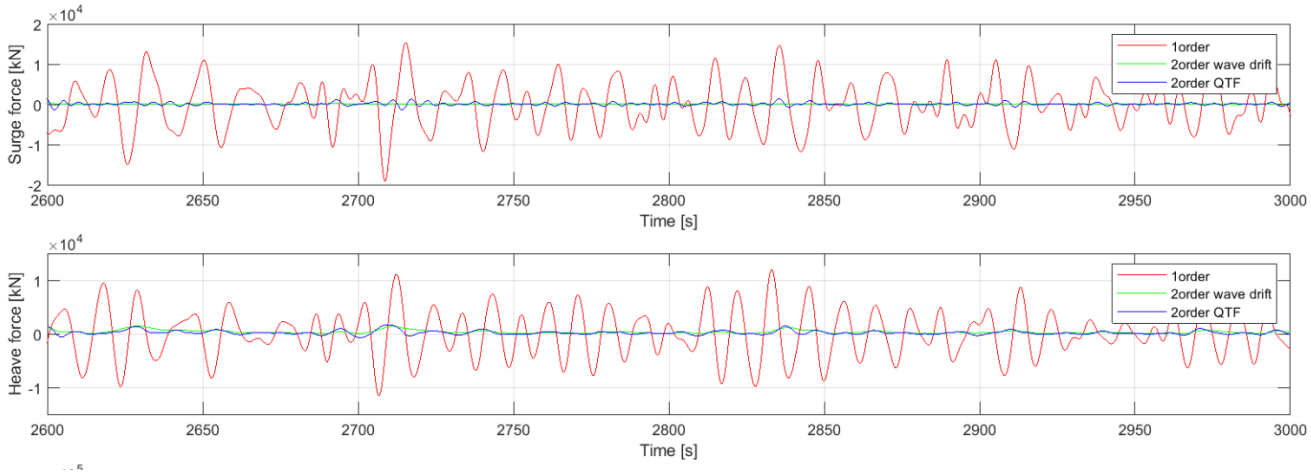

(a) OC3-Hywind

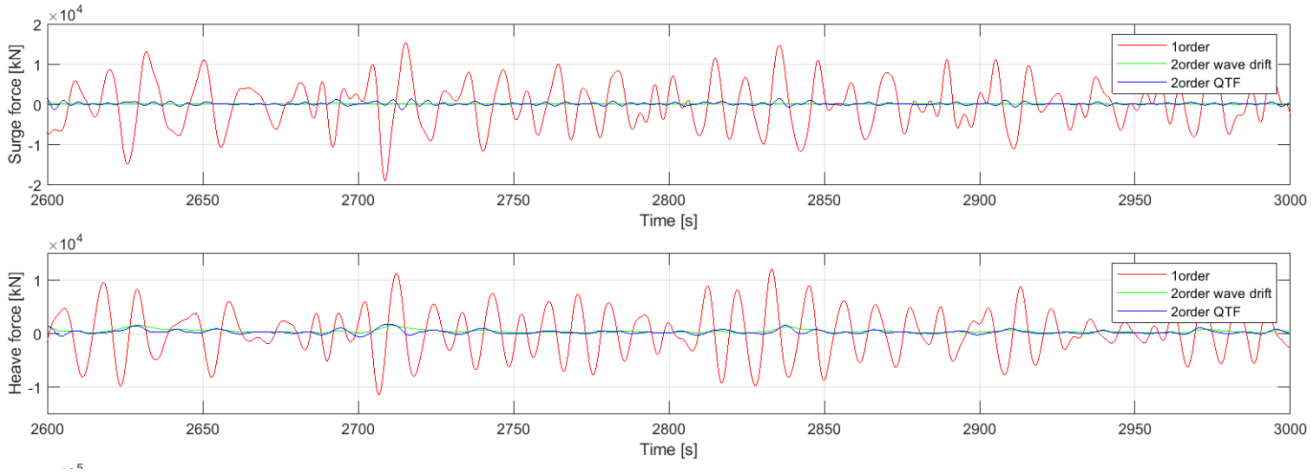

(b) WindFloat

Figure 8.3: Surge, heave and pitch force on OC3-Hywind and Windfloat for LC3 (50-year, aligned)

In figure 8.4, the time-series of the second-order QTF surge wave force are illustrated for both structures and the three load cases LC1, LC3 and LC5. The surge force is found for environmental conditions defined as expected operational (blue line), extreme 50-year return period with aligned wind (red line), and extreme 100-year return period with aligned wind (green line). A selected period of the full simulation time is presented to provide better visibility. The surge second-order QTF wave force significantly increases with increasing wind speed. The force produced during extreme cases are thus, as expected, significantly larger compared to operational environmental conditions. One can, in addition, observe that the forces from the two extreme load cases, to a great extent, are similar. Therefore, the increased wind and waves do not affect the second-order QTF wave forces remarkably.

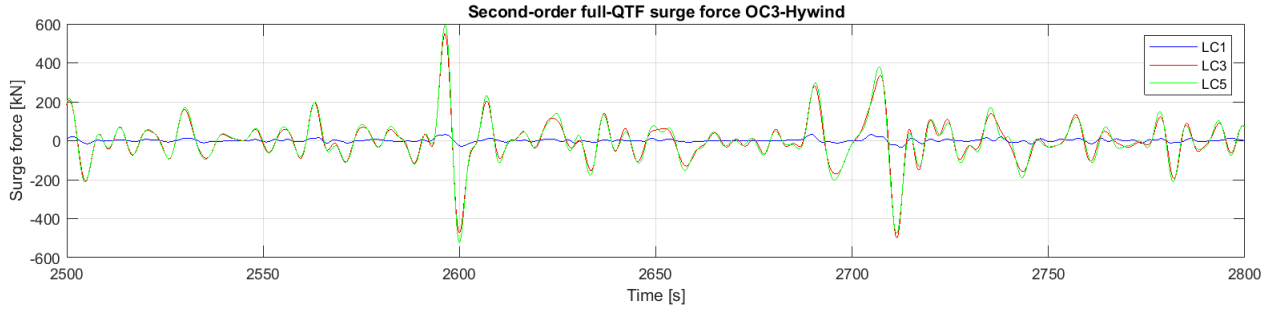

(a) OC3-Hywind

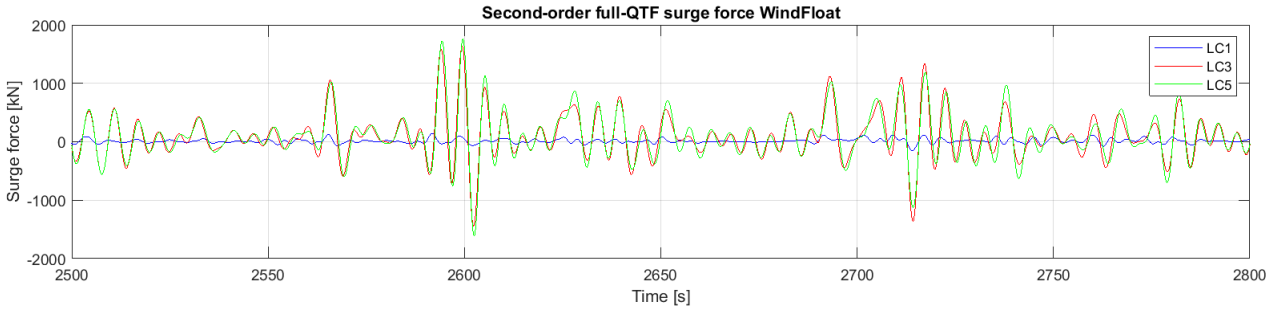

(b) WindFloat

Figure 8.4: Second-order full-QTF surge force: LC1, LC3, LC5

8.3 Mooring Line Tensions

The mooring line tensions at the fairleads (i.e. the connections at the platform), are presented next as the axial force at the fairlead connection of mooring line 2 and 3 of both structures. The tension is given for all load cases by first-order wave force and second-order QTF wave force in table 8.5. The mooring systems of the two paltforms, are somewhat different; OC3-Hywind has three catenary homogeneous mooring lines of wire rope, while WindFloat has four catenary mooring lines combined of chain and polyester rope. However, both structures have two mooring lines placed on the upstream side of the structure, at an angle with the waves and current. The two upstream mooring lines are defined as line 2 and 3, see figure A.1 in appendix A.3. It is assumed that these lines experience the largest force from the waves and the current, and are thus most comparable for both structures.

In table A.5 (appendix A.3), the minimum breaking strength of each mooring line material is presented. For chain grade R3 and polyester rope of WindFloat, the minimum breaking strength is 4767 kN and 2113 kN, respectively. For wire rope of OC3-Hywind, the minimum breaking strength is 4530 kN. The maximum mooring line tension for WindFloat is found to be 2049 kN. It is experienced in line 2 during a 100-year storm with misaligned wind (LC6) and second-order QTF wave force. However, the tension at the fairlead is less than the minimum breaking strength of a polyester rope of 2113 kN. Thus, the mooring lines of WindFloat do not break during the defined environmental conditions in this thesis.

The maximum tension at the fairleads of OC3-Hywind is found to be 3676.5 kN. It is experienced during load case 6 with second-order QTF wave force in line 2, as for WindFloat. However, the tension is less than the minimum breaking strength of a wire rope of 4530 kN. Thus, the mooring lines of the spar FWT do not break during the defined extreme conditions in this thesis.

The mooring lines of WindFloat have lower fairlead tensions than the mooring lines of OC3-Hywind. The spar mooring line tensions are in general 20-40 % higher. These results may be connected with the platform response standard deviations which in general are larger for the spar OC3-Hywind, as seen in section 8.1. Larger platform movements mean that the lines will be subject to stronger forces.

The results are somewhat unclear in regard to which mooring line is subject to the highest tensions. For the expected operational conditions in LC1, the differences between the two lines are small, i.e. in the order of 1 %. For the maximum operational condition (LC2), the tensions in line 3 are highest. Regarding OC3-Hywind during the first extreme load case (LC3), the tension in line 2 is smaller than in line 3. The mooring line tensions of WindFloat for LC3 are quite similar, with only 0.1 % difference.

Regarding load case 5, with 100-year aligned conditions, there is a difference whether only first-order wave forces or second-order wave forces are included as well. With only first-order wave forces, the tension in line 3 exceeds the tension in line 2, as for LC3. However, when second-order QTF wave forces are included in the analysis, the tension in line 2 exceeds line 3. When the wind is misaligned, the tension is in general greatest in line 2. The exception is for OC3-Hywind under first-order wave forces and 100-year

misaligned wind (LC6), where line 3 tension is somewhat higher.

These inconsistencies might be due to the body form of the FWTs and their respective motions, as second-order wave forces are sensitive to the body form, among other factors.

The mooring line tension increases, for increasing wind speed, wave height, wave period and current speed, as expected. Nevertheless, the tension is more extensive under the expected operational conditions when the wind is below rated, than under the maximum operational conditions.

For mooring line 2, the tension is in general greatest when the wind is misaligned as in LC4 and LC6, compared to LC3 and LC5, respectively. For the semi-submersible WindFloat, the tension during misaligned wind is approximately 5-7 % higher than for aligned conditions, while for the spar OC3-Hywind, the tension during misaligned wind is approximately 35 % higher. Some inconsistent results are apparent, e.g. OC3-Hywind under 100-year conditions. For the first-order wave force, the tension is fairly larger for aligned wind. During a second-order QTF wave force, the tension is 17 % higher for misaligned wind, than aligned wind and waves. Regarding mooring line 3, the tension is consistently higher for aligned wind conditions.

The results discussed above can be explained by the connection between the wind direction and the position of the lines. According to figure A.1, the fairlead of mooring line 3 is positioned with positive y-coordinate, while the fairlead of mooring line 2 with negative y-coordinate. The misaligned wind at 90° is propagating in the positive y-direction. This means that mooring line 2 is assumed to be subject to the highest tensions at the fairlead connections. Additionally, the inconsistent results discussed above could be connected to the platform offsets during only wind and only wave conditions. However, due to time restrictions, those results are not found in this thesis. It is strongly suggested to perform this investigation during future work.

Table 8.5: Maximum of the axial force at the fairleads of mooring line 2 and 3

Mooring line 2 tension [kN]

	First-order wave		Second-order QTF	
	OC3	WF	OC3	WF
LC1 - exp. op.	1364.7	959.4	1363.0	964.0
LC2 - max. op.	1180.7	769.1	1150.6	814.4
LC3 - 50-year, aligned	1950.5	1574.0	1997.1	1789.9
LC4 - 50-year, misal.	3061.4	1688.4	3024.0	1900.0
LC5 - 100-year, aligned	2649.4	1695.4	3059.9	1924.6
LC6 - 100-year, misal.	2631.1	1824.2	3676.5	2049.7

Mooring line 3 tension [kN]

	First-order wave		Second-order QTF	
	OC3	WF	OC3	WF
LC1 - exp. op.	1339.9	965.9	1343.1	970.4
LC2 - max. op.	1249.4	854.2	1290.7	901.4
LC3 - 50-year, aligned	2056.8	1577.1	2143.7	1787.1
LC4 - 50-year, misal.	1825.3	1283.8	1957.3	1477.7
LC5 - 100-year, aligned	2866.3	1687.8	2919.4	1911.6
LC6 - 100-year, misal.	2686.0	1348.5	1910.2	1556.2

8.4 Power Spectra

In order to assess the contribution from the hydrodynamic loads, the power spectral density (PSD) of the loads and FWT responses are presented. The energy of the platform forces and responses have been analysed for load cases 1, 3 and 5. In figure 8.5-8.7, the PSD for the surge, heave and pitch motions of the two FWTs under extreme 50-year conditions (LC3) are presented. In figure C.3, the PSD for surge, heave and pitch motions are presented for 100-year conditions (LC5).

In the literature study in chapter 2, the effects of second-order forces on the responses and forces of floating wind turbines were discussed. The effect of the QTF force and Newman's approximation was indeed also investigated by several researchers. In general, Newman's approximation underestimates the slow-drift forces and responses around the relevant DoF's natural frequency.

8.4.1 Response Spectra

The incident wave frequency is 0.38 rad/s in LC3 and 0.37 rad/s in LC5. It is apparent from the spectra below that all motions induce resonant responses around the wave frequency, and that the resonance peaks are not influenced by first-order, second-order wave drift forces or second-order QTF wave forces. The differences in the energy distribution between the wave forces are more apparent around the respective motion resonant frequencies, which will be discussed next.

The surge natural frequencies for OC3-Hywind and WindFloat are 0.051 rad/s and 0.059 rad/s, respectively. Duarte et al. (2014) report that the surge motion PSD of OC3-Hywind is only influenced by the second-order loads under extreme wave conditions and normal wind. Thus, figure 8.5a corresponds well as only a small underestimation of the response is visible for OC3-Hywind around the natural frequency. Regarding the surge motion PSD of WindFloat, H. C. Kim and M. H. Kim (2015) report that the surge motion is underestimated when first-order wave forces are applied. Newman's approximation should correspond better with the second-order QTF, however, a small underestimation is distinguishable in figure 8.5b. These results also correspond quite well, especially for OC3-Hywind, with the fact that Newman's approximation is valid for natural periods above 100 s.

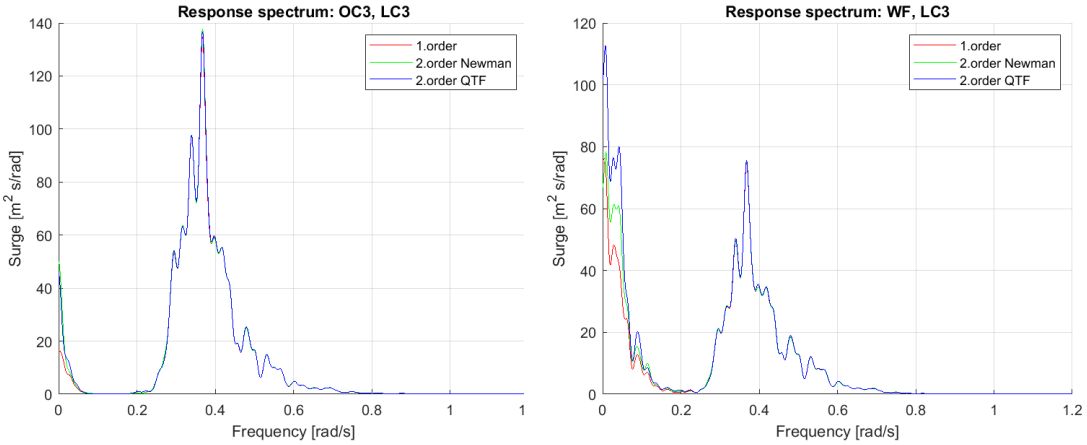

(a) OC3-Hywind - Surge PSD

(b) WindFloat - Surge PSD

Figure 8.5: Power spectral density of the surge motion during LC3

In figure 8.6a, an underestimation of the heave motion of OC3-Hywind is clearly visible around 0.2 rad/s. The natural frequency in heave of OC3-Hywind is 0.204 rad/s, thus, the PSD corresponds well with the theory and literature study where first-order and second-order Newman's approximation underestimates the second-order QTF wave force. The natural frequency of WindFloat in heave is 0.32 rad/s, where a small underestimation is noticeable in figure 8.6b. This is illustrated in the small square which shows the PSD zoomed in at the peak around 0.35 rad/s. However, H. C. Kim and M. H. Kim (2015) investigated the effect of second-order loads on the OC4 semi-submersible, and report that the heave motion spectrum shows approximately no difference between first-order, second-order Newman's and second-order QTF for the heave PSD. Thus, the results presented here correspond quite well, even though a small underestimation is visible.

In figure 8.7a, no underestimation of the pitch response spectrum is clearly visible for OC3-Hywind. However, around the pitch natural frequency 0.215 rad/s a small difference of approximately 0.2 deg s^2/rad is visible, which is illustrated by the small zoomed-in square. This corresponds with the results by Duarte et al. (2014), who report that the pitch motion spectrum is influenced by the second-order difference-frequency QTF and that Newman's approximation underestimates the energy distribution around

the natural frequency. Regarding WindFloat, the natural frequency in pitch is 0.167 rad/s. H. C. Kim and M. H. Kim (2015) reported that the pitch motion spectrum is underestimated when linear and Newman's approximation is applied. This supports the obtained results in figure 8.7b around frequency 0.2 rad/s.

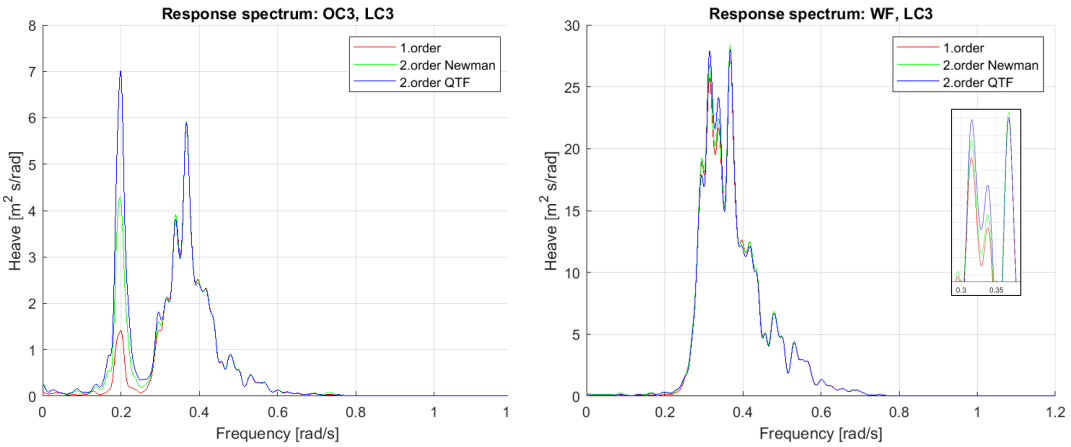

(a) OC3-Hywind - Heave PSD (b) WindFloat - Heave PSD

Figure 8.6: Power spectral density of the heave motion during LC3

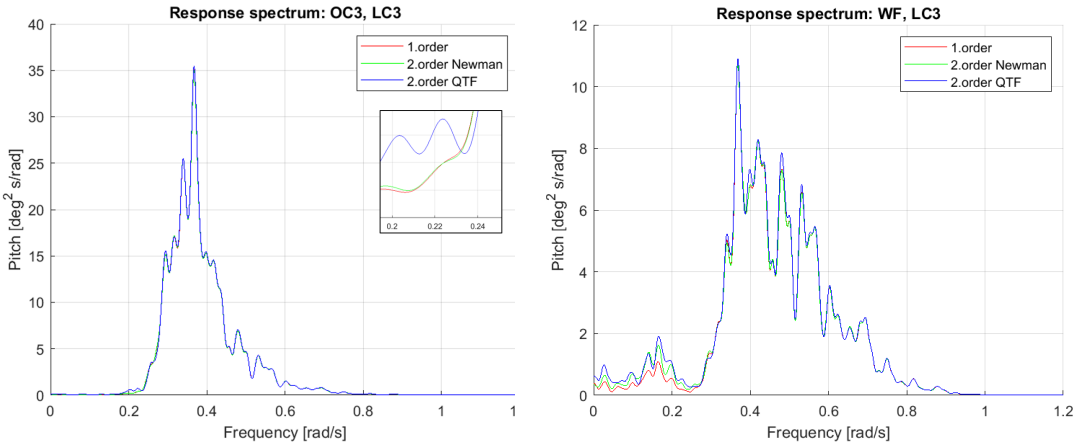

(a) OC3-Hywind - Pitch PSD (b) WindFloat - Pitch PSD

Figure 8.7: Power spectral density of the pitch motion during LC3

Furthermore, the energy distributions for the surge and pitch motions are greater for the spar OC3-Hywind than for WindFloat. For surge PSD, the difference is approximately 45 %, while for pitch PSD, the energy distribution is approximately 68 % larger for OC3-Hywind. The opposite case is true for the heave motion spectrum, where the energy distribution of WindFloat has a higher peak.

In figure 8.8, the power spectral densities of surge, heave and pitch motion of both FWTs are presented for load case 5, where the environmental conditions are for a 100-year return period. Comparing these to the corresponding spectra for load case 3, the energy distributions are of similar shape. Furthermore, the peaks of the energy

distribution are greater for the load cases with 100-year conditions, as expected.

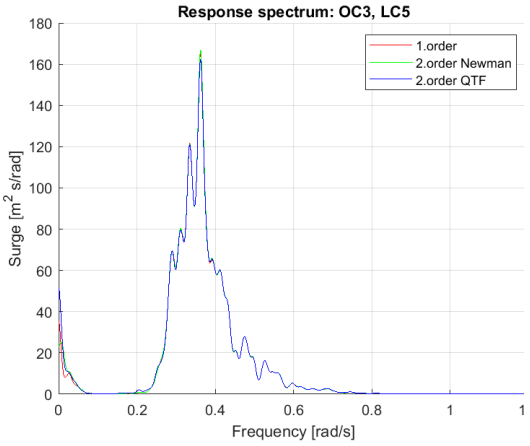

(a) OC3-Hywind - Surge PSD

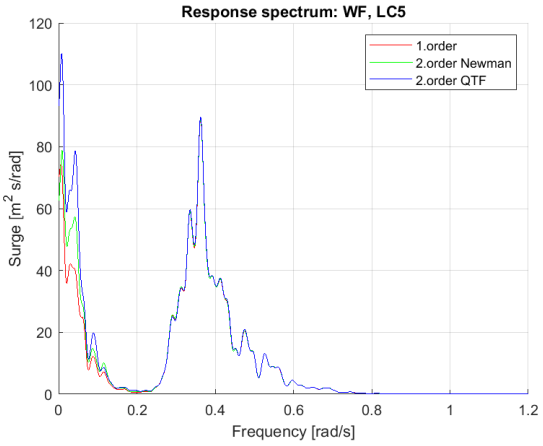

(b) WindFloat - Surge PSD

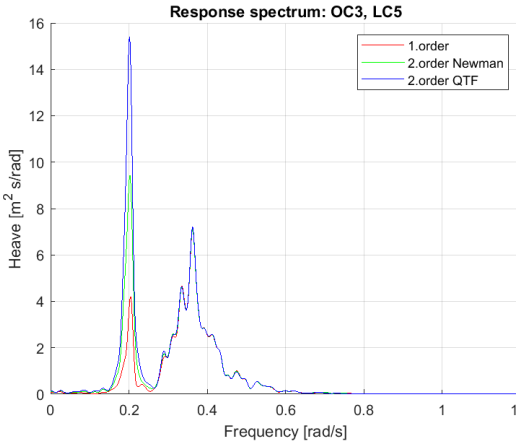

(c) OC3-Hywind - Heave PSD

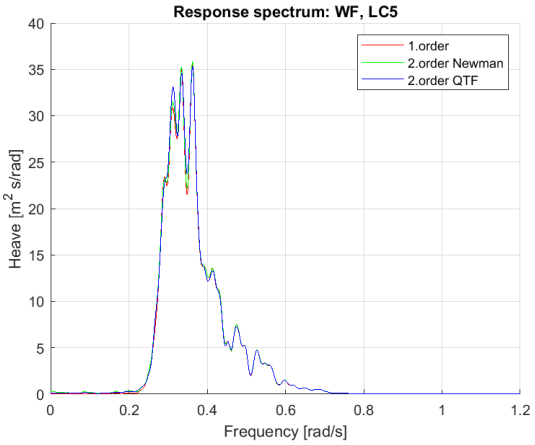

(d) WindFloat - Heave PSD

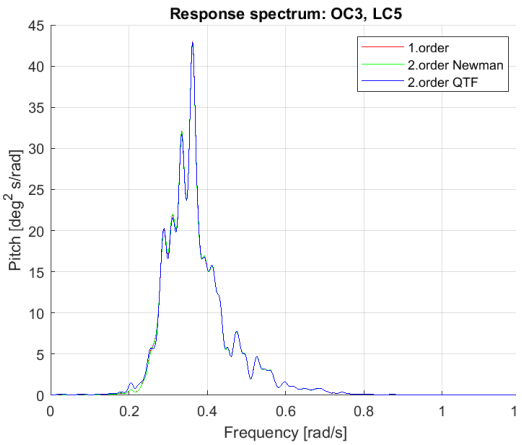

(e) OC3-Hywind - Pitch PSD

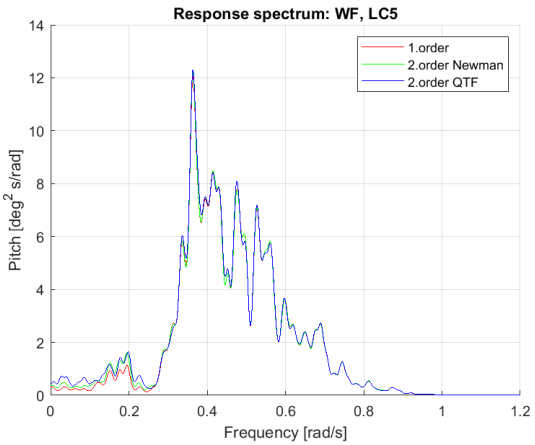

(f) WindFloat - Pitch PSD

Figure 8.8: Power spectral density of the surge, heave and pitch motion during LC5

In appendix C.1, the response spectra for surge, heave and pitch motion during the expected load case (LC1) are presented. The spectra are in general quite similar for first-order, second-order Newman's and second-order QTF wave forces for both FWTs and all degrees of freedom. The surge motion spectra correspond well to the results of Duarte et al. (2014), who reported that the surge motion under normal operating conditions is not significantly influenced by the second-order forces. However, they reported an influence of the second-order forces on the pitch spectra. This influence is not observed with these results.

8.4.2 Force Spectra

The power spectra of two hydrodynamic forces are presented next. In figure 8.9, the spectra of the surge and heave forces during 50-year conditions (LC3) are presented. In correspondence with the force time-series presented in figure 8.3, the second-order force spectra are significantly smaller than the first-order force spectra. Consequently, in order to illustrate the first-order and second-order spectra together, the second-order forces are multiplied by ten. The spectra for load case 5, with 100-year conditions, are presented in appendix C.2. The shape of the energy distribution is similar, however, once again, the energy peaks are higher for higher return period.

The second-order QTF wave forces are seen to induce more energy on WindFloat than on OC3-Hywind, for both surge and heave force. The energy distribution of surge second-order wave force by Newman's approximation is underestimated compared to the QTF force. The first-order wave force induces approximately equal amount of energy on the two structures for the surge PSD, however, over a larger range of frequencies for the semi-submersible. Regarding the heave PSD, the energy peak of WindFloat is higher by a large extent.

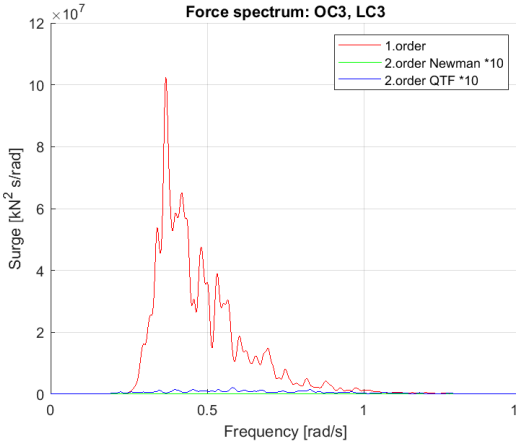

(a) OC3-Hywind - Surge PSD

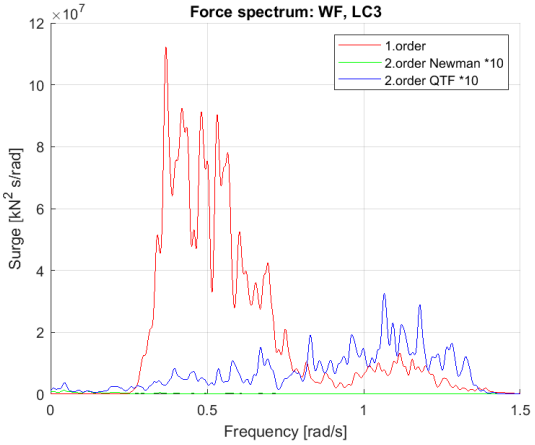

(b) WindFloat - Surge PSD

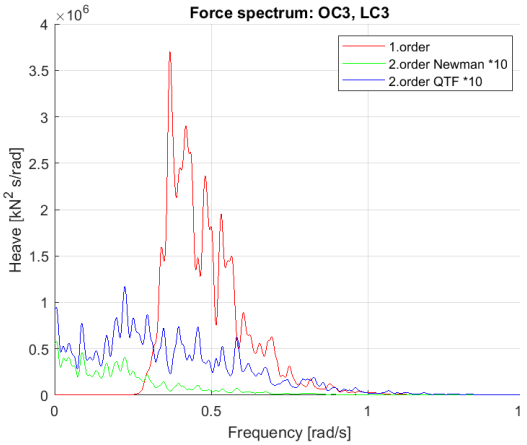

(c) OC3-Hywind - Heave PSD

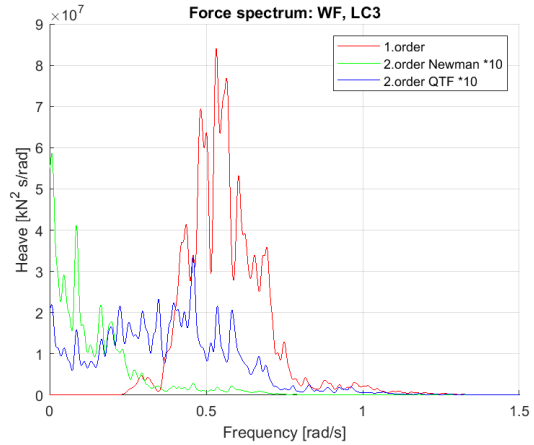

(d) WindFloat - Heave PSD

Figure 8.9: Power spectral density of the surge and heave force during LC3

8.5 Effect of Wave Drift Damping

As explained in chapter 3, the wave drift damping of a structure's horizontal motions are connected with it's ability to generate waves. The damping is caused by second-order effects from the wave-body interaction and is proportional to the body speed. Therefore, it was decided to perform a small investigation on the effect of the wave drift damping of the two FWTs. However, it is suggested that a more thorough investigation is performed for future work.

In figure 8.10 and 8.11, a part of the time series of the horizontal platform responses are presented for load case 3 (50-year aligned conditions). The responses from first-order force (red line), second-order wave drift force by Newman's approximation (green line), second-order QTF wave force (blue line with asterisk) and second-order wave drift damping force by Newman's approximation (black line with asterisk) are presented. It is observed that the surge, sway and yaw motion of WindFloat (figure 8.11) are quite similar for each type of force analysis. Thus, the wave drift damping has limited effect on the horizontal responses of the semi-submersible WindFloat.

In regard to OC3-Hywind, the surge platform response is quite similar for the first-order and different second-order wave forces. However, the effect on the sway and yaw motion is quite distinct. The first-order wave force produces the largest sway motion, in general. The motions due to the second-order forces are somewhat smaller, out of phase compared to the other wave forces and they produce different motion periods. Regarding the yaw motion, there is no clear trend, however, the second-order wave drift damping force does in some instances produce the largest platform response.

The above-mentioned results can be observed in relation to the results presented in table 8.1. Those platform responses are taken from the second-order QTF wave force analysis, and it was stated that the motion results were fairly similar to the corresponding first-order and second-order wave drift results. This corresponds to the results presented here, for WindFloat and the surge motion of OC3-Hywind. However, the platform motions presented in table 8.1 are only for surge, heave and pitch. Nevertheless, results from an analysis with second-order wave forces require a high degree of accuracy, and they are sensitive to wave heading, body motion, wave length, wave height and body form (Faltinsen 1993). As the four former are equal for all cases in question, it is assumed that the body form of the two FWTs influence the responses significantly.

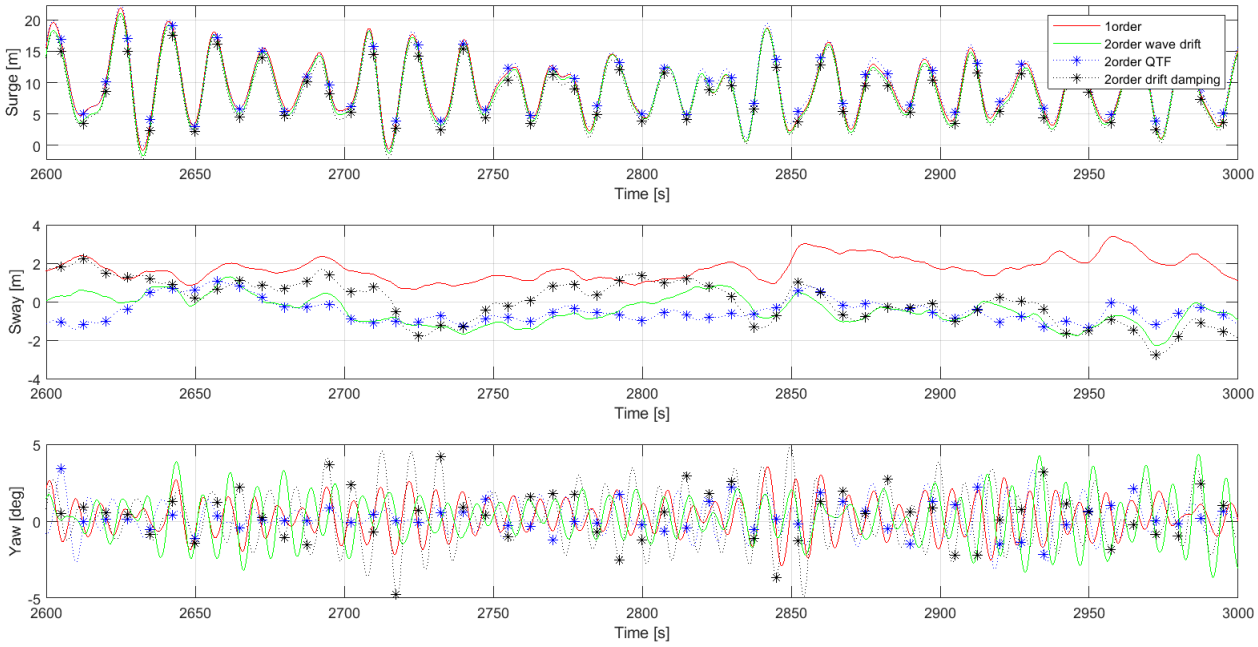

Figure 8.10: Platform response of OC3-Hywind - effect of wave drift damping

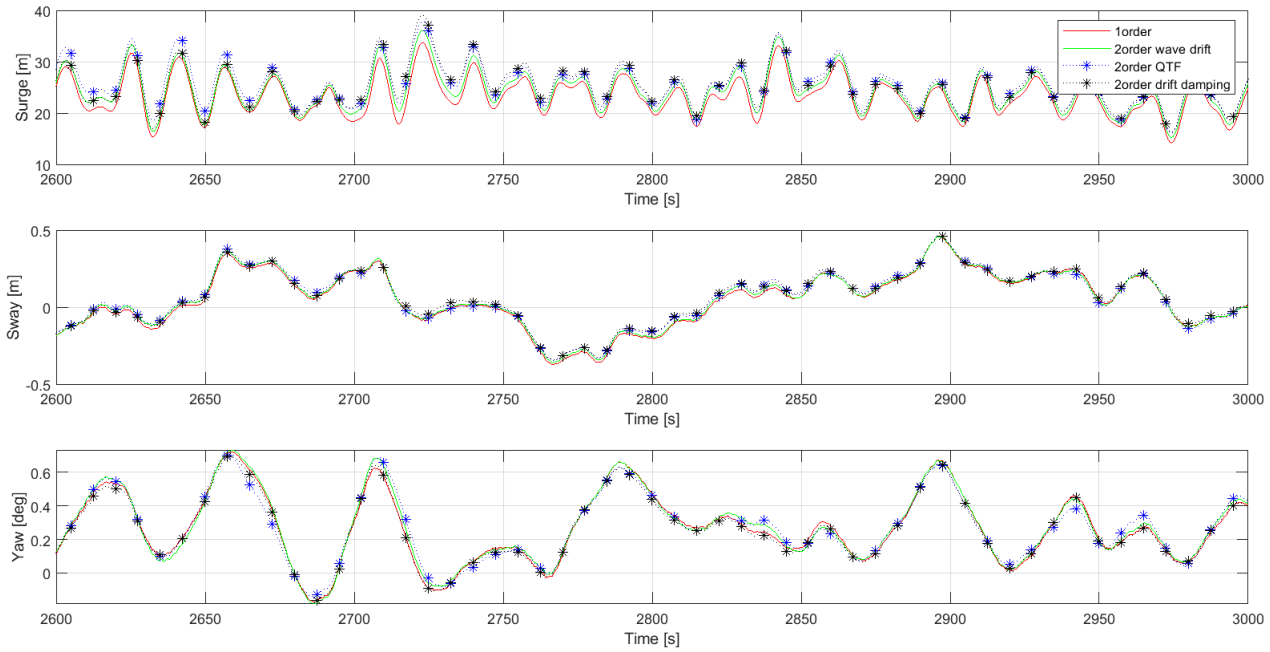

Figure 8.11: Platform response of WindFloat - effect of wave drift damping

In figure 8.12 and 8.13, the surge, sway and yaw forces of the two FTWs are presented, computed by second-order wave drift forces by Newman's approximation (green line), second-order QTF wave forces (blue line with asterisk) and second-order wave drift damping forces and Newman's (black line with asterisk). As described in section 8.2.4, the second-order forces are significantly smaller in magnitude than the first-order forces. Therefore, to simplify the illustration and the presentation of the results, the first-order forces are not presented here.

Regarding the surge and sway motion, the second order forces computed by Newman's approximation are fairly similar in magnitude, i.e close to zero. The QTF force is larger, yet there are differences between OC3-Hywind and WindFloat in the force magnitude. The surge forces are in the order of 10^2 for OC3-Hywind and 10^3 for WindFloat. The corresponding order of magnitudes for sway are 10^{-1} and 10^{-3}.

In terms of the yaw forces, the second-order wave drift (by Newman's approximation) and QTF wave forces are equal in both shape and magnitude, for each respective structure. The force magnitudes of both FWTs are approximately constant zero kNm. The second-order force computed with wave drift damping and Newmans's approximation is, however, different in magnitude between the two structures. Regarding WindFloat, the force is in the order of 10^2, while for OC3-Hywind it oscillates around zero. Thus, the wave drift damping affects the yaw second-order force of the spar platform OC3-Hywind to a certain degree.

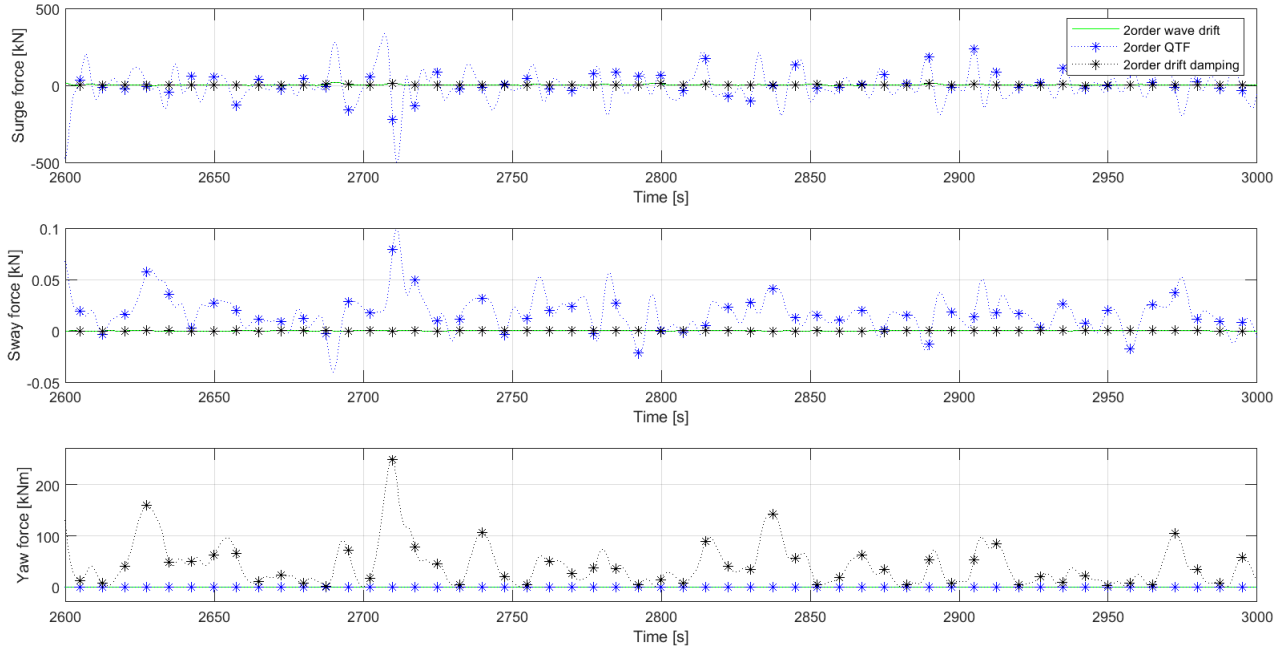

Figure 8.12: Platform hydrodynamic forces of OC3-Hywind - effect of wave drift damping

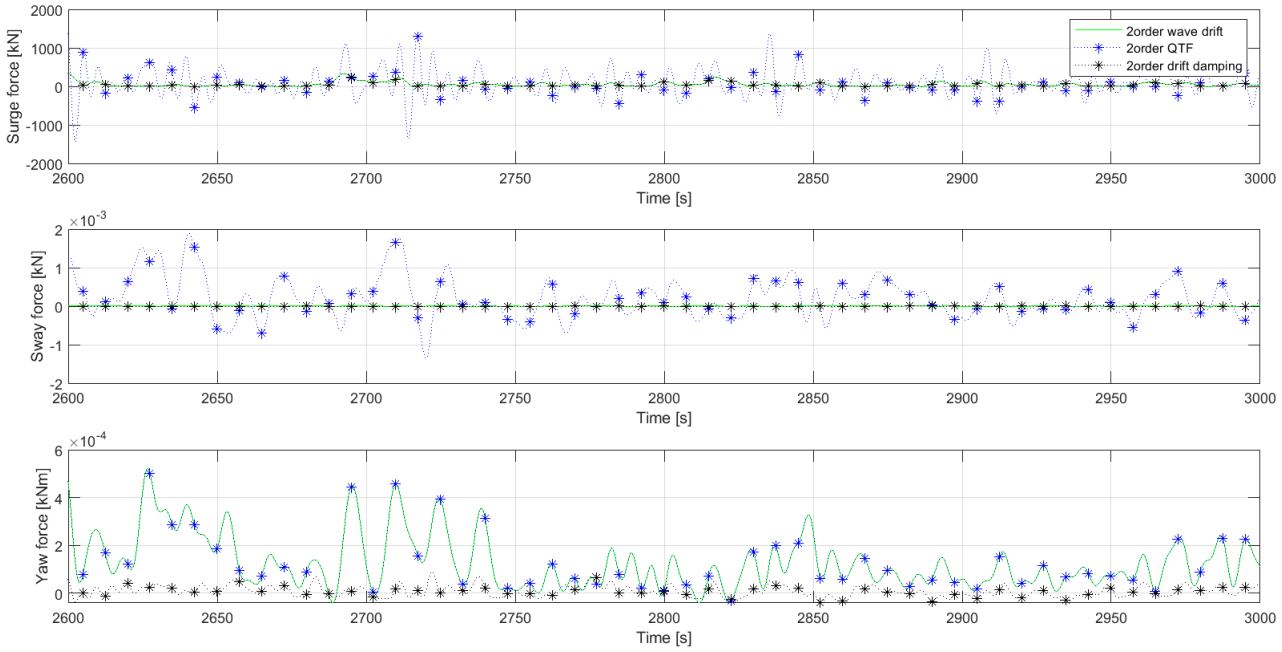

Figure 8.13: Platform hydrodynamic force of WindFloat - effect of wave drift damping

8.6 Viscous Forces on the WindFloat Heave Plates

To illustrate how the viscous forces on the heave plates of WindFloat can be accounted for, a brief iterative process was performed. The viscous forces are defined to be a correction to the potential theory added mass A_{33} due to the presence of the heave plates. In table 8.6, the corrected added mass coefficient, damping coefficient, quadratic drag coefficient and KC-number on the heave plates are presented. The original model is defined as the numerical model utilised in the previous simulations described in the sections above. The values are determined by following the process described in section 6.5.2. A quadratic drag on the heave plates is already implemented in the original model by reference to Kvittem (2014), while the added mass is not accounted for.

Ideally, this process would be performed for all load cases, in addition to perform the iteration until convergence. However, the iteration performed here was not completed due to time limitations. The viscous forces was only found for one load case (LC1), and only one iteration was performed. However, based on the results in table 8.6, the KC-number for this specific load case seems to have converged.

Table 8.6: Viscous effects on the heave plates - LC1

	A_{33}^{corr} [kg]	B_{33} [kg/s]	C_D [-]	KC [-]
Original model	-	-	7.5	0.04994
Iterated	2.91E+05	3.45E+05	18.95	0.04990

The iterated drag coefficient on the heave plate is significantly larger than the value utilised in the simulations earlier in the thesis. However, the drag coefficients were also found for the other cases with the original model, and for the extreme cases, the drag coefficients were found to be around 8.2, which is closer to the defined C_D of 7.5. It is assumed that an iteration process performed until convergence for all load cases would present improved results for all load cases.

Table 8.7: First-order wave force platform motions - LC1

	Surge [m]	Sway [m]	Heave [m]	Roll [deg]	Pitch [deg]	Yaw [deg]
Original	2.6087	0.2900	0.1206	0.3508	1.8659	1.3658
Iterated	2.5929	0.2900	0.1175	0.4689	2.0270	1.3729

In table 8.7, all six degrees of freedom of the platform motions are presented for the original and the iterated values for load case 1 by first-order wave force computation. As observed, the differences in motion between the two cases are small. Four decimals are included to illustrate the order of difference. The largest differences are found for roll and pitch motions. As the KC-number on the heave plates for this load case is small, the drag forces are assumed to be dominated by the inertia forces. Thus, since the difference in KC-number for the original and iterated model is negligible, the effect of the large difference in drag coefficient is minor on the platform motions. The effect on the hydrodynamic forces is non-existent, and thus not presented here.

Chapter 9

Conclusion and Summary

9.1 Conclusion

The models were verified successfully through results from the hydrodynamic analyses in HydroD and by free decay tests in SIMA. The mean drift forces, response amplitude operators, eigenperiods and the quadratic transfer functions were used for the verification. The pitch RAO of WindFloat was affected by the heave plate thickness between the author's model and the provided model used for verification. The free decay tests corresponded well with reference values, except yaw natural period of WindFloat. That inconsistency is explained by the coupling effects between sway and yaw during the yaw free decay tests. In addition, the wind turbine performance of both FWTs was verified towards the reference turbine.

The semi-submersible WindFloat has a larger offset in surge and heave during extreme conditions than OC3-Hywind, while OC3-Hywind is subject to the largest motion variation. This is due to the design where spar-buoys are designed for small motions, while semi-submersibles are designed for large motions due to the small draft. The results show inconsistent trends between the two platforms regarding the structural loads axial force and bending moment. The tower of OC3-Hywind withstands the extreme conditions better than WindFloat, with regard to axial force. With regard to bending moment, the tower of WindFloat withstands the extreme conditions better. These inconsistencies are assumed to appear due to the different body forms of the floating structures. With regard to the turbine thrust, the results show good agreement between the two FWTs, which is to be expected, since both are based on the 5 MW NREL turbine. Further, the mooring line tensions of the fairleads are quite smaller on WindFloat, than on OC3-Hywind, which can be connected to the platform motion responses.

Most of the analysed response variables presented in this thesis increase in magnitude with increasing return period of the conditions, as expected. The exception is the thrust on the turbine shaft, which decreases for wind speeds above the cut-out wind speed. This is due to the parked condition and feathering of the blades. During aligned conditions, the results are inconsistent in which mooring line is exposed to the largest tension. This is assumed to be affected by the body form and platform motions.

The misalignment of wind and waves has been shown to greatly affect several of the analysed aspects. The platform responses are not significantly affected, while the struc-

tural loads are influenced a great deal. The tower of OC3-Hywind is subject to significantly smaller variation in the axial force when the wind is misaligned, than during aligned conditions. The opposite is the case for the tower of WindFloat. However, the tension in mooring line 2 is consistently larger than in line 3 during misaligned conditions, due to the direction of the wind and the upstream position of line 2.

The platform motions, structural loads and aerodynamic thrust are not significantly influenced by the second-order wave forces. However, the hydrodynamic forces on the platforms are greatly influenced, where the second-order forces are a great deal smaller than the first-order forces. This is observed in the time-series and the force spectra, and corresponds with the theory. The mooring line tensions are somewhat lower during a first-order wave force, than during a second-order difference-frequency wave force.

9.2 Further Work

The following are suggestions for further work, based on the simulations and results found during the work with this master's thesis.

- The effect of the heave plates of WindFloat could be subject to further work, both in regard to the effect of a case without the plates, and to the viscous forces on the heave plates. The main simulations in this thesis exclude a correction to the potential theory added mass contribution due to the heave plates. An investigation of this correction should thus be performed.
- In addition, investigation and optimisation of the heave plate thickness on this modified WindFloat FWT are suggested for further work. The structural loads on the conjunction between the plates and the columns are proposed as a way of defining a suitable thickness, in combination with other aspects.
- The results presented were inconsistent with regard to which tower and platform is structurally better during extreme conditions. A more thorough investigation is thus proposed. Additionally, the effect of the misalignment of the wind and waves on the structural loads is a possible subject for further studies.
- Further investigation of the mooring line tensions during both aligned and misaligned extreme conditions, with regard to which line is subject to the highest tensions. This can be connected to the offset of the platforms under simulations with only wind and only waves, to assess the relevance of each met-ocean aspect on the motions and line tensions.
- The effects of the wave drift damping was only briefly studied here, with inconsistent results with regard to both platform motions and forces of both FWTs. Thus, it is suggested to further investigate this effect.

Bibliography

Aubault, A. and C. Cermelli (2009). "WindFloat: A Floating Foundation for Offshore Wind Turbines Part lll: Structural Analysis". In: *ASME 2009 28th International Conference on Ocean, Offshore and Arctic Engineering*.

Azcona, J. et al. (2014). *D4.22 Methods for Performing Scale-Tests for Method and Model Validation of Floating Wind Turbines*. Ed. by A. Manjock.

Azcone, J. et al. (2013). *D4.21 State-of-the-Art and Implementation of Design Tools for Floating Structures*. Ed. by J. Azcona Armendàriz.

Bachynski, E. (2018). *Lecture Notes "Integrated Dynamic Analysis of Wind Turbines"*.

Bae, Y. H. and M. H. Kim (2014). "Aero-Elastic-Control-Floater-Mooring Coupled Dynamic Analysis of Floating Offshore Wind Turbine in Maximum Operation and Survival Conditions". In: *Journal of Offshore Mechanics and Arctic Engineering* 136.2.

Borg, M and H. Bredmose (2015). *D4.4 Overview of the Numerical Models Used on the Consortium and Their Qualification*.

Cermelli, C., D. Roddier, and A. Aubault (2009). "Windfloat: A Floating Foundation for Offshore Wind Turbines Part II: Hydrodynamics Analysis". In: *ASME 2009 28th International Conference on Ocean, Offshore and Arctic Engineering*. Vol. 4, pp. 135–143.

Consortium, FukuShima Offshore Wind (2018). *Fukushima Floating Offshore Wind Farm Demonstration Project (FORWARD)*. URL: `http://www.fukushima-forward.jp/english/index.html`.

DNVGL (2015a). *DNVGL-OS-E304 Offshore Mooring Steel Wire Ropes*. Ed. by DNV GL.

— (2015b). *SESAM User Manual - GeniE*. Ed. by DNVGL.

— (2015c). *SESAM User Manual - WADAM*. Ed. by DNVGL.

— (2016). *SESAM User Manual - HydroD*. Ed. by DNVGL.

— (2017). *DNVGL-RP-N103 Modelling and Analysis of Marine Operations*.

— (2018). *DNVGL-ST-0119 Floating Wind Turbine Structures*.

Duarte, T. M., A. Sarmento, and J. Jonkman (2014). *Effects of Second-Order Hydrodynamic Forces on Floating Offshore Wind Turbines*.

Equinor (2018). *Hywind - the World's Leading Floating Offshore Wind Solution*. URL: https://www.equinor.com/en/what-we-do/hywind-where-the-wind-takes-us.html.

Faltinsen, O. M. (1993). *Sealoads on Ships and Offshore Structures*.

Finne, S., J. Grue, and A. Nestegård (2000). "Prediction of the Complete Second Order Wave Drift Damping Force for Offshore Structures". In: *ISOPE 10th International Offshore and Polar Engineering Conference*.

Gao, Z. et al. (2018). "Commitee V.4 Offshore Renewable Energy". In: *20th International Ship and Offshore Structures Congress*.

GWEC (2018). *Global Wind Report 2018*. Ed. by K. Ohlenforst et al. Report.

IEC (2019a). *Wind Energy Generation Systems. Part 3-1: Design Requirements for Fixed Offshore Wind Turbines*. Ed. by IEC.

— (2019b). *Wind Energy Generation Systems. Part 3-2: Design Requirements for Floating Offshore Wind Turbines*. Ed. by IEC.

ISO (2012). *ISO 1141 FibreRopes - Polyester - 3-, 4-, 8- and 12-strand ropes*. Ed. by ISO.

— (2013). *ISO 19901-7 Petroleum and Natural Gas Industries - Specific Requirements for Offshore Structures - Part 7: Stationkeeping Systems for Floating Offshore Structures and Mobile Offshore Units*. Ed. by ISO.

Johannessen, K., T. Meling, and S. Haver (2001). "Joint Distribution for Wind and Waves in the Northern North Sea". In: *ISOPE 11th International Offshore and Polar Engineering Conference*. Vol. 12. 1, pp. 1–8.

Jonkman, J. (2009). *TurbSim User's Guide: Version 1.50*.

— (2010). *Definition of the Floating System for Phase IV of OC3*.

Jonkman, J. and W. Musial (2010). *Offshore Code Comparison Collaboration (OC3) for IEA Wind Task 23 Offshore Wind Technology and Deployment*.

Jonkman, J. et al. (2009). *Definition of a 5-MW Reference Wind Turbine for Offshore System Development*. Ed. by NREL.

Kaldellis, J. K. et al. (2016). "Environmental and Social Footprint of Offshore Wind Energy. Comparison with Onshore Counterpart". In: *Renewable Energy* 92, pp. 543–556.

Karimirad, M. et al. (2017). "Comparison of Real-Time Hybrid Model Test of a Braceless Semi-Submersible Wind Turbine and Numerical Simulations". In: *ASME 2017 36th International Conference on Ocean, Offshore and Arctic Engineering*.

Karmakar, D., H. Bagbanci, and C. G. Soares (2016). "Long-Term Extreme Load Prediction of Spar and Semisubmersible Floating Wind Turbines Using the Environmental Contour Method". In: *Journal of Offshore Mechanics and Arctic Engineering* 138.2.

Kim, H. C. and M. H. Kim (2015). "Global Performance of a Semi-Submersible 5 MW Wind-Turbine Including Second-Order Wave-Diffraction Effects". In: *Ocean Systems Engineering*.

Kvingedal, B. and M. Mathiesen (2010). *Snorre Field - Metocean Design Basis. Rev 5.* Technical Report. Equinor.

Kvittem, M. I. (2014). "Modelling and Response Analysis for Fatigue Design of a Semi-Submersible Wind Turbine". PhD thesis. NTNU.

Kvittem, M. I. and T. Moan (2015). "Frequency versus Time Domain Analysis for Fatigue of a Semi-Submersible Wind Turbine". In: *Journal of Offshore Mechanics and Arctic Engineering*.

Li, L., Z. Gao, and T. Moan (2015). "Joint Distribution of Environmental Condition at Five European Offshore Sites for Design of Combined Wind and Wave Energy Devices". In: *Journal of Offshore Mechanics and Arctic Engineering* 137.3.

Lopez-Pavon, C. and A. Souto-Iglesias (2015). "Hydrodynamic Forces and Pressure Loads on Heave Plates for Semi-Submersible Floating Offshore Wind Turbines: A Comparative Analysis Using Large Scale Models". In: *Renewable energy*.

Moreno, J., K. P. Thiagarajan, and M. Cameron (2016). "Hydrodynamic Coefficients of Hexagonal Heave Plates for Floating Offshore Wind Turbine Platforms". In: *ASME 2016 35th International Conference on Ocean, Offshore and Arctic Engineering*.

Müller, K. et al. (2018). *D7.7 Identification of Critical Environmental Conditions and Design Load Cases*.

Newman, J. N. (1974). "Second Order, Slowly Varying Forces on Vessels in Irregular Waves". In: *Intl. Symp. on Dynamics of Marine Vehicles and Offshore Structures in Waves*.

Ormberg, H. and E. Bachynski (2012). "Global Analysis of Floating Wind Turbines: Code Development, Model Sensitivity and Benchmark Study". In: *ISOPE 21th International Offshore and Polar Engineering Conference*, pp. 366–373.

PrinciplePower (2015). *WindFloat*. URL: `http://www.principlepowerinc.com/en/windfloat`.

Roald, L. et al. (2013). "The Effect of Second-Order Hydrodynamics on Floating Offshore Wind Turbines". In: *Energy Procedia*.

Robertson, A. et al. (2013). "Summary of Conclusions and Recommendations Drawn From the DeepCwind Scaled Floating Offshore Wind System Test Campaign". In: *ASME 2013 32nd International Conference on Ocean, Offshore and Arctic Engineering*.

Robertson, A. et al. (2014). *Offshore Code Comparison Collaboration Continuation Within IEA Wind Task 30: Phase II Results Regarding a Floating Semisubmersible Wind System*.

Robertson, A. et al. (2017). "OC5 Project Phase II: Validation of Global Loads of the DeepCwind Floating Semisubmersible Wind Turbine". In: *Energy Procedia* 137, pp. 38–57.

Rock, M. and L. Parsons (2010). *Environmental and Energy Study Institute: Offshore Wind Energy*. Ed. by Carol Werner.

Roddier, D., C. Cermelli, and A. Weinstein (2009). "Windfloat: A Floating Foundation for Offshore Wind Turbines Part I: Design Basis and Qualification Process". In: *ASME 2009 28th International Conference on Ocean, Offshore and Arctic Engineering*. Vol. 4, pp. 845–853.

Roddier, D. et al. (2011). "A Generic 5MW WindFloat for Numerical Tool Validation and Comparison Against a Generic Spar". In: *ASME 2011 30th International Conference on Ocean, Offshore and Arctic Engineering*.

Sauder, T. et al. (2016). "Real-Time Hybrid Model Testing of Braceless Semi-Submersible Wind Turbine: Part I - The Hybrid Approach". In: *ASME 2016 35th International Conference on Ocean, Offshore and Arctic Engineering*.

SeaTwirl (2011). *Successful Testing of the Third Prototype*. URL: `https://seatwirl.com/news/successful-testing-and-installation-of-the-prototype-p3/`.

Simos, A. N. et al. (2017). "Slow-Drift of a Floating Wind Turbine: An Assessment of Frequency-Domain Methods Based on Model Tests". In: *Renewable energy*.

SINTEFOcean (2018a). *RIFLEX 4.12.2 Theory Manual*.

— (2018b). *SIMA 3.5 User Guide*.

Tao, L. and S. Cai (2003). "Heave Motion Suppression of a Spar with a Heave Plate". In: *Ocean Engineering*.

Tao, L. et al. (2007). "Spacing Effects on Hydrodynamic of Heave Plates on Offshore Structures". In: *Journal of Fluids and Structures*.

UMaine (2019a). *New England Aqua Ventus I*. URL: `https://composites.umaine.edu/offshorewind/`.

— (2019b). *VolturnUS 1:8*. URL: `https://composites.umaine.edu/research/volturnus/`.

Utsunomiya, T. et al. (2014). "Dynamic Analysis of a Floating Offshore Wind Turbine Under Extreme Environmental Conditions". In: *Journal of Offshore Mechanics and Arctic Engineering* 136.2.

Vittori, F. et al. (2018). "Hybrid Scaled Testing of a 5MW Floating Wind Turbine Using the SiL Method Compared with Numerical Models". In: *ASME 2018 37th International Conference on Ocean, Offshore and Arctic Engineering*.

VLIZ (2016). *Marine Regions - Towards a Standard for Georeferences Marine Names*. Ed. by Flanders Marine Institute. URL: `http://www.marineregions.org/`.

Vryhof (2010). *Anchor Manual 2010 - The Guide to Anchoring*. Ed. by Vryhof Anchors.

WindEnergyTechnologiesOffice (2017). *Offshore Floating Vertical-Axis Wind Turbine Project Identifies Promising Platform Design*. Ed. by U.S. Department of Energy. URL: https://www.energy.gov/eere/wind/articles/offshore-floating-vertical-axis-wind-turbine-project-identifies-promising.

WindEurope (2018). *Wind Energy: About Wind*. URL: https://windeurope.org/about-wind/.

— (2019). *Wind Energy Today*. URL: https://windeurope.org/about-wind/wind-energy-today/.

Appendix A

Additional Specifications on the FWTs

A.1 Mass, Restoring and Inertia

Table A.1: Mass, restoring and inertia for OC3-Hywind system, including turbine and tower

Parameter	Value
Total mass	8.066E+06 kg
COG (from origo at SWL)	(-0.0139, 0.011, -78) m
Radius of gyration Rxx	47 m
Radius of gyration Ryy	47 m
Radius of gyration Rzz	1.6 m
Hydrostatic restoring heave	3.44E+05 N/m
Hydrostatic restoring roll	1.48E+09 Nm
Hydrostatic restoring pitch	1.48E+09 Nm

Table A.2: Mass, restoring and inertia for modified WindFloat system, including turbine and tower

Parameter	Value
Total mass	4.619E+06 kg
COG (from origo at SWL)	(-0.331, 0, 1.489) m
Radius of gyration Rxx	18.5 m
Radius of gyration Ryy	22.6 m
Radius of gyration Rzz	26.1 m
Radius of gyration Ryz	4.69 m
Hydrostatic restoring heave	2.35E+06 N/m
Hydrostatic restoring roll	3.76E+08 Nm
Hydrostatic restoring pitch	3.76E+08 Nm

A.2 Ballast System for WindFloat

U_w : wind speed at hub height (z = 90 m)
COG_i : centre of gravity in i = x-,y-,z-direction
I_{ij} : mass moment of inertia, where i,j = x-,y-,z-direction

The two tables below show how the centre of gravity and hull moments of inertia vary for different wind speeds, assuming that ballast water is pumped to give the platform a near-zero mean pitch angle. The values are assumed for the floating hull structure and ballast water alone, excluding the tower, turbine and mooring lines. Table A.3 is provided by co-supervisor Erin Bachynski and is used for the constant wind tests in section 7.3. The values in table A.4 are calculated based on the mass of the steel structure, mass of ballast water ((Kvittem 2014)) and mean thrust and generator torque on a fixed 5 MW WT.

Table A.3: Ballast system for WindFloat floating sub-structure - constant wind tests (Bachynski 2018)

U_w (hub)	COG_x	COG_y	COG_z	I_{xx}	I_{yx}	I_{yy}	I_{zx}	I_{zz}
[m/s]	[m]	[m]	[m]	[kgm^2]	[kgm^2]	[kgm^2]	[kgm^2]	[kgm^2]
0	-4.300	0	-7.937	1.97E+09	0.00E+00	1.52E+09	8.83E+07	2.75E+09
4	-4.580	0	-7.877	1.99E+09	0.00E+00	1.51E+09	9.57E+07	2.75E+09
6	-4.847	0	-7.817	2.00E+09	0.00E+00	1.49E+09	1.03E+08	2.75E+09
8	-5.200	0	-7.733	2.01E+09	0.00E+00	1.47E+09	1.13E+08	2.75E+09
10	-5.710	0	-7.600	2.03E+09	0.00E+00	1.43E+09	1.28E+08	2.75E+09
11.4	-5.911	0	-7.544	2.04E+09	0.00E+00	1.42E+09	1.34E+08	2.75E+09
12	-5.708	0	-7.600	2.03E+09	0.00E+00	1.43E+09	1.27E+08	2.75E+09
14	-5.431	0	-7.674	2.02E+09	0.00E+00	1.45E+09	1.19E+08	2.75E+09
16	-5.306	0	-7.706	2.02E+09	0.00E+00	1.46E+09	1.16E+08	2.75E+09
18	-5.239	0	-7.723	2.01E+09	0.00E+00	1.46E+09	1.14E+08	2.75E+09
20	-5.203	0	-7.732	2.01E+09	0.00E+00	1.46E+09	1.13E+08	2.75E+09
22	-5.188	0	-7.735	2.01E+09	0.00E+00	1.47E+09	1.12E+08	2.75E+09
24	-5.188	0	-7.735	2.01E+09	0.00E+00	1.47E+09	1.12E+08	2.75E+09

Table A.4: Ballast system for WindFloat floating sub-structure - six environmental load cases

LC	U_w (hub)	COG_x	$COGy$	$COGz$	I_{xx}	I_{yx}	I_{yy}	I_{zx}	I_{zz}
-	[m/s]	[m]	[m]	[m]	[kgm^2]	[kgm^2]	[kgm^2]	[kgm^2]	[kgm^2]
LC1	10.46	-5.750	0	-7.593	2.03E+09	2.41E+06	1.43E+09	1.28E+08	2.746E+09
LC2	25.00	-5.075	0	-7.766	2.01E+09	2.83e+06	1.47E+09	1.09E+08	2.746E+09
LC3	38.93	-4.410	0	-7.914	1.98E+09	0	1.52E+09	9.11E+07	2.746E+09
LC4	27.37	-4.290	0	-7.939	1.97E+09	0	1.52E+09	8.80E+07	2.746E+09
LC5	41.14	-4.423	0	-7.912	1.98E+09	0	1.52E+09	9.14E+08	2.746E+09
LC6	29.41	-4.288	0	-7.939	1.97E+09	0	1.52E+09	8.80E+07	2.746E+09

A.3 Mooring Lines

A.3.1 Definition of Mooring Line Placement

An illustration of the positioning of the mooring lines are given in figure A.1. The scale and angles are not necessarily correct, the figure is used to illustrate which lines the fairlead tension is taken on (line 2 and 3 of each structure). The wind, waves and current are moving in the positive x-direction.

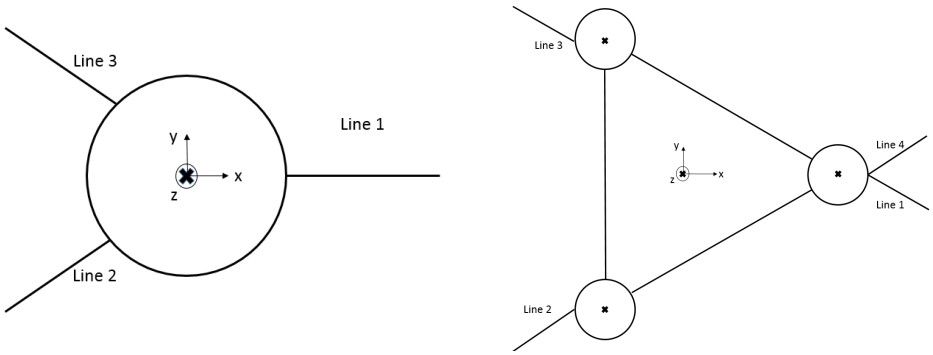

(a) OC3-Hywind (b) WindFloat

Figure A.1: Mooring line placement of OC3-Hywind and WindFloat

A.3.2 Minimum Breaking Strength

The mooring lines of WindFloat consists of chain and polyester rope, while the mooring lines of OC3-Hywind consist of only wire rope. In order to determine if the mooring lines break during the extreme environmental conditions, the minimum breaking strength (MBS) of each material is determined based on the limited information which is available. The diameter of the respective lines and the minimum breaking strengths are presented in table A.5.

Chain
ISO 19901-7 (ISO 2013) defines the MBS [kN] of Oil Rig Quality (ORQ) chain as in equation (A.1), where D is the diameter [mm]. It is assumed that the chain is of grade R3.

$$\text{MBS}_{ORQ} = 0.0211D^2(44 - 0.08D) \qquad MBS_{R3} = 1.057 \cdot MBS_{ORQ} \tag{A.1}$$

Polyester
ISO 1141 (ISO 2012) defines the MBS based on rope diameter [mm]. It is assumed that the line is of 8-stranded braided polyester rope. Based on the diameter of the rope, and with the assumption that the rope is unspliced, the minimum breaking strength is calculated with linear interpolation.

Wire Rope
DNVGL-OS-E304 (DNVGL 2015a) defines the MBS of wire rope, based on the diameter [mm]. The breaking strength is thus found through linear interpolation.

Table A.5: Minimum breaking strength for mooring line materials

Mooring line material	D [mm]	MBS [kN]
Chain R3	75	4766.6
Polyester	125	2112.5
Wire rope	90	4530.0

A.4 Performance Curves for NREL 5 MW Turbine

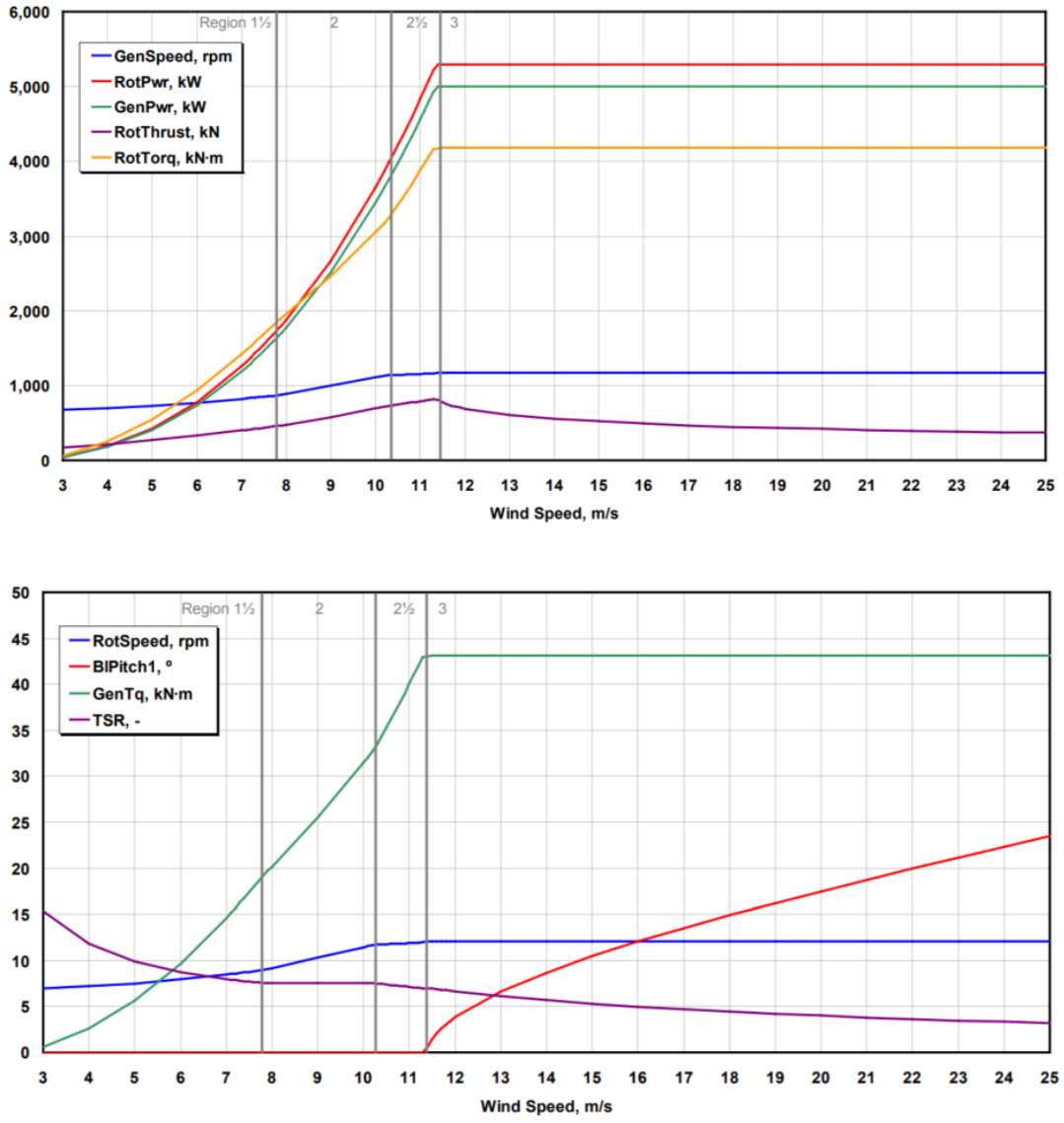

Figure A.2: Performance curves for the 5 MW NREL wind turbine (Jonkman et al. 2009)

Appendix B

Free Decay

B.1 OC3-Hywind

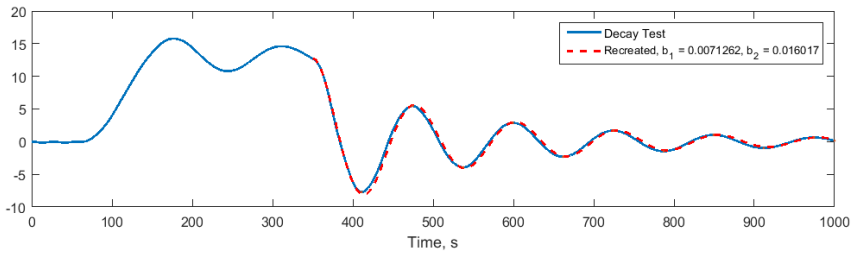

(a) Surge

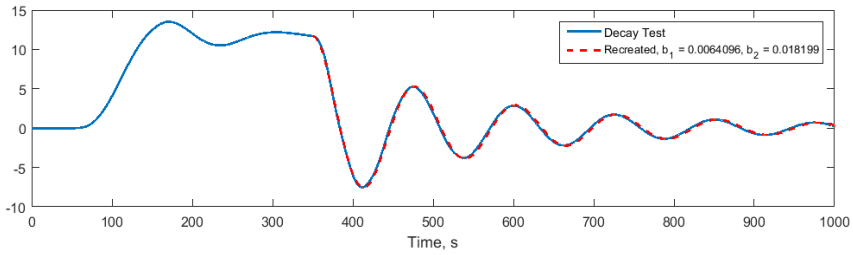

(b) Sway

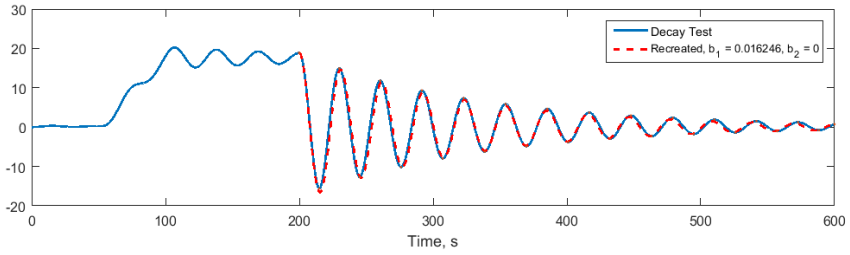

(c) Heave

Figure B.1: Free decay tests surge, sway and heave for OC3-Hywind

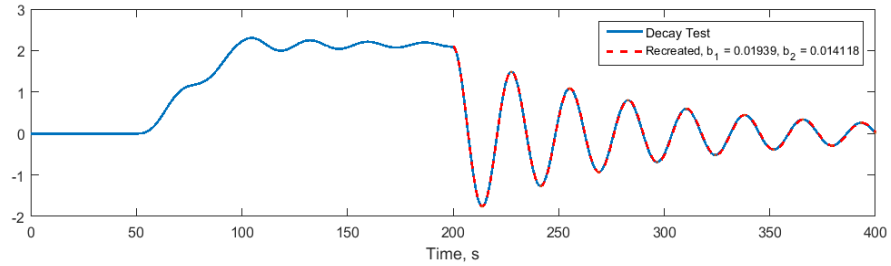

(a) Roll

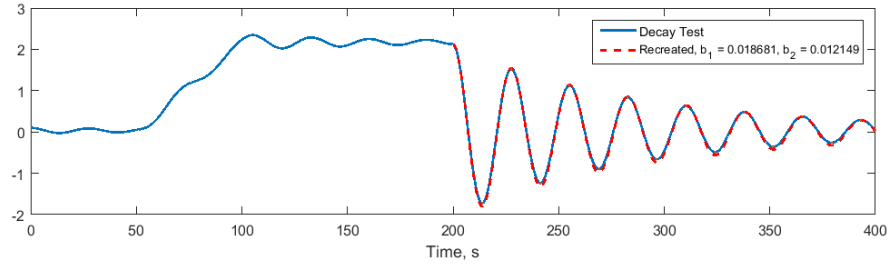

(b) Pitch

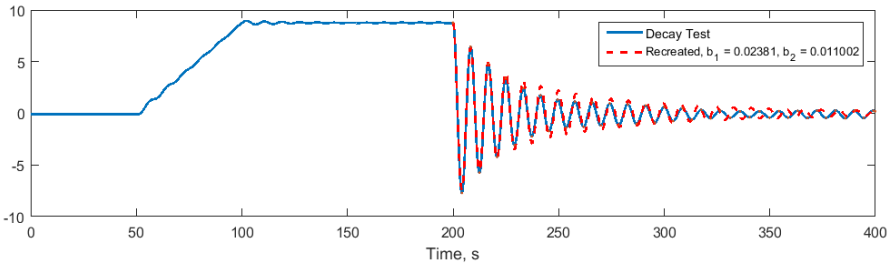

(c) Yaw

Figure B.2: Free decay tests roll, pitch and yaw for OC3-Hywind

B.2 WindFloat

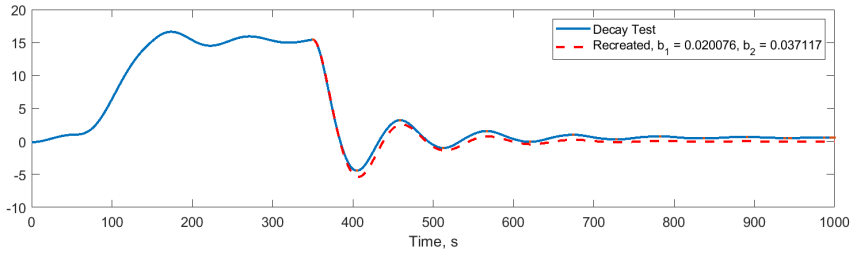

(a) Surge

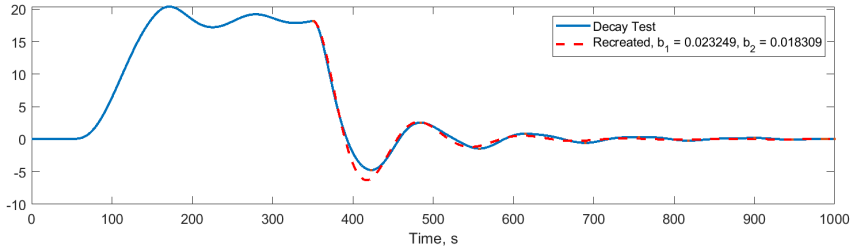

(b) Sway

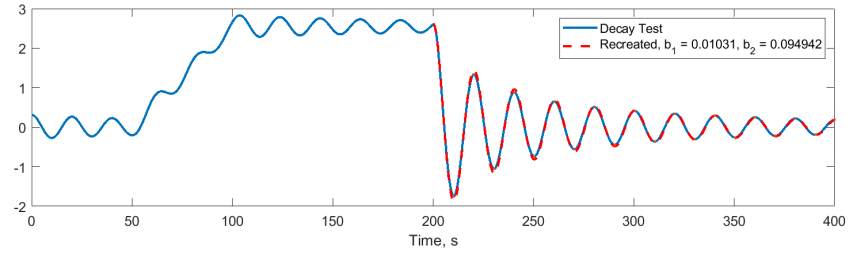

(c) Heave

Figure B.3: Free decay tests surge, sway and heave for WindFloat

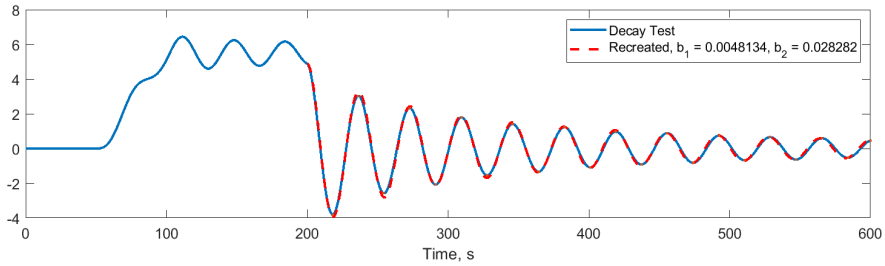

(a) Roll

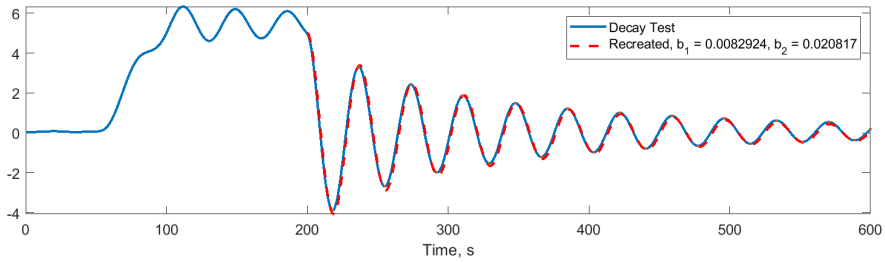

(b) Pitch

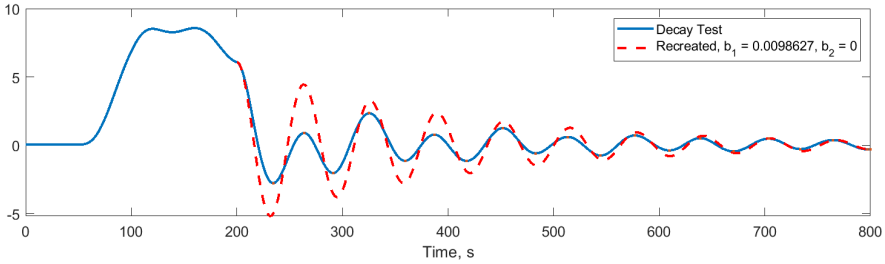

(c) Yaw

Figure B.4: Free decay tests roll, pitch and yaw for WindFloat

B.3 Coupling Effects Sway and Yaw

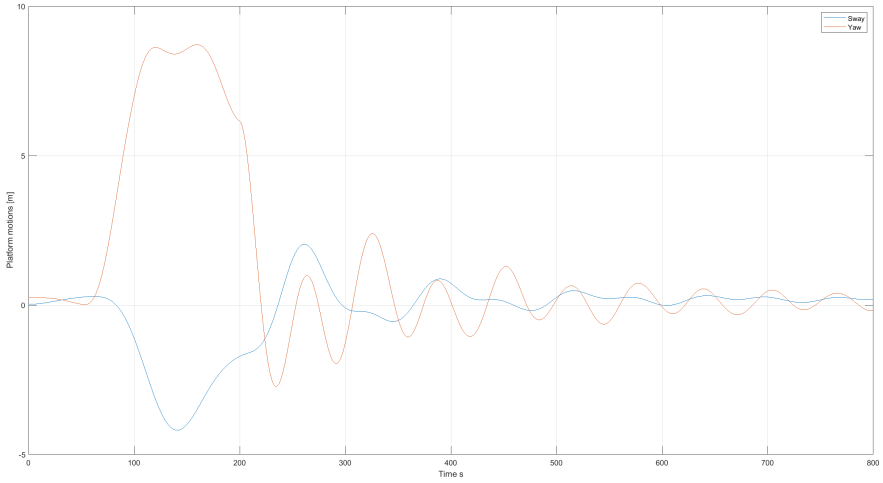

(a) Yaw decay test with coupling effects

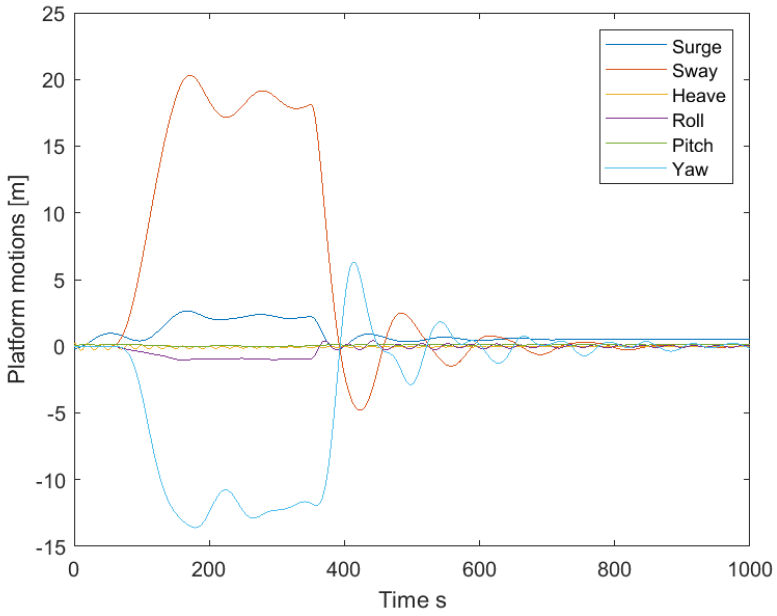

(b) Sway decay test with coupling effects

Figure B.5: Coupling effects of yaw and sway during free decay tests for WindFloat

Appendix C

Power Spectral Density

C.1 Response Spectra Load Case 1

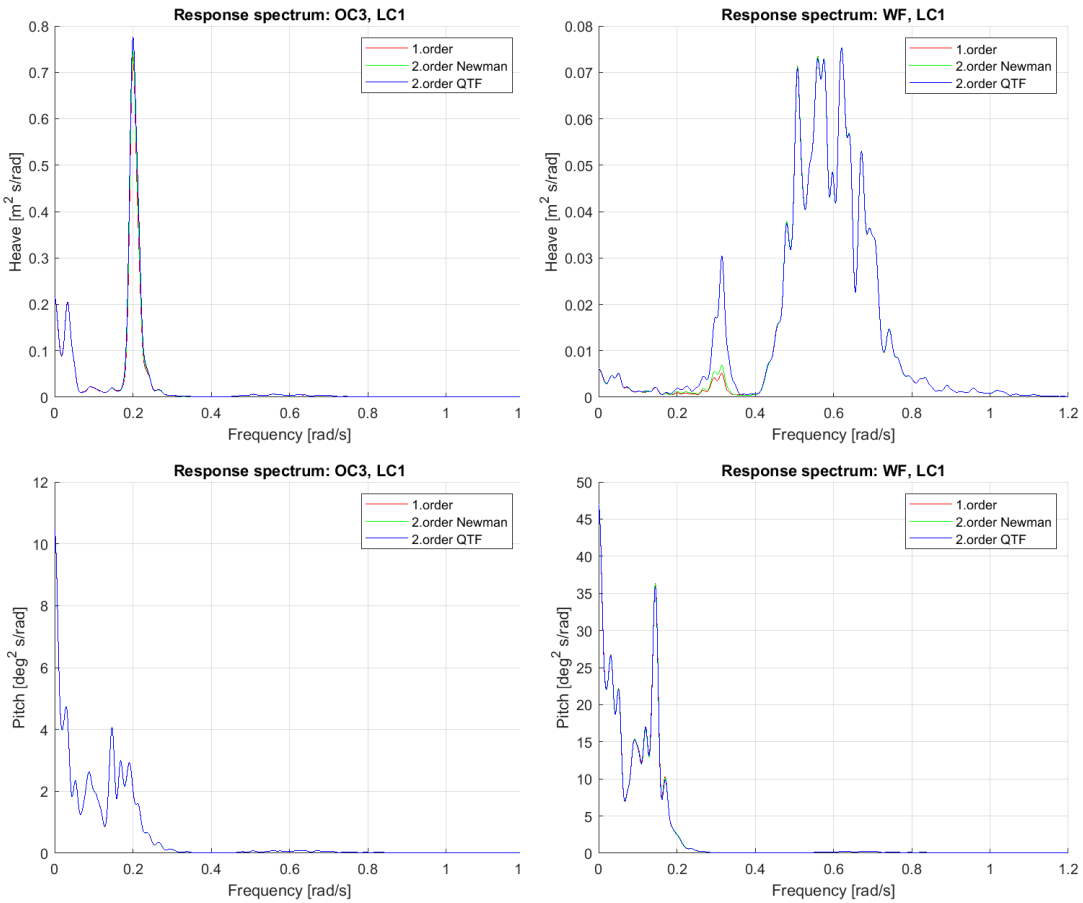

Figure C.1: Power spectral density of heave and pitch motion during LC1 for OC3-Hywind and WindFloat

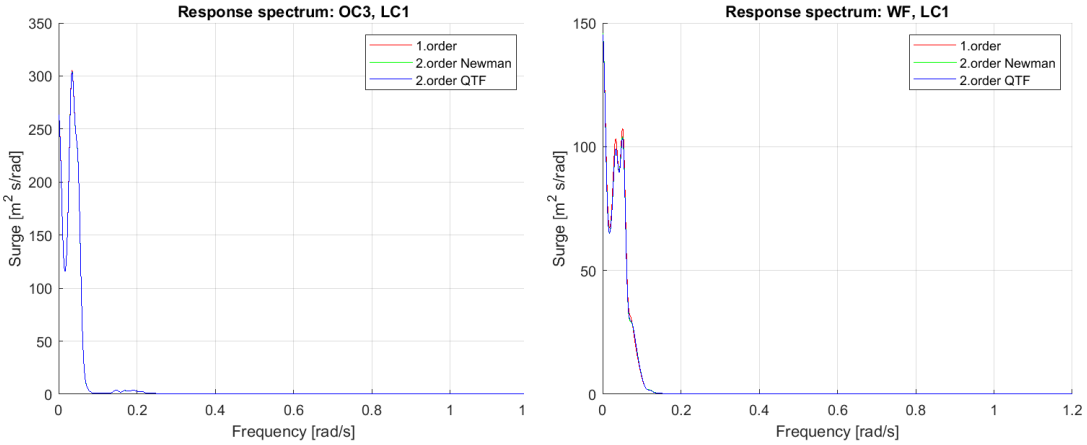

Figure C.2: Power spectral density of surge motion during LC1 for OC3-Hywind and WindFloat

C.2 Force Spectra Load Case 5

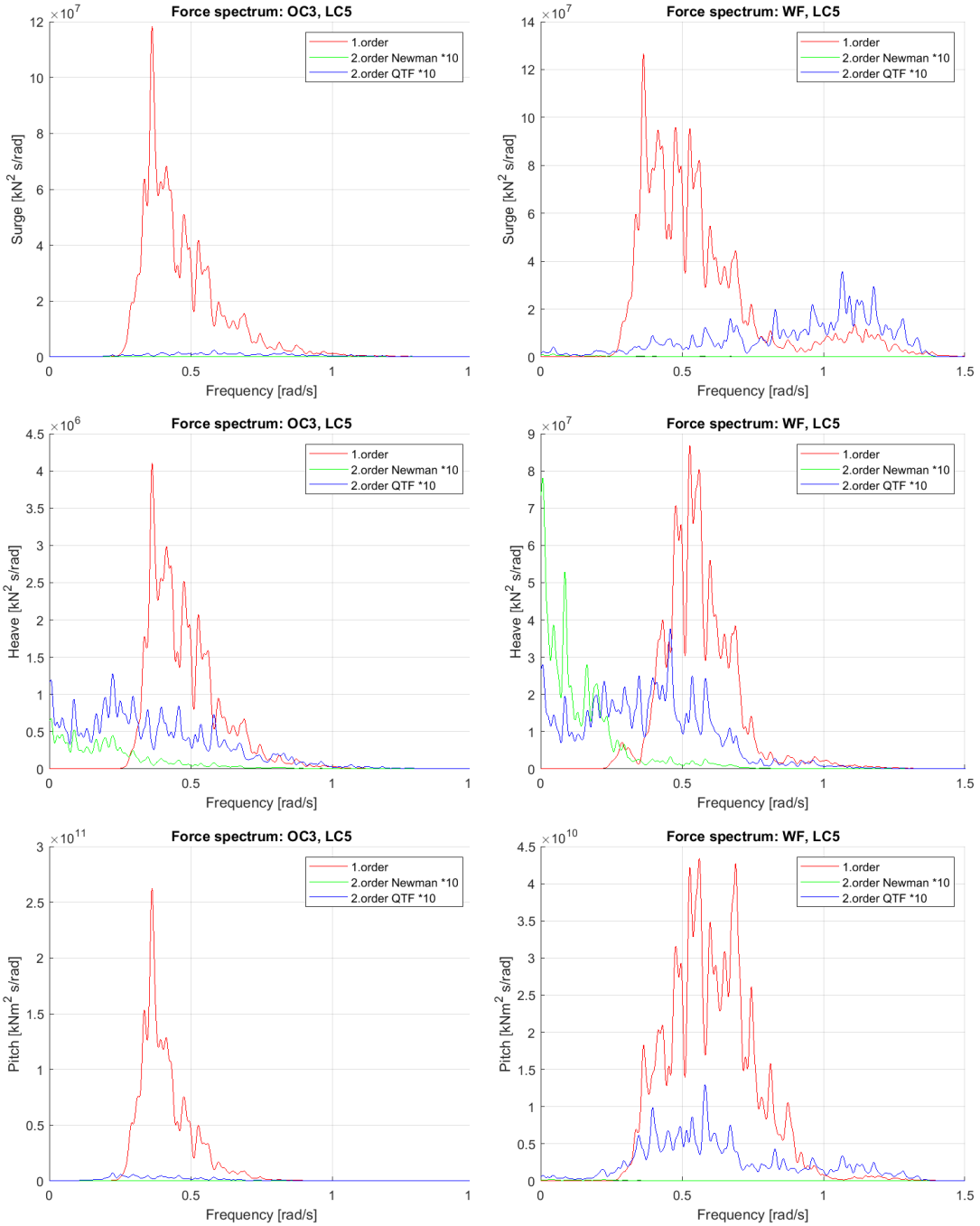

Figure C.3: Power spectral density of heave and pitch motion during LC1 for OC3-Hywind and WindFloat

Cecilie Vangdal

Hydrodynamic Study of Floating Wind Turbines in Extreme Conditions

NTNU
Norwegian University of
Science and Technology